Adsorption Performance of Activated Carbon in Heat Pump Systems: Insights for Sustainable Energy Applications

楊, 兆晟

Adsorption Performance of Activated Carbon in Heat Pump Systems: Insights for Sustainable Energy Applications

Dissertation

Zhaosheng Yang

Department of Energy and Environmental Engineering

Interdisciplinary Graduate School of Engineering Science

Kyushu University, Japan

February 2024

Adsorption Performance of Activated Carbon in Heat Pump Systems: Insights for Sustainable Energy Applications

A dissertation submitted in partial fulfilment of the requirements for the award of the degree of

Doctor of Philosophy

By

Zhaosheng Yang

Supervisor**: Professor Takahiko Miyazaki**

Co-supervisor: **Associate Professor Kyaw Thu**

Department of Energy and Environmental Engineering
Interdisciplinary Graduate School of Engineering Science
Kyushu University, Japan
February 2024

Acknowledgements

This research paper represents the culmination of my remarkable journey at Kyushu University in Japan, reflecting the collaborative efforts and unwavering support of several individuals who have significantly contributed to its realization.

Foremost, I extend my sincere appreciation to **Professor Takahiko Miyazaki**, and **Associate Professor Kyaw Thu** for their invaluable guidance and mentorship throughout the entirety of my research endeavor. Moreover, I express my sincere appreciation for their unwavering commitment to reviewing and providing feedback on my manuscript, despite their demanding academic commitments. Importantly, their understanding and patience during periods of underperformance and adversity have been paramount to my growth and development. Meanwhile, I would like to express my sincere appreciation to **Associate Professor Muhammad Sultan** for his crucial contributions to this study and his invaluable support throughout the acquisition and processing of experimental data. I also extend my gratitude to **Mr. Nobuo Takata** for his indispensable assistance during the experimental phase.

Furthermore, I would like to extend my gratitude to past and present laboratory colleagues and classmates. In particular, I would like to acknowledge the contributions of **Mr. Mojtaba Purjam, Dr. Sagar Saren, Mr. Seo Sang Won, Mr. Yang Cheng, Mr. Yu Hao,** and many other diligent and talented individuals. Their collaborative efforts and intellectual prowess have significantly enriched my research journey. I am deeply grateful for their companionship, assistance, and the lively atmosphere they fostered.

Moreover, I wish to express my sincerest appreciation to my family and friends

who have played an indispensable role in my academic pursuits. I would like to acknowledge my mother, **Mrs. Zhao Chunjuan,** as well as my father, **Mr. Yang Yong** my grandparents, uncles, and aunts. Their unwavering support and unwavering presence have been a constant source of inspiration and encouragement. Their selfless dedication, care, and enduring support without any expectation of reciprocity are deeply cherished.

Additionally, I would like to extend my thanks to the Japanese government, Kyushu University, and IGSES Interdisciplinary Graduate School of Engineering Science for their unwavering commitment to fostering a conducive learning environment and providing exceptional academic guidance. I am also deeply grateful for the financial assistance granted by the China Scholarship Council (CSC), which has played a crucial role in supporting my educational journey.

Table of Contents

Summary

With the gradual progression of countries worldwide towards carbon neutrality objectives and plans, refrigeration and air conditioning systems based on renewable energy sources or low-grade heat sources have gained substantial attention from both academia and industry. Due to their inherent advantages such as a broad range of heat source temperatures, utilization of environmentally friendly working fluids, corrosion resistance, system stability, and operational simplicity, adsorption systems have experienced significant research intensification on a global scale. These systems are increasingly being explored for diverse applications in sustainable energy utilization, encompassing areas such as gas storage, water desalination, thermal energy storage, and low-grade heat-driven heat pumps. Notably, adsorption heat pump (AHP) systems, which operate using industrial waste heat, geothermal energy, solar energy, and other low-temperature heat sources, offer a promising and prospective alternative solution to address the prevailing energy crisis and environmental concerns.

Among the various adsorbents investigated thus far, activated carbon (AC) has garnered attention as a potential adsorbent for adsorption heat pump applications. This can be attributed to its high surface area, extensive pore volume, and favorable adsorption properties exhibited towards diverse adsorbates. Hydrofluorocarbon (HFC) refrigerant, specifically difluoromethane (R32), possesses several advantageous features, including an appropriate boiling temperature, substantial latent heat of phase change, low global warming potential (GWP), zero ozone depletion potential (ODP), high energy efficiency, and cost-effectiveness. These characteristics render R32 an appealing choice for incorporation into air conditioning and heat pump systems,

making it an attractive alternative. As a chlorine-free substitute, R32 is regarded as an environmentally friendly option. The combined utilization of AC as an adsorbent and R32 as a refrigerant presents a promising avenue in the pursuit of sustainable and efficient adsorption heat pump systems.

This study entails a comprehensive analysis of the adsorption characteristics of the refrigerant R32 on activated carbon surfaces, along with an assessment of its feasibility and performance in a single-stage adsorption heat pump system. The research approach encompasses theoretical analysis, experimental investigations, thermodynamic analysis, and steady-state simulations. These methodologies collectively facilitate a thorough understanding of the adsorption properties exhibited by the AC-R32 working pair and elucidate its potential for application in heat pump systems driven by low-grade heat sources.

This study employs a thermal gravimetric approach to meticulously investigate the adsorption characteristics of the working pair across a broad temperature range, covering both subcritical and supercritical conditions. Special emphasis is placed on improving the accuracy of adsorption isotherm predictions and reducing fitting errors by proposing a novel adsorption potential model as an enhancement to the conventional Dubinin-Astakhov (D-A) models. The developed model is rigorously validated using experimental data from this study and previous research, thereby ensuring improved accuracy in predicting adsorption isotherms.

Theoretical analysis is undertaken to establish the fundamental principles and thermodynamic framework governing the adsorption process, including isosteric heat, specific heat capacity, enthalpy, and entropy. The thermodynamic adsorption interactions between the adsorbent and the adsorbate are thoroughly examined, further enhancing the understanding of the underlying mechanisms.

Furthermore, the adsorption kinetics of the refrigerant R32 on the surface of activated carbon were investigated. A comparative analysis is conducted among widely employed adsorption kinetics models, including the Linear Driving Force (LDF) model, Fickian Diffusion (FD) model, semi-infinite model and modified LDF models. The diffusion time constants pertinent to the MSC30-R32 working pair are calculated and compared with analogous working pairs involving MSC30 and various refrigerants. To enhance the accuracy and broaden the applicability of the Jribi-modified LDF models, a novel mass transfer coefficient model is proposed and experimentally validated. The obtained results are compared with those of other potential working pairs, laying the groundwork for optimizing the dynamic performance of adsorption heat pumps.

Steady-state simulations are conducted to further investigate the performance of adsorption heat pump systems utilizing the studied working pair. This involves the development of mathematical models to simulate system operation under different operating conditions and analyze energy efficiency and overall performance. The performance of the activated carbon-R32 working pair is compared with that of other commonly used adsorbent-refrigerant pairs. This comparative analysis aims to evaluate the advantages, limitations, and potential applications of the studied working pair in relation to alternative choices.

By combining experimental investigations with theoretical analysis, this study contributes to a comprehensive understanding of the adsorption behavior and thermodynamic properties of the working pair. These findings not only expand our understanding of adsorption phenomena but also substantially enhance the predictive capacity of computational models, thereby facilitating enhanced design and optimization of environmentally friendly adsorption technologies.

List of Figures

List of Tables

Chapter 1
Introduction

1.1 Background

The refrigeration and air conditioning systems account for 15% of the world's electricity consumption, and the majority of it is consumed by the vapor-compression based refrigeration systems [1, 2]. As nations around the world strive to achieve their goals for carbon neutrality, researchers are placing greater emphasis on exploring refrigeration and air conditioning systems that are powered by renewable energy or low-grade heat sources. The utilization of thermally powered adsorption heat pump systems has gained significant traction in recent years, as the urgency of mitigating the impacts of global warming and ozone depletion, coupled with the need for sustainable energy solutions, led to increased research and attention on this technology[3-6]. Adsorption heat pump has several advantages over the traditional compression-based system: (i) it is capable of utilizing low-temperature heat sources, thereby enabling the utilization of renewable energy sources or waste heat as a source of thermal energy [7-9]. (ii) it uses environmentally friendly refrigerants, such as water or ethanol, which do not contribute to ozone depletion or global warming [10-12]. (iii) no mechanical compressor is used, resulting in low power consumption and minimal production of noise and vibration [13, 14]. Overall, the use of adsorption heat pumps can lead to significant energy savings, environmental benefits, and cost savings for various

applications [15-19].

1.2 Adsorption Fundamentals

1.2.1 Adsorption Mechanisms

Adsorption is a fundamental phenomenon characterized by the accumulation of fluid clusters (adsorbate) on the surface and within the pores of a porous medium (adsorbent). It represents a molecular agglomeration process at the interface between two immiscible phases. Figure 1.1 illustrates a schematic diagram depicting the typical processes of adsorption and desorption. During adsorption process, the adsorbate molecules, driven by intermolecular non-equilibrium forces, become concentrated on the adsorbent solid surface, leading to a reduction in molecular freedom and the subsequent release of adsorption heat. Conversely, when the system temperature rises, the thermal motion of the adsorbed molecules intensifies. In cases where the adsorbent's attractive forces towards the adsorbate are insufficient to retain the adsorbed molecules, they disengage from the surface of the adsorbent and revert back to a gaseous or liquid state.

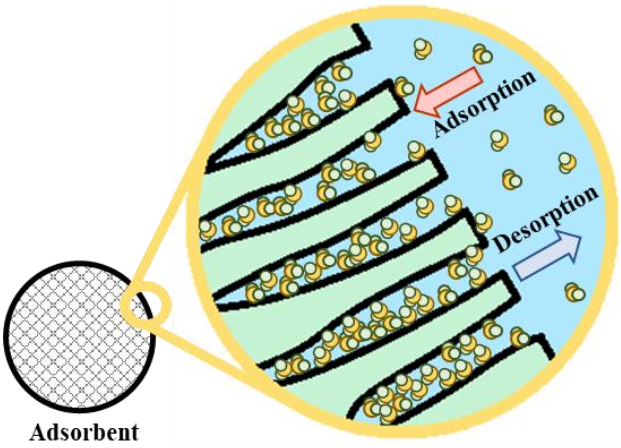

Figure 1.1 Typical adsorption process and desorption process in porous material

Adsorption is a phenomenon primarily governed by the intricate intermolecular interactions prevailing between the adsorbent and the adsorbate. These interactions primarily encompass molecular forces such as van der Waals forces, electrostatic interactions, and hydrogen bonding, exerting a pivotal influence on the adsorption process. Adsorption can be broadly categorized into two fundamental types: physical adsorption, commonly referred to as physisorption, and chemical adsorption, known as chemisorption. Physical adsorption relies on the prevailing van der Waals forces between molecules, and can give rise to the formation of multiple layers of adsorbate after the adsorption of a monolayer. The heat released accompanying physical adsorption is akin to that of condensation, signifying the condensation of adsorbate molecules onto the solid surface. Conversely, chemical adsorption is predominantly governed by the chemical reactivity between the adsorbate molecules and the surface of the adsorbent. This process involves intricate phenomena, including electron transfer, atomic rearrangement, and the formation and cleavage of chemical bonds. Notably, chemical adsorption often results in the formation of distinct chemical compounds at the adsorbent's surface, usually as a monolayer. The heat released associated with chemical adsorption corresponds to the enthalpy change of the relevant chemical reactions and surpasses that of physical adsorption. In Table 1.1, a comprehensive comparison of the two modes of adsorption is presented, highlighting their distinguishing characteristics and behaviors.

Physical adsorption is predominantly achieved through the utilization of various adsorbents, including activated carbon, carbon fibers, silica gel, zeolites, and metal-organic frameworks (MOFs). Conversely, chemical adsorption primarily relies on adsorbents such as metal halides, metal hydrides, and metal oxides[20]. While chemical adsorption exhibits significantly higher adsorption heat, it is limited to

specific operating conditions and selective interactions between particular working pairs. Moreover, chemical adsorption often demonstrates irreversibility, necessitating rigorous conditions and higher activation energy for desorption. Conversely, physical adsorption exhibits reversibility, allowing for easy desorption of the adsorbed molecules from the adsorbent surface. It demonstrates faster adsorption kinetics and offers greater controllability, enabling the manipulation of the adsorption-desorption process through temperature adjustments. Consequently, physical adsorption finds greater favor in numerous applications such as adsorption-based heat pumps, dehumidification systems, and carbon capture applications.

Table 1.1 Comparative analysis of physical adsorption and chemical adsorption

	Physical Adsorption	Chemical Adsorption
Adsorption Heat	21-63 kJ/mol, slightly larger than heat of condensation	42-125 kJ/mol, equivalent to heat of chemical reactions
Adsorption Force	van der Waals forces	unsaturated chemical bonds
Adsorption Rate	Fast	Slow
Reversibility	Reversible	difficult to desorb
Isotherm Characteristics	Uptake proportionally increases with pressure	Complex behavior
Isobar Characteristics	Adsorption uptake decreases with increasing temperature	Adsorption occurs at specific temperature ranges

1.2.2 Adsorption Equilibrium

When an adsorbent solid surface is exposed to a gas phase containing adsorbate

molecules, at the microscopic scale, the adsorbate molecules diffuse into the porous structure of the adsorbent. In the course of their thermal motion, some molecules collide with the adsorbent surface, experiencing both rebound and capture phenomena. The captured molecules adhere to the solid surface due to the attractive forces, such as van der Waals interactions. It is also worth noting that adsorbed molecules can be desorbed and reintroduced into the gas phase at the same time. Initially, during the early stages of adsorption process, the concentration of adsorbate molecules on the adsorbent surface is low, facilitating their capture and resulting in a rapid adsorption rate. However, as the number and layers of adsorbed molecules increase, the overall attractive forces exerted by the adsorbent on gas molecules diminish, leading to a gradual decrease in the adsorption rate and an increase in the desorption rate. Eventually, a dynamic equilibrium is attained, where the adsorption rate equals the desorption rate. This equilibrium state signifies that the quantity of adsorbate molecules adsorbed on the solid surface remains constant and is referred to as the equilibrium adsorption uptake or equilibrium capacity w ($kg \cdot kg^{-1}$)[21]. The equilibrium adsorption capacity w is primarily governed by the characteristics of the adsorbent-adsorbate system, along with the prevailing pressure p (kPa) and temperature T (K) conditions, which can be given by,

$$w = f(p, T, working\ pair) \tag{1.1}$$

The adsorption isotherm and isobar are the quantitative representation of the equilibrium state between the adsorbent and adsorbate, typically depicted graphically or mathematically. The adsorption isotherm describes the relationship between the amount of the adsorbate that is adsorbed onto the adsorbent surface and the pressure or concentration of that relationship in the surrounding environment at a constant

temperature [22]. An adsorption isobar, on the other hand, represents the relationship between the equilibrium adsorption uptake and the temperature at a constant pressure. The efficiency and effectiveness of adsorption heat pump system are strongly dependent on the properties of the adsorbent-adsorbate working pair, with particular emphasis on the adsorption isotherm. The adsorption isotherm plays a crucial role in understanding the adsorption phenomenon and characterizing the adsorbent's behavior. It reveals essential information regarding the adsorption capacity, surface properties, and affinity between the adsorbate and adsorbent. By analyzing the shape and features of the isotherm, valuable insights can be gained into the adsorption mechanism, pore structure, and surface chemistry of the adsorbent.

Extensive research has been conducted in the literatures on the physical adsorption behavior of different refrigerant-adsorbent pairs at temperatures below and above their critical points. Several of the studied working pair include: R134a + activated carbon (AC) pair [23, 24], R410A + ACs pair [25], CO_2 + ACs pair[26-28], CO_2 + zeolite pair[29], methanol + ACs pair[30, 31], ethanol + ACs pair[32, 33], water + MOFs pair[34-37], water + silica gels pair[38-40], ethanol + silica gels pair[41-43]. Various techniques have been established to evaluate the adsorption equilibrium, some of the most widely employed methods include: the magnetic suspension balance (MSB)[44-46], the constant volume variable pressure (CVVP) method[47-49], and the chromatographic method[50], etc. Hornbostel et al.[26] measured the adsorption equilibrium of various gases (CO_2, N_2, O_2, Ar, H_2O vapor, and impurities NO and SO_2) present in a flue gas stream on an advanced carbon adsorbent using a TGA unit. Saha et al.[24] studied the adsorption equilibrium data of R134a onto granular activated carbon and activated carbon fiber within adsorption temperatures range from 30 °C to 80 °C. And the experimental data were fitted to various popular isothermal models.

Srinivasan et al.[51] investigated the isothermal adsorption data of multiple gases on activated carbon and fitted to Dubinin-Astakhov (D-A) model, which considers the pseudo saturation pressure playing an important role in the supercritical gas adsorption. Saha et al.[22] conducted a comparative analysis of the isotherm data of CO_2 adsorption under supercritical conditions on two highly porous activated carbons. The authors utilized the empirical equation for the pseudo saturation pressure and fitted the experimental data. The resulting root-mean-square deviation (RMSD) ranged from 3.58 to 9.58.

1.2.3 Adsorption Thermodynamics

After gaining an understanding of the fundamental characteristics of the interaction between adsorbents and adsorbate species, as well as the equilibrium behavior of adsorption, thermodynamic parameters such as isosteric heat, specific heat capacity, enthalpy, and entropy serve a pivotal role in facilitating a rapid comprehension of the thermodynamic characteristics and spontaneity of adsorption phenomena. These parameters assume significant importance in the analysis, computation, and design of diverse applications reliant on adsorption processes. In the past, it was widely believed that adsorbed molecules on the solid surface of the adsorbent behaved as if they were in a liquid phase, and the released heat was approximated to be equivalent to the adsorbate's latent heat of condensation. The thermodynamic properties, including specific heat capacity, enthalpy and entropy, were also approximated using the values corresponding to a saturated liquid phase[52, 53]. However, as research has progressed, an increasing number of researchers have come to realize that although there is no explicit and precise phase boundary, the

thermodynamic phase of the adsorbed molecules can be distinguished[54]. This state is commonly referred to as the adsorbed phase. The thermodynamic properties of the adsorbed phase, including isosteric heat, specific heat capacity, entropy and enthalpy, are not only influenced by temperature and pressure but also exhibit variations with changes in the adsorption uptake[55-57].

During the adsorption process, the transition of adsorbate molecules from the gaseous phase to the adsorbed state leads to a decrease in their degrees of freedom and energy levels, resulting in the release of energy. The isosteric heat, defined as the ratio between the infinitesimal energy evolution and the infinitesimal mass change, plays a significant role in characterizing the thermodynamic features and spontaneity of adsorption phenomena[58]. Many researchers, employing both experimental and theoretical approaches, have revealed that the adsorption heat associated with physical adsorption is typically moderately higher, ranging between 30% and 100%, when compared to the corresponding condensation heat of the adsorbate. However, it is generally observed that the adsorption heat for physical adsorption remains lower than that observed for chemical adsorption[59]. It not only reflects the amount of energy released during the adsorption process, but also signifies the strength of the binding between the adsorbent and adsorbate molecules. Higher adsorption heat values indicate a greater amount of energy required to elevate the energy levels and degrees of freedom of the adsorbate molecules during the desorption process. [60]

Chua et al[56]. developed a comprehensive model to characterize the thermodynamic parameters of adsorbate-adsorbent pairs involving single-component systems. Their study focused on examining the behavior of specific heat capacities in different temperature and pressure conditions for several working pairs, such as silica gel-water, activated carbon-nitrogen, activated carbon- hydrogen systems.

Furthermore, Chakraborty et al[57, 61]. established a theoretical framework based on fundamental principles of classical thermodynamics. They employed this framework to derive insightful results and conducted an in-depth analysis of the adsorption heat and specific heat of two different working pairs: silica gel-water and activated carbon-methane. The developed models served as valuable tools for elucidating the thermodynamic characteristics associated with these adsorption systems. Azahar et al.[62] developed a thermodynamic model of the isosteric heat of adsorption to address the non-ideal behavior and the variation in the adsorbed phase density. The model was validated using experimental data and compared to existing models in the literature. The impact of each model on the heat pump systems' coefficient of performance (COP) was evaluated using six sets of adsorbent-adsorbate pairs.

1.2.4 Adsorption Kinetics

In adsorption systems, the efficacy requires not only high adsorption capacity but also rapid adsorption kinetics, which refers to the process of measuring the uptake of adsorbate over time at a constant pressure and temperature. The adsorption kinetics is crucial in determining the rate at which adsorbate molecules diffuse into the pores of the adsorbent material[63, 64]. Thus, understanding the adsorption kinetics is crucial for optimizing the design and operation of such systems to enhance their performance and efficiency and ultimately contribute towards sustainable development[65, 66]. An increase in adsorption kinetics can lead to a decrease in the system's cycle time, thus improving its cooling or heating capacity per unit time. The comprehension of kinetics models and parameters related to the adsorbent-refrigerant working pair is essential for designing an efficient adsorption heat pump system that can perform effectively

under diverse working conditions.

A significant amount of research has been carried out to explore the kinetics of different pairs of adsorbate and adsorbents[67-69], and numerous adsorption kinetic models have been formulated., including the Langmuir model[70], Linear driving force (LDF) model[71], Fickian diffusion (FD) model[72] and pseudo-first order reaction model[73]. Aristov et al.[65] conducted an experimental study on the adsorption kinetics of water onto silica gel, utilizing both the LDF and FD models in their investigation. The effect of different silica gel grain sizes on the adsorption kinetics were compared. Ghazy et al.[74] conducted a study to analyze the adsorption characteristics of AquaSorb 2000 activated carbon for HFC-404A in adsorption refrigeration systems at typical operating temperatures. The researchers employed both the LDF model and FD model to analyze the experimental results of the kinetics. The findings indicated that the pre-exponential coefficient was estimated to be 1.66×10^{-13} $m^2\cdot s^{-1}$, and the activation energy was calculated to be 18.8 $kJ\cdot kg^{-1}$. El-Sharkawy et al.[33] investigated the enhancement of ethanol adsorption performance by pretreating Maxsorb III with KOH-H_2 and H_2. The adsorption equilibrium and kinetics of the pretreated and untreated Maxsorb III were compared, and the data was fitted using the Dubinin–Radushkevich isotherm model and FD kinetics model. The results showed that the Maxsorb III treated with KOH-H_2 exhibited the highest diffusion time constant and activation energy, indicating an improved ethanol adsorption performance. However, the adsorption kinetics of the Maxsorb III treated with H_2 decreased compared to the untreated Maxsorb III.

The diffusive transport within porous media is a complex phenomenon that is influenced by various parameters, including the size and shape of the diffusing species, as well as the physicochemical characteristics of the porous adsorbent particles. To

enhance the precision of adsorption kinetic models in predicting the behavior of different working pairs at various adsorption stages, several researchers have dedicated significant efforts towards modifying the kinetic models. Sultan et al.[75] introduced a new fitting parameter to the LDF model, which resulted in increased degrees of freedom. As a consequence, the modified LDF model showed superior predictive capabilities in adsorption kinetics experiments when compared to commonly used models such as LFD, FD, and semi-infinite models. Jribi et al.[28] performed measurements of adsorption isotherms and kinetics of CO_2 on to MSC30 with gravimetric apparatus. They developed a novel model based on the linear driving force (LDF) model, which incorporated mass transfer coefficient to improve the model's predictive capabilities. The authors found that this modified LDF model outperformed the classic LDF model in terms of fitting the experimental data. Rupa et al.[76] introduced a new kinetics model for predicting adsorption dynamics in various adsorbate-adsorbent pairs. The model is validated using several adsorption pairs, showing accurate predictions during initial and saturated conditions. Adsorption processes often occur at various temperature and pressure ranges. Water and ethanol are typical adsorbates that operate at sub-atmospheric pressures while most refrigerants such as hydrocarbons and Hydrofluoroolefin at higher pressures. In some cases, the adsorption conditions are at supercritical states as in the adsorption of methane[44, 59] and propane[77]. Thus, one particular kinetics model cannot represent all types of adsorptions.

1.3 Adsorption Heat Pump System

The adsorption phenomena find extensive applications in various fields,

including heat pumps, thermal energy storage, dehumidification s, gas purification and separation, gas storage, catalysis and chemical reactions. Among these applications, adsorption heat pump systems utilize the heat released and adsorbed during the adsorption and desorption processes to achieve refrigeration or heating effects. A fundamental schematic diagram of an adsorption heat pump system is depicted in Figure 1.2, comprising (i) an adsorbent bed, which is filled with a solid adsorbent; (ii) an evaporator; (iii) a condenser; and (iv) an expansion valve. Figure 1.3 illustrates the Pressure-Temperature-Adsorption uptake (p-T-w) diagram of an adsorption heat pump cycle employing the activated carbon-R134a working pair at adsorption temperature of 30 ℃ and desorption temperature of 90 ℃.

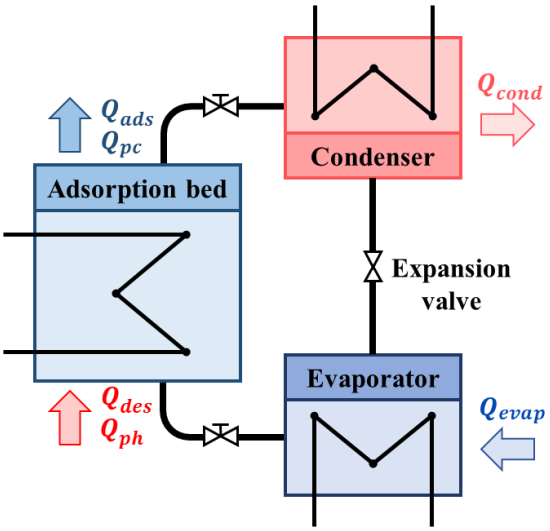

Figure 1.2 Schematic diagrams a basic single-bed adsorption heat pump cycle

In the adsorption heat pump cycle, the operational sequence involves several key steps. Initially, the adsorbent bed is pre-cooled to reduce its temperature and pressure. Subsequently, the connection between the adsorbent bed and the evaporator allows the refrigerant working fluid to undergo evaporation within the evaporator. During this phase, the refrigerant absorbs heat from the chilled water Q_{evap}. The resulting

evaporated refrigerant gas proceeds to enter the adsorbent bed, where it undergoes adsorption by the adsorbent material present within the bed. This adsorption process liberates adsorption heat known as Q_{ads} Following the adsorption stage, the adsorbent bed undergoes preheating to elevate its temperature. The heated adsorbent bed is then connected to the condenser. The necessary heat Q_{ph} and Q_{des} for desorption are introduced into the adsorbent bed, promoting the detachment of adsorbed refrigerant molecules. These desorbed molecules subsequently enter the condenser, where they undergo condensation and release the corresponding condensation heat Q_{cond} into the cooling water. Hence, in the context of the refrigeration cycle, the coefficient of performance (COP) of the adsorption heat pump can be expressed succinctly as follows:

$$COP_{cooling} = \frac{Q_{evap}}{Q_{ph}+Q_{des}} \tag{1.2}$$

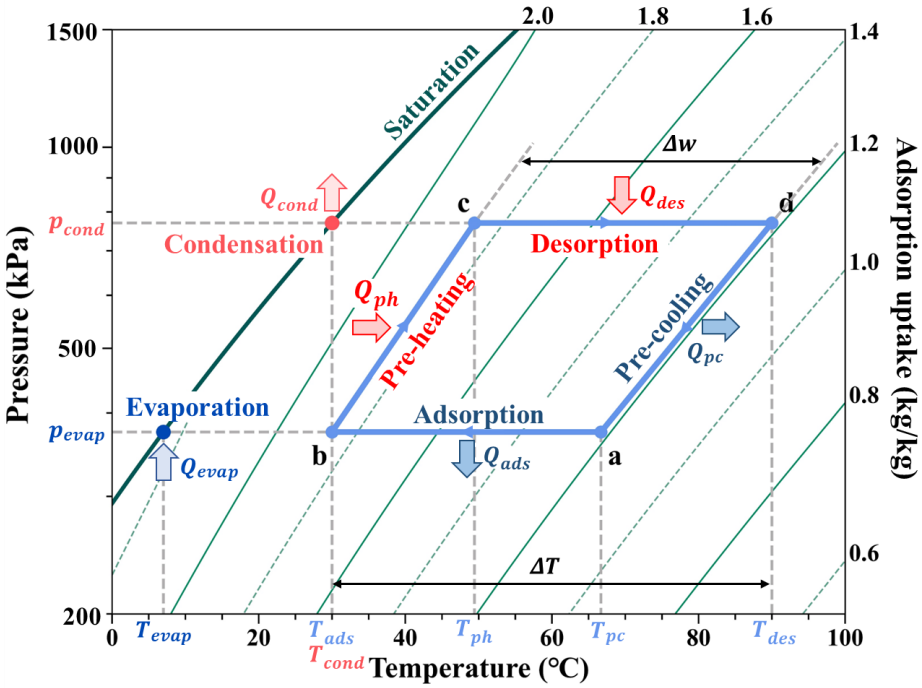

Figure 1.3 Thermodynamic cycle of a basic adsorption heat pump with MSC30-R134a at adsorption temperature of 30 ℃ and desorption temperature of 90 ℃.

For a more comprehensive description of the adsorption heat pump cycle, please refer to Section 5.2. Adsorption heat pump systems offer several advantages that make them attractive for cooling or heating applications. Firstly, they can utilize a wide range of low-grade heat sources, such as solar energy, geothermal energy, industrial waste heat, and biomass. This versatility expands the potential application scenarios for adsorption heat pumps. Secondly, these systems do not require moving components like compressors, resulting in significantly lower electric power consumption, reduced noise, and minimal vibration. This feature contributes to their energy efficiency and operational reliability. Thirdly, adsorption heat pumps can employ environmentally friendly refrigerant working pairs, mitigating concerns about environmental impact, corrosion, and toxicity. This aspect aligns with sustainability goals and reduces greenhouse gas emissions. Meanwhile, the operational principles and structural simplicity of adsorption heat pump systems make them relatively easy to control and maintain[14]. These advantages position them as potential alternatives to traditional vapor compression heat pumps and absorption heat pump systems. As a result, there has been a growing interest among researchers in exploring and investigating the capabilities of adsorption heat pump systems[78, 79].

However, it is important to acknowledge the limitations of adsorption heat pump systems. One significant drawback is their lower operating efficiency compared to traditional vapor compression heat pump systems. The coefficient of performance (COP) values for adsorption heat pumps typically ranges from 0.1 to 0.8 in refrigeration conditions. This implies that a considerable amount of energy input is required to achieve the desired heating and cooling effects. Another limitation is the need for multiple adsorbent beds to ensure continuous operation, resulting in larger system volume and mass. This restricts the practical implementation of adsorption heat

pumps in space-constrained environments. To further advance the utilization of adsorption heat pump systems, ongoing research is focused on enhancing their energy efficiency, optimizing operating conditions, and developing advanced materials with improved adsorption characteristics. Overcoming these limitations will contribute to their wider adoption and integration into various heating and cooling applications[80-83].

Singh et al.[84] conducted a series of experiments to investigate the adsorption isotherms of three different commercially available activated carbons with respect to CO_2 as adsorbate. They extensively analyzed the thermodynamic characteristics of the identified AC-CO_2 working pairs in order to understand their performance in adsorption refrigeration systems. The researchers compared the performance of these systems using the three pairs and determined the minimum operating temperature required. The results showed that the highest values achieved for the specific cooling effect (SCE) and the COP were 25.87 $kJ \cdot kg^{-1}$ and 0.09, respectively. Pinheiro et al.[85] developed a Computational Fluid Dynamics (CFD) solver in OpenFOAM for simulating adsorption heat pump heating cycles using the metal-organic framework (MOF) CPO-27(Ni) as the adsorbent and water as the adsorbate. The researchers employed an innovative approach by applying the adsorbent coating on a copper foam metal surface to enhance heat and mass transfer. Their simulation results indicated that the COP ranged from 1.16 to 1.39, while the specific heating power (SHP) varied between 1.9 and 5.1 $kW \cdot kg^{-1}$. Furthermore, Myat et al.[9] conducted experimental investigations on a waste heat driven adsorption refrigeration system utilizing zeolite-water working pair. They examined the influence of cycle time, heat source temperature, and heat recovery time on the system's performance. The experiments demonstrated that the system achieved a minimum driving temperature of 55°C, and

the optimal COP of approximately 0.48 was obtained when the heat source temperature reached 65℃. These findings contribute to the understanding and development of efficient adsorption-based heat pump systems of cooling and heating applications.

1.4 Objectives and Scope

The primary objectives of this research are to assess the viability and performance of a single-stage adsorption heat pump system employing activated carbon (Type MSC30) and difluoromethane (R32) refrigerant as the working pair. The investigation aims to comprehensively analyze the adsorption characteristics of this working pair and explore its potential application in heat pump systems driven by low-grade heat sources. The research adopts a multidisciplinary approach, incorporating theoretical analysis, experimental testing, thermodynamic analysis, and steady-state simulations, to gain a comprehensive understanding of the system's behavior. To achieve these research objectives, the scope of this work primarily encompasses the following aspects:

1. To comprehensively analyze the adsorption capacity and equilibrium characteristics of refrigerant R32 on activated carbon under subcritical and supercritical conditions, experimental testing is conducted using the thermal gravimetric approach across a wide temperature range.
2. To provide a new correlation of adsorption potential model, aiming to improve the accuracy of predicting adsorption isotherms and thermodynamic properties. To validate the effectiveness of the model, experimental data obtained in this research and data from previous studies will be utilized, a

comprehensive comparison will be conducted between the model predictions and the experimetal data.

3. To get a deeper understanding of the thermodynamic aspects of adsorption processes of the target adsorbent and adsorbate. The aim is to establish a theoretical analysis that elucidates the fundamental principles and thermodynamic framework governing the adsorption process. This involves the investigation of adsorption equilibrium and the development of models for thermodynamic parameters such as isosteric heat, specific heat capacity, enthalpy, and entropy. These endeavors contribute to a deeper understanding of the thermodynamic aspects of adsorption processes.
4. To examine the adsorption kinetics characteristics of R32 refrigerant on activated carbon surfaces. Various adsorption kinetics models will be compared, and a modifed adsorption kinetics model will be proposed and validated. Furthermore, a comparative analysis will be conducted to compare the adsorption kinetics of the investigated working pair with other potential working pairs, thereby establishing a basis for optimizing the dynamic performance of adsorption heat pumps.
5. To further investigate the performance of adsorption heat pump systems employing the studied working pair through steady-state simulations. This research endeavor involves the development and utilization of mathematical models to accurately simulate the system's behavior under various operating conditions, enabling an in-depth analysis of its energy efficiency and overall performance metrics. A comparative assessment will be conducted, juxtaposing the performance of the activated carbon-R32 working pair with that of other widely used adsorbent-refrigerant combinations. This

comparative analysis aims to critically evaluate the strengths, limitations, and potential applications of the investigated working pair relative to alternative options.

1.5 Thesis Outline

This thesis endeavor encompasses a comprehensive exploration of six distinct chapters that elucidate the experimental and simulation work in the realm of equilibrium analysis, thermodynamics analysis, kinetics analysis, and heat pump systems utilizing activated carbon-R32 as the adsorbent-adsorbate working pair. The orderly arrangement of these chapters within this scholarly thesis is as follows:

Chapter 1: Introduction

Chapter 2: Adsorption Equilibrium of R32 Vapor on Activated Carbon

Chapter 3: Adsorption Thermodynamics of Activated Carbon-R32 Systems

Chapter 4: Adsorption Kinetics of Activated Carbon-R32 Systems

Chapter 5: Steady-State Cycle Analysis for Adsorption Cooling Application

Chapter 6: Conclusions

A summary of the key contents of each chapter is provided below:

Chapter 1 provides a comprehensive macroscopic introduction and literature review on the adsorbent-adsorbate working pairs materials and their applications in the field of adsorption-based heat pump systems. This chapter elucidates the fundamental principles governing the adsorption process for such systems and establishes the theoretical framework underlying their operation. It also critically

examines the existing literatures and prior investigations, assesses the current state of knowledge, and identifies gaps in research. Furthermore, the chapter offers a comprehensive exposition of the research background, rationale, significance, and specific objectives, thereby laying a solid groundwork for the subsequent chapters.

Chapter 2 is dedicated to a comprehensive analysis of adsorption equilibrium and the validation of a thermodynamic model for adsorbate-adsorbent working pairs under supercritical conditions. The investigation begins by conducting experiments using a magnetic suspension adsorption measurement apparatusto assess the adsorption characteristics of refrigerant R32 on activated carbon MSC30. The experimental campaign encompasses a wide range of adsorption temperatures (25°C to 150°C) and pressures up to 3000 kPa, covering both subcritical and supercritical operating conditions. Subsequently, a novel thermodynamic model is introduced to describe the adsorption potential at temperatures above the critical point. The proposed model is validated using the experimental data obtained in this study, as well as data from relevant literature sources. Furthermore, a comparative analysis is conducted to compare the performance of the new model with conventional pseudo-saturation pressure models and Tóth adsorption isotherm models.

Chapter 3 delves into a thorough discussion on the thermodynamic analysis associated with the adsorption process. A comprehensive theoretical framework is presented and derived, encompassing crucial parameters such as the isosteric heat, specific heat capacity, entropy, and enthalpy of R32 vapor adsorbed on MSC30. Building upon the previously introduced adsorption potential model, two distinct adsorption heat models are derived, considering the volumetric correction of the adsorbed phase in one model and neglecting it in the other. Rigorous comparisons and validations against data from diverse working pairs and classical models are conducted.

Furthermore, utilizing experimental data, this chapter calculates and analyzes the specific heat capacity, entropy, and enthalpy of the adsorbate phase within the MSC30-R32 working pair, over a temperature range spanning 0 to 160 ℃. The chapter evaluates the influential factors of temperature, pressure, and adsorption uptake on the thermophysical properties of the working pair and conducts a comparative analysis with other relevant working pairs, thereby enhancing our understanding of the adsorption phenomena under investigation.

Chapter 4 provides a comprehensive investigation into the adsorption kinetics of R32 on the MSC30 adsorbent under subcritical and supercritical conditions. The chapter encompasses both experimental and theoretical analyses, aiming to elucidate the underlying mechanisms and optimize the adsorption process. A comparative analysis is conducted among widely employed adsorption kinetics models, including the Linear Driving Force (LDF) model, Fickian Diffusion (FD) model, and semi-infinite model. The diffusion time constants pertinent to the MSC30-R32 working pair are precisely calculated and compared with analogous working pairs involving MSC30 and various refrigerants. To enhance accuracy and broaden the applicability of the Jribi-modified LDF models, a novel mass transfer coefficient model is proposed. This model integrates empirical parameters into the Jribi-modified LDF model to refine its predictive capabilities. The efficacy of the proposed model is rigorously assessed through regression analysis of transient adsorption-desorption data. Furthermore, the reliability and effectiveness of the model are corroborated via extensive validation using adsorbate-adsorbent pairs across different temperature ranges. The insights derived from this chapter contribute to advancing the understanding of adsorption kinetics and facilitate the design and optimization of adsorption processes for various applications.

Chapter 5 presents a comprehensive analysis of the thermodynamic performance of an equilibrium adsorption cooling cycle using the MSC30-R32 working pair. This analysis is based on the prior chapters' findings, including the derived adsorption isotherm models, adsorption heat, and specific heat capacity of the adsorbate-adsorbent system. The chapter focuses on investigating the thermal dynamics of a low-temperature-driven adsorption refrigeration system and examines the influence of various operational parameters, such as adsorption temperature, evaporation temperature, desorption temperature, and mass ratio, on key performance indicators like specific cooling energy (SCE) and coefficient of performance (COP). Moreover, a comparative analysis is conducted to assess the working conditions and performance characteristics of adsorption heat pump systems utilizing commonly used adsorbent-refrigerant pairs, namely MSC30-CO2 and MSC30-R245fa. The insights provided in this chapter contribute to a deeper understanding of adsorption refrigeration cycles and aid in the selection and optimization of adsorbent-refrigerant pairs for enhanced efficiency and sustainable cooling applications.

Chapter 6, the final chapter, presents a comprehensive synthesis of the research findings obtained from both experimental investigations and simulation work. It encapsulates the primary conclusions derived from these endeavors and elucidates their potential implications in the field of adsorption heat pumps. Furthermore, this chapter delves into the identification of prospective avenues for future research, outlining promising directions that hold potential for further exploration and improvement in this domain.

1.6 Nomenclature

COP	Coefficient of performance (-)
p	Pressure (kPa)
Q	Thermal energy (kJ)
SCE	Specific cooling energy ($kJ \cdot kg^{-1}$)
SHP	Specific heating power ($kW \cdot kg^{-1}$)
T	Temperature (K)
w	Equilibrium uptake in mass ratio ($kg \cdot kg^{-1}$)
Subscript	
ads	Adsorption
cond	Condenser
des	Desorption
evap	Evaporator
pc	Pre-cooling
ph	Pre-heating

1.7 References

[1] P. Goyal, P. Baredar, A. Mittal, A.R. Siddiqui. Adsorption refrigeration technology - An overview of theory and its solar energy applications, J. *Renewable & Sustainable Energy Reviews*. 53(2016) 1389-1410, doi: 10.1016/j.rser.2015.09.027.

[2] B. Choudhury, P.K. Chatterjee, J.P. Sarkar. Review paper on solar-powered air-conditioning through adsorption route, J. *Renewable & Sustainable Energy Reviews*. 14(2010) 2189-2195, doi: 10.1016/j.rser.2010.03.025.

[3] R.P. Sah, B. Choudhury, R.K. Das, A. Sur. An overview of modelling techniques employed for performance simulation of low grade heat operated adsorption cooling systems, J. *Renewable & Sustainable Energy Reviews*. 74(2017) 364-376, doi: 10.1016/j.rser.2017.02.062.

[4] Y. Fan, L. Luo, B. Souyri. Review of solar sorption refrigeration technologies:

Development and applications, J. *Renewable & Sustainable Energy Reviews*. 11(2007) 1758-1775, doi: 10.1016/j.rser.2006.01.007.

[5] L.W. Wang, R.Z. Wang, R.G. Oliveira. A review on adsorption working pairs for refrigeration, J. *Renewable & Sustainable Energy Reviews*. 13(2009) 518-534, doi: 10.1016/j.rser.2007.12.002.

[6] P.R. Chauhan, S.C. Kaushik, S.K. Tyagi. A review on thermal performance enhancement of green cooling system using different adsorbent/refrigerant pairs, J. *Energy Conversion and Management-X*. 14(2022), doi: ARTN 100225 10.1016/j.ecmx.2022.100225.

[7] R.Z. Wang, R.G. Oliveira. Adsorption refrigeration - An efficient way to make good use of waste heat and solar energy, J. *Progress in Energy and Combustion Science*. 32(2006) 424-458, doi: 10.1016/j.pecs.2006.01.002.

[8] K. Thu, A. Chakraborty, B.B. Saha, K.C. Ng. Thermo-physical properties of silica gel for adsorption desalination cycle, J. *Applied Thermal Engineering*. 50(2013) 1596-1602, doi: 10.1016/j.applthermaleng.2011.09.038.

[9] A. Myat, N.K. Choon, K. Thu, Y.D. Kim. Experimental investigation on the optimal performance of Zeolite-water adsorption chiller, J. *Applied Energy*. 102(2013) 582-590, doi: 10.1016/j.apenergy.2012.08.005.

[10] A. Chakraborty, K.C. Leong, K. Thu, B.B. Saha, K.C. Ng. Theoretical insight of adsorption cooling, J. *Applied Physics Letters*. 98(2011), doi: Artn 221910 10.1063/1.3592260.

[11] I.I. El-Sharkawy, K. Uddin, T. Miyazaki, B. Baran Saha, S. Koyama, H.-S. Kil, S.-H. Yoon, J. Miyawaki. Adsorption of ethanol onto phenol resin based adsorbents for developing next generation cooling systems, J. *International Journal of Heat and Mass Transfer*. 81(2015) 171-178, doi: 10.1016/j.ijheatmasstransfer.2014.10.012.

[12] Z. Liu, J. Xu, M. Xu, C. Huang, R. Wang, T. Li, X. Huai. Ultralow-temperature-driven water-based sorption refrigeration enabled by low-cost zeolite-like porous aluminophosphate, J. *Nat Commun*. 13(2022) 193, doi: 10.1038/s41467-021-27883-4.

[13] J. Xu, Q.W. Pan, W. Zhang, Z.L. Liu, R.Z. Wang, T.S. Ge. Design and

experimental study on a hybrid adsorption refrigeration system using desiccant coated heat exchangers for efficient energy utilization, J. *Renewable & Sustainable Energy Reviews*. 169(2022), doi: ARTN 112890 10.1016/j.rser.2022.112890.

[14] H. Demir, M. Mobedi, S. Ulku. A review on adsorption heat pump: Problems and solutions, J. *Renewable & Sustainable Energy Reviews*. 12(2008) 2381-2403, doi: 10.1016/j.rser.2007.06.005.

[15] N.C. Srivastava, I.W. Eames. A review of adsorbents and adsorbates in solid-vapour adsorption heat pump systems, J. *Applied Thermal Engineering*. 18(1998) 707-714, doi: Doi 10.1016/S1359-4311(97)00106-3.

[16] M.F. de Lange, K.J. Verouden, T.J. Vlugt, J. Gascon, F. Kapteijn. Adsorption-Driven Heat Pumps: The Potential of Metal-Organic Frameworks, J. *Chem Rev*. 115(2015) 12205-12250, doi: 10.1021/acs.chemrev.5b00059.

[17] G.G. Ilis, H. Demir. Influence of bed thickness and particle size on performance of microwave regenerated adsorption heat pump, J. *International Journal of Heat and Mass Transfer*. 123(2018) 16-24, doi: 10.1016/j.ijheatmasstransfer.2018.02.063.

[18] G.G. Ilis, H. Demir, B.B. Saha. Innovative approach in adsorption chiller: Combination of condenser-adsorber for improving performance, J. *Applied Thermal Engineering*. 192(2021), doi: ARTN 116958 10.1016/j.applthermaleng.2021.116958.

[19] Q.W. Pan, J. Xu, R.Z. Wang, T.S. Ge. A new operation strategy based on unequal ad-/desorption time for a two-bed adsorption refrigeration system, J. *Energy*. 259(2022), doi: ARTN 124977 10.1016/j.energy.2022.124977.

[20] L. Jiang, A.P. Roskilly. Thermal conductivity, permeability and reaction characteristic enhancement of ammonia solid sorbents: A review, J. *International Journal of Heat and Mass Transfer*. 130(2019) 1206-1225, doi: 10.1016/j.ijheatmasstransfer.2018.11.029.

[21] D.D. Do. Adsorption Analysis: Equilibria and Kinetics, 1998.

[22] B.B. Saha, S. Jribi, S. Koyama, I.I. E-Sharkawy. Carbon Dioxide Adsorption Isotherms on Activated Carbons, J. *Journal of Chemical and Engineering Data*.

56(2011) 1974-1981, doi: 10.1021/je100973t.

[23] K. Habib, B.B. Saha, K.A. Rahman, A. Chakraborty, S. Koyama, K.C. Ng. Experimental study on adsorption kinetics of activated carbon/R134a and activated carbon/R507A pairs, J. *International Journal of Refrigeration-Revue Internationale Du Froid*. 33(2010) 706-713, doi: 10.1016/j.ijrefrig.2010.01.006.

[24] B.B. Saha, I.I. El-Sharkawy, R. Thorpe, R.E. Critoph. Accurate adsorption isotherms of R134a onto activated carbons for cooling and freezing applications, J. *International Journal of Refrigeration-Revue Internationale Du Froid*. 35(2012) 499-505, doi: 10.1016/j.ijrefrig.2011.05.002.

[25] A.A. Askalany, B.B. Saha, I.M. Ismail. Adsorption isotherms and kinetics of HFC410A onto activated carbons, J. *Applied Thermal Engineering*. 72(2014) 237-243, doi: 10.1016/j.applthermaleng.2014.04.075.

[26] M.D. Hornbostel, J. Bao, G. Krishnan, A. Nagar, I. Jayaweera, T. Kobayashi, A. Sanjurjo, J. Sweeney, D. Carruthers, M.A. Petruska, L. Dubois. Characteristics of an advanced carbon sorbent for CO2 capture, J. *Carbon*. 56(2013) 77-85, doi: 10.1016/j.carbon.2012.12.082.

[27] A. Pal, I.I. EI-Sharkawy, B.B. Saha, S. Jribi, T. Miyazaki, S. Koyama. Experimental investigation of CO2 adsorption onto a carbon based consolidated composite adsorbent for adsorption cooling application, J. *Applied Thermal Engineering*. 109(2016) 304-311, doi: 10.1016/j.applthermaleng.2016.08.031.

[28] S. Jribi, T. Miyazaki, B.B. Saha, A. Pal, M.M. Younes, S. Koyama, A. Maalej. Equilibrium and kinetics of CO2 adsorption onto activated carbon, J. *International Journal of Heat and Mass Transfer*. 108(2017) 1941-1946, doi: 10.1016/j.ijheatmasstransfer.2016.12.114.

[29] B.K. Sward, M.D. LeVan. Examination of the performance of a compression-driven adsorption cooling cycle, J. *Applied Thermal Engineering*. 19(1999) 1-20, doi: Doi 10.1016/S1359-4311(98)00013-1.

[30] K. Thu, Y.D. Kim, A. Bin Ismil, B.B. Saha, K.C. Ng. Adsorption characteristics of methane on Maxsorb III by gravimetric method, J. *Applied Thermal Engineering*. 72(2014) 200-205, doi: 10.1016/j.applthermaleng.2014.04.076.

[31] I.I. El-Sharkawy, M. Hassan, B.B. Saha, S. Koyama, M.M. Nasr. Study on

adsorption of methanol onto carbon based adsorbents, J. *International Journal of Refrigeration-Revue Internationale Du Froid*. 32(2009) 1579-1586, doi: 10.1016/j.ijrefrig.2009.06.011.

[32] K. Uddin, I.I. El-Sharkawy, T. Miyazaki, B.B. Saha, S. Koyama, H.S. Kil, J. Miyawaki, S.H. Yoon. Adsorption characteristics of ethanol onto functional activated carbons with controlled oxygen content, J. *Applied Thermal Engineering*. 72(2014) 211-218, doi: 10.1016/j.applthermaleng.2014.03.062.

[33] I.I. El-Sharkawy, K. Uddin, T. Miyazaki, B.B. Saha, S. Koyama, J. Miyawaki, S.H. Yoon. Adsorption of ethanol onto parent and surface treated activated carbon powders, J. *International Journal of Heat and Mass Transfer*. 73(2014) 445-455, doi: 10.1016/j.ijheatmasstransfer.2014.02.046.

[34] B.B. Saha, I.I. El-Sharkawy, T. Miyazaki, S. Koyama, S.K. Henninger, A. Herbst, C. Janiak. Ethanol adsorption onto metal organic framework: Theory and experiments, J. *Energy*. 79(2015) 363-370, doi: 10.1016/j.energy.2014.11.022.

[35] Z. Chen, Z. Shao, Y. Tang, F. Deng, S. Du, R. Wang. Study of the Scale-Up Effect on the Water Sorption Performance of MOF Materials, J. *ACS Materials Au*. 3(2022) 43-54, doi: 10.1021/acsmaterialsau.2c00052.

[36] T.Y. Yang, L.R. Ge, T.S. Ge, G.W. Zhan, R.Z. Wang. Binder-Free Growth of Aluminum-Based Metal-Organic Frameworks on Aluminum Substrate for Enhanced Water Adsorption Capacity, J. *Advanced Functional Materials*. 32(2022), doi: ARTN 2105267 10.1002/adfm.202105267.

[37] L.R. Ge, T.S. Ge, R.Z. Wang. Facile synthesis of Al-based MOF and its applications in desiccant coated heat exchangers, J. *Renewable & Sustainable Energy Reviews*. 157(2022), doi: ARTN 112015 10.1016/j.rser.2021.112015.

[38] S. Mitra, P. Kumar, K. Srinivasan, P. Dutta. Performance evaluation of a two-stage silica gel plus water adsorption based cooling-cum-desalination system, J. *International Journal of Refrigeration-Revue Internationale Du Froid*. 58(2015) 186-198, doi: 10.1016/j.ijrefrig.2015.06.018.

[39] K.C. Ng, H.T. Chua, C.Y. Chung, C.H. Loke, T. Kashiwagi, A. Akisawa, B.B. Saha. Experimental investigation of the silica gel-water adsorption isotherm characteristics, J. *Applied Thermal Engineering*. 21(2001) 1631-1642, doi: Doi 10.1016/S1359-4311(01)00039-4.

[40] Q. Pan, L. Liu, B. Wang, J. Xu, T. Ge. Design and experimental study on a small-scale silica gel/water adsorption chiller with heat and mass recovery scheme for solar energy use, J. *Solar Energy*. 252(2023) 91-100, doi: 10.1016/j.solener.2023.01.052.

[41] R. Habash, G.G. Ilis, H. Demir, H.F. Oztop. Analysis of low-grade heat driven ethanol-silica gel adsorption chiller, J. *Thermal Science and Engineering Progress*. 26(2021), doi: ARTN 101125 10.1016/j.tsep.2021.101125.

[42] A. Rezk, G.G. Ilis, H. Demir. Experimental study on silica gel/ethanol adsorption characteristics for low-grade thermal driven adsorption refrigeration systems, J. *Thermal Science and Engineering Progress*. 34(2022), doi: ARTN 101429 10.1016/j.tsep.2022.101429.

[43] A. Rezk, A.G. Olabi, A.H. Alami, A. Radwan, H. Demir, S.M.A. Rahman, S.K. Shah, M.A. Abdelkareem. Experimental Study on Utilizing Silica Gel with Ethanol and Water for Adsorption Heat Storage, J. *Energies*. 16(2022), doi: 10.3390/en16010444.

[44] S. Himeno, T. Komatsu, S. Fujita. High-pressure adsorption equilibria of methane and carbon dioxide on several activated carbons, J. *Journal of Chemical and Engineering Data*. 50(2005) 369-376, doi: 10.1021/je049786x.

[45] M. Sultan, T. Miyazaki, B.B. Saha, S. Koyama, H.S. Kil, K. Nakabayashi, J. Miyawaki, S.H. Yoon. Adsorption of Difluoromethane (HFC-32) onto phenol resin based adsorbent: Theory and experiments, J. *International Journal of Heat and Mass Transfer*. 127(2018) 348-356, doi: 10.1016/j.ijheatmasstransfer.2018.07.097.

[46] B. Berdenova, A. Pal, M. Muttakin, S. Mitra, K. Thu, B.B. Saha, A. Kaltayev. A comprehensive study to evaluate absolute uptake of carbon dioxide adsorption onto composite adsorbent, J. *International Journal of Refrigeration-Revue Internationale Du Froid*. 100(2019) 131-140, doi: 10.1016/j.ijrefrig.2019.01.014.

[47] S. Seo, H. Kawakami, F. Miksik, N. Takata, K. Thu, T. Miyazaki. Thermodynamic analysis and impact of thermal masses on adsorption cycles using MaxsorbIII/R245fa and SAC-2/R245fa pairs, J. *International Journal of Refrigeration*. 123(2021) 52-62, doi: 10.1016/j.ijrefrig.2020.12.005.

[48] W.S. Loh, K.A. Rahman, A. Chakraborty, B.B. Saha, Y.S. Choo, B.C. Khoo, K.C.

Ng. Improved Isotherm Data for Adsorption of Methane on Activated Carbons, J. *Journal of Chemical and Engineering Data*. 55(2010) 2840-2847, doi: 10.1021/je901011c.

[49] A.A. Askalany, B.B. Saha, K. Uddin, T. Miyzaki, S. Koyama, K. Srinivasan, I.M. Ismail. Adsorption Isotherms and Heat of Adsorption of Difluoromethane on Activated Carbons, J. *Journal of Chemical and Engineering Data*. 58(2013) 2828-2834, doi: 10.1021/je4005678.

[50] Z.Y. Gu, C.X. Yang, N. Chang, X.P. Yan. Metal-organic frameworks for analytical chemistry: from sample collection to chromatographic separation, J. *Acc Chem Res*. 45(2012) 734-745, doi: 10.1021/ar2002599.

[51] K. Srinivasan, B.B. Saha, K.C. Ng, P. Dutta, M. Prasad. A method for the calculation of the adsorbed phase volume and pseudo-saturation pressure from adsorption isotherm data on activated carbon, J. *Phys Chem Chem Phys*. 13(2011) 12559-12570, doi: 10.1039/c1cp20383e.

[52] S.M. Sami, C. Tribes. An improved model for predicting the dynamic behaviour of adsorption systems, J. *Applied Thermal Engineering*. 16(1996) 149-161, doi: 10.1016/1359-4311(95)00054-h.

[53] H.T. Chua, K.C. Ng, A. Malek, T. Kashiwagi, A. Akisawa, B.B. Saha. Modeling the performance of two-bed, sillica gel-water adsorption chillers, J. *International Journal of Refrigeration*. 22(1999) 194-204, doi: 10.1016/s0140-7007(98)00063-2.

[54] D.P. Foster, E. Orlandini, M.C. Tesi. Surface critical exponents for models of polymer collapse and adsorption: the universality of the Theta and Theta ' points, J. *Journal of Physics A: Mathematical and General*. 25(1992) L1211-L1217, doi: 10.1088/0305-4470/25/21/002.

[55] D.D. Do, H.D. Do. Adsorption of supercritical fluids in non-porous and porous carbons: analysis of adsorbed phase volume and density, J. *Carbon*. 41(2003) 1777-1791, doi: 10.1016/s0008-6223(03)00152-0.

[56] H.T. Chua, K.C. Ng, N. Chakraborty, N.M. Oo. Thermodynamic property fields of an adsorbate-adsorbent system, J. *Langmuir*. 19(2003) 2254-2259, doi: 10.1021/la0267140.

[57] A. Chakraborty, B.B. Saha, K.C. Ng, S. Koyama, K. Srinivasan. Theoretical Insight of Physical Adsorption for a Single-Component Adsorbent plus Adsorbate System: I. Thermodynamic Property Surfaces, J. *Langmuir*. 25(2009) 2204-2211, doi: 10.1021/la803289p.

[58] A.B. ISMAIL. Experimental and Theoretical Studies on Adsorption Chillers Driven by Waste Heat and Propane, National University of Singapore, 2013.

[59] K.A. RAHMAN. Experimental and Theoretical Studies on Adsorbed Natural Gas Storage System Using Activated Carbons, National University of Singapore, 2011.

[60] M. Sultan, T. Miyazaki, S. Koyama, Z.M. Khan. Performance evaluation of hydrophilic organic polymer sorbents for desiccant air-conditioning applications, J. *Adsorption Science & Technology*. 36(2017) 311-326, doi: 10.1177/0263617417692338.

[61] A. Chakraborty, K.C. Ng, B.B. Saha, El-Sharkawy, II. THEORETICAL INSIGHT OF PHYSICAL ADSORPTION FOR A SINGLE COMPONENT ADSORBENT-ADSORBATE SYSTEM, 2010.

[62] F.H.M. Azahar, S. Mitra, A. Yabushita, A. Harata, B.B. Saha, K. Thu. Improved model for the isosteric heat of adsorption and impacts on the performance of heat pump cycles, J. *Applied Thermal Engineering*. 143(2018) 688-700, doi: 10.1016/j.applthermaleng.2018.07.131.

[63] G.L. An, L.W. Wang, J. Gao, R.Z. Wang. A review on the solid sorption mechanism and kinetic models of metal halide-ammonia working pairs, J. *Renewable & Sustainable Energy Reviews*. 91(2018) 783-792, doi: 10.1016/j.rser.2018.04.032.

[64] J.P. Simonin. On the comparison of pseudo-first order and pseudo-second order rate laws in the modeling of adsorption kinetics, J. *Chemical Engineering Journal*. 300(2016) 254-263, doi: 10.1016/j.cej.2016.04.079.

[65] Y.I. Aristov, M.M. Tokarev, A. Freni, I.S. Glaznev, G. Restuccia. Kinetics of water adsorption on silica Fuji Davison RD, J. *Microporous and Mesoporous Materials*. 96(2006) 65-71, doi: 10.1016/j.micromeso.2006.06.008.

[66] W. Dang, J.C. Zhang, H.K. Nie, F.Q. Wang, X. Tang, N. Wu, Q. Chen, X.L. Wei,

R.J. Wang. Isotherms, thermodynamics and kinetics of methane-shale adsorption pair under supercritical condition: Implications for understanding the nature of shale gas adsorption process, J. *Chemical Engineering Journal*. 383(2020), doi: ARTN 123191 10.1016/j.cej.2019.123191.

[67] H.W.B. Teo, A. Chakraborty, Y. Kitagawa, S. Kayal. Experimental study of isotherms and kinetics for adsorption of water on Aluminium Fumarate, J. *International Journal of Heat and Mass Transfer*. 114(2017) 621-627, doi: 10.1016/j.ijheatmasstransfer.2017.06.086.

[68] P. Ammendola, F. Raganati, R. Chirone, F. Miccio. Fixed bed adsorption as affected by thermodynamics and kinetics: Yellow tuff for CO2 capture, J. *Powder Technology*. 373(2020) 446-458, doi: 10.1016/j.powtec.2020.06.075.

[69] A.A. Askalany, K. Uddin, B.B. Saha, M. Sultan, G. Santori. Water desalination by silica supported ionic liquid: Adsorption kinetics and system modeling, J. *Energy*. 239(2022), doi: 10.1016/j.energy.2021.122069.

[70] I. Langmuir. The Adsorption of Gases on Plane Surfaces of Glass, Mica and Platinum, J. *Journal of the American Chemical Society*. 40(2002) 1361-1403, doi: 10.1021/ja02242a004.

[71] E. Glueckauf. Theory of chromatography. Part 10.—Formulæ for diffusion into spheres and their application to chromatography, J. *Trans Faraday Soc*. 51(1955) 1540-1551, doi: 10.1039/tf9555101540.

[72] S.K. Bhatia, M.R. Bonilla, D. Nicholson. Molecular transport in nanopores: a theoretical perspective, J. *Phys Chem Chem Phys*. 13(2011) 15350-15383, doi: 10.1039/c1cp21166h.

[73] J.L. Latham, A.E. Burgess. Elementary Reaction Kinetics, 1918.

[74] M. Ghazy, A.A. Askalany, K. Harby, M.S. Ahmed. Adsorption isotherms and kinetics of HFC-404A onto bituminous based granular activated carbon for storage and cooling applications, J. *Applied Thermal Engineering*. 105(2016) 639-645, doi: 10.1016/j.applthermaleng.2016.03.057.

[75] M. Sultan, I.I. El-Sharkawy, T. Miyazaki, B.B. Saha, S. Koyama, T. Maruyama, S. Maeda, T. Nakamura. Water vapor sorption kinetics of polymer based sorbents: Theory and experiments, J. *Applied Thermal Engineering*. 106(2016) 192-202,

doi: 10.1016/j.applthermaleng.2016.05.192.

[76] M.J. Rupa, A. Pal, S. Mitra, B.B. Saha. Time adapted linear driving force model for gas adsorption onto solids, J. *Chemical Engineering Journal*. 420(2021), doi: ARTN 129785 10.1016/j.cej.2021.129785.

[77] N. Tzabar, H.J.M. ter Brake. Adsorption isotherms and Sips models of nitrogen, methane, ethane, and propane on commercial activated carbons and polyvinylidene chloride, J. *Adsorption-Journal of the International Adsorption Society*. 22(2016) 901-914, doi: 10.1007/s10450-016-9794-9.

[78] J.M. Pinheiro, S. Salústio, J. Rocha, A.A. Valente, C.M. Silva. Adsorption heat pumps for heating applications, J. *Renewable and Sustainable Energy Reviews*. 119(2020), doi: 10.1016/j.rser.2019.109528.

[79] N. Riaz, M. Sultan, S. Noor, U. Sajjad, M. Farooq, M.U. Khan, S. Hanif, F. Riaz. Recent developments in adsorption heat pumps for heating applications, J. *Advances in Mechanical Engineering*. 14(2022), doi: Artn 16878132221089444 10.1177/16878132221089444.

[80] L.F. Cabeza, A. Sole, C. Barreneche. Review on sorption materials and technologies for heat pumps and thermal energy storage, J. *Renewable Energy*. 110(2017) 3-39, doi: 10.1016/j.renene.2016.09.059.

[81] Z.Y. Yang, M. Qu, K.R. Gluesenkamp. Ammonia-based chemisorption heat pumps for cold-climate heating applications: A comprehensive review, J. *Applied Thermal Engineering*. 179(2020), doi: ARTN 115674 10.1016/j.applthermaleng.2020.115674.

[82] J.H. Ahn, J.S. Lee, C. Baek, Y. Kim. Performance improvement of a dehumidifying heat pump using an additional waste heat source in electric vehicles with low occupancy, J. *Energy*. 115(2016) 67-75, doi: 10.1016/j.energy.2016.08.104.

[83] J.M.S. Dias, V.A.F. Costa. Adsorption heat pumps for heating applications: A review of current state, literature gaps and development challenges, J. *Renewable and Sustainable Energy Reviews*. 98(2018) 317-327, doi: 10.1016/j.rser.2018.09.026.

[84] V.K. Singh, E.A. Kumar. Experimental investigation and thermodynamic analysis

of CO 2 adsorption on activated carbons for cooling system, J. *Journal of CO2 Utilization*. 17(2017) 290-304, doi: 10.1016/j.jcou.2016.12.004.

[85] J.M. Pinheiro, S. Salustio, V. Geraldes, A.A. Valente, C.M. Silva. Copper foam coated with CPO-27(Ni) metal-organic framework for adsorption heat pump: Simulation study using OpenFOAM, J. *Applied Thermal Engineering*. 178(2020), doi: ARTN 115498 10.1016/j.applthermaleng.2020.115498.

Chapter 2
Adsorption Equilibrium of R32 Vapor on Activated Carbon

2.1 Introduction

As an important tool for studying adsorption phenomena, adsorption isotherms provide a quantitative description of the relationship between the amount of adsorbate on the adsorbent surface and the equilibrium concentration of the adsorbate in the bulk phase. Adsorption isotherms play a crucial role in designing and optimizing various adsorption working pairs and systems. Isotherm models can be used to analyze the adsorption mechanism, estimate the maximum adsorption capacity, and predict the behavior of the adsorbent under different temperature and pressure conditions. By fitting experimental data with various isotherm models, researchers can determine the most suitable model for a particular adsorbent-adsorbate pair and obtain parameters that are essential for subsequent thermodynamic and kinetic analyses. Therefore, understanding adsorption isotherms is always the first step in studying adsorption working pairs and their applications in various technological fields.

In this chapter, an automated and controlled magnetic suspension adsorption measurement unit (MSB-VG-10M) was utilized to investigate the adsorption characteristics of the environmentally friendly refrigerant R32 on MSC 30. Experiments have been conducted within a range of adsorption temperatures from

25 °C to 150 °C and pressure up to 3000 kPa. Moreover, a new thermodynamic model for the adsorption potential at a temperature above the critical point is proposed and validated using experimental data and compared to the conventional pseudo saturation pressure model and Tóth adsorption isotherms model.

2.2 Materials

2.2.1 Adsorbent Materials

The present study uses MSC 30 as the adsorbent material. MSC 30 is a carbon-based adsorbent material commonly utilized in various industrial applications, such as adsorption chillers, and heat pumps. It is known for its high surface area-to-volume ratio, high porosity, and thermal stability. These properties endow MSC 30 with exceptional adsorption and desorption capabilities, particularly for refrigerant molecules, making it a popular choice as the adsorbent material in adsorption systems. The thermophysical properties of the MSC 30 have been investigated by Thu et al.[1] as presented in Table 2.1. In this work, samples of MSC 30 were supplied by Kansai Coke Chemical Co., Ltd., Japan. Before conducting the experiments, the samples were subjected to a pre-treatment process of heating in an oven at 130°C for approximately 4 hours to remove any moisture present and to ensure the accuracy of mass measurements.

Table 2.1 Porosity and elemental composition of MSC 30

MSC 30	Properties	Values
Porosity	Total surface area ($m^2 \cdot g^{-1}$)	3045
	Average pore width (nm)	1.11
	Pore volume (cm3·g-1)	1.7
Elemental composition	Carbon (wt.%)	95.13
	Hydrogen (wt.%)	0.14
	Nitrogen (wt.%)	0.25
	Oxygen (wt.%)	4.35
	Ash (wt.%)	0.13

2.2.2 Adsorbate Materials

The hydrofluorocarbon (HFC) refrigerant difluoromethane (R32) is selected in this study as the adsorbate. The thermophysical properties of R32 are summarized in Table 2.2. Its boiling temperature at a pressure of one atmosphere is -51.65°C, and its critical point is 78.11 °C and 5782 kPa. The refrigerant R32 is a refrigerant with several advantages over other commonly used refrigerants, including a low global warming potential (GWP), high energy efficiency, cost-effective and a good safety profile. These properties make it an attractive option for use in air conditioning and heat pump systems. As a chlorine-free alternative, it is considered to be an environmentally friendly option. Samples of R32, with a stated purity of 99.5%, were procured from Daikin, Ltd., Japan.

Table 2.2 Properties of commonly used refrigerants

Properties	R32	R134a	R245fa
Chemical Formula	CH_2F_2	$C_2H_2F_4$	$C_3H_3F_5$
Flammability	Low	Low	Low
Toxicity	No	Low	Low
Ozone depletion potential	0	0	0
Global warming potential	675	1300	858
Critical temperature (°C)	78.11	101.06	153.86
Critical pressure (kPa)	5782	4059	3651
Triple temperature (°C)	-136.81	-103.30	-102.1
Triple pressure (kPa)	0.048	0.390	0.014
Specific volume at Triple point ($m3 \cdot kg^{-1}$)	0.00070	0.00063	0.00061
Boiling Temperature (°C)	-51.65	-26.30	15.05
Specific volume at boiling point ($m^3 \cdot kg^{-1}$)	0.00082	0.00073	0.00073
Van der Waals volume ($cm^3 \cdot mol^{-1}$)	0.00121	0.00094	0.00091
Molar mass ($g \cdot mol^{-1}$)	52.02	102.03	134.05

2.3 Experimental Section

2.3.1 Apparatus and Procedure

In this study, the adsorption uptake of R32 onto the surface of MSC30 is quantified using a magnetic suspension adsorption measurement apparatus (MSB-VG-10M, MicrotracBEL Corp). This approach allows for real-time monitoring of the adsorption process under controlled conditions, providing a comprehensive

understanding of the adsorption properties of the system. It is important to underscore that the original experimental data presented herein predominantly derive from the research endeavors of Associate Professor Muhammad Sultan during his tenure within our laboratory.

The magnetic levitation balance system utilizes a non-contact method to weigh the sample, eliminating direct contact between the measuring unit and the balance. This approach ensures that the balance is not affected by the measurement environment, resulting in more accurate measurements. Additionally, this method enables measurements to be taken at high temperatures and pressures, making it a suitable technique for the quantification of adsorption properties in this research.

The schematic diagram of the experimental setup is shown in Figure 2.1. The main components of the apparatus include magnetic levitation balance, thermostatic circulating oil bath that controls adsorption and evaporation temperature, air thermostatic bath to avoid condensation through connecting tubes, and ultrahigh vacuum system i.e., diaphragm, rotary and turbomolecular vacuum pump. The pressure sensor had a maximum measurement capacity of 10 MPa and was able to measure pressure with precision and accuracy of ±0.002% and ±0.05% of the full-scale range, respectively. The measurement apparatus allows for a maximum sample weight of 15 g with a resolution of 10 mg for recording the adsorbed or desorbed mass, and a repeatability of weight measurement of ±30 milligrams with a relative error of ±0.002%. During the weighing process, the adsorbent sample is immersed in the bulk gas and experiences an upward force due to buoyancy. As the mass of the sample being tested is quite small, the effect of buoyancy on the weight measurement cannot be ignored. To account for this, the measurement system takes buoyancy correction into account during the measurement. To avoid condensation inside the connecting tube,

an air bath was used to maintain the piping temperature at 20 °C above the saturation temperature of the refrigerant.

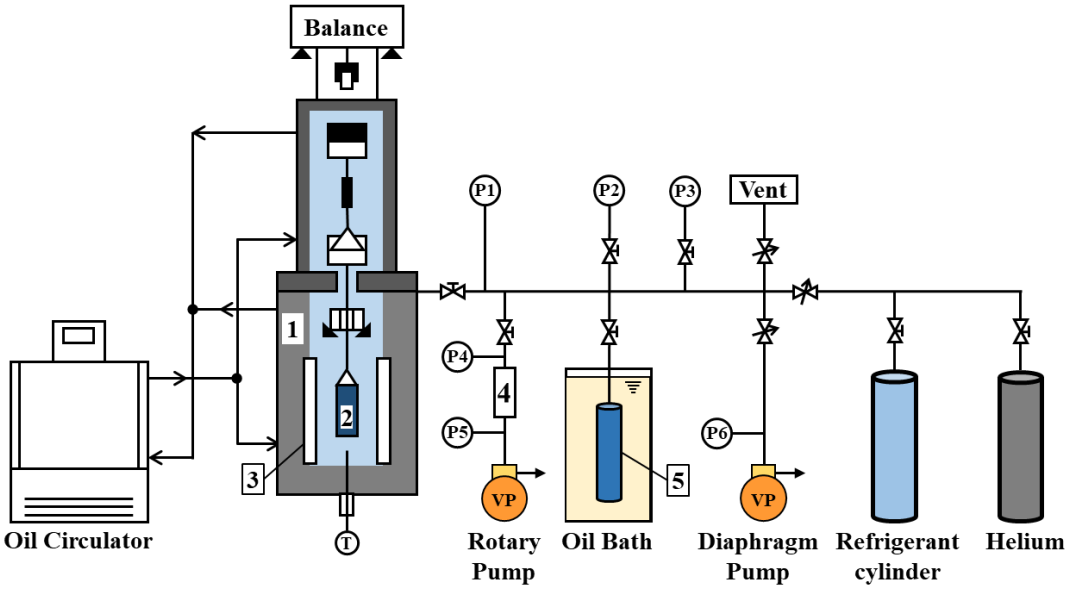

1. Circulation oil jacket, 2. Sample cell, 3. Sheathed heater,

4. Terbo-molecular pump, 5. Refrigerant charging cell

Figure 2.1 Schematic diagram of the experimental set up

The experiment was conducted within adsorption temperature at 25 °C, 30 °C, 50 °C, 70 °C, 90 °C, 110 °C, 130 °C, 150 °C and pressures up to 3000 kPa. Key points of the experimental procedure for each isotherm measurement can be explained as follows:

(i) For each adsorption isotherm measurement, the adsorbent sample is placed into the sample cell and heated at 130 °C for 4 hours under a vacuum condition of about 3×10^{-4} Pa to remove any adsorbed gas inside the sample.

(ii) The dried adsorbent sample is cooled to the set temperature and kept at that temperature throughout the adsorption process.

(iii) The valve connecting the refrigerant charging cell and the sample cell is then

opened, allowing the sorbent to begin adsorbing the refrigerant vapor. The adsorption uptake is continuously monitored utilizing the MSB until a state of equilibrium is attained.

(iv) The valve between the refrigerant charge cell and sample cell is then closed, and the refrigerant charge cell is heated in preparation for the next relative pressure step.

(v) Repeat steps 3,4 until the desired pressure is achieved.

2.4 Theoretical Models

2.4.1 Absolute Adsorption Uptake Estimation

Figure 2.2 presents a schematic diagram depicting the adsorbate concentration on the surface of the adsorbent as a function of the distance from the adsorbent surface at the microscopic level[2]. Depending on the distance from the adsorbent surface, it can be divided into three distinct regions: (i) the interior region of the adsorbent solid, (ii) the region within the adsorption layer, and (iii) the gaseous region. In region (i), volume-based adsorption concentration of the adsorbate $c(x)$ is zero. The $c(x)$ value exhibits a progressively decrease with increasing distance x from the adsorbent surface[3]. At a distance x equal to the thickness of the adsorbed layer x_{layer}, the final concentration $c(x)$ reaches the same level as that of the ambient gas concentration c_{gas}. It is worth noting that the c_{gas}, which approximately follows the ideal gas law, depends only on the temperature and pressure conditions. On the other hand, the concentration of the adsorbed molecules within the adsorbed layer is not only influenced by temperature and pressure but also by the van der Waals forces between

the adsorbate and adsorbent surface as well as the adsorption loading.

Under constant temperature and pressure conditions, the adsorption concentration is a function of the distance from the adsorbent surface. The number of adsorbed adsorbate molecules below the adsorption layer can be expressed as:

$$n_{abs} = S \int_0^{x_{layer}} c(x)\ dx \tag{2.1}$$

Here, S is the interfacial area (m^2), n_{abs} is the absolute molar uptake ($mol \cdot g^{-1}$)

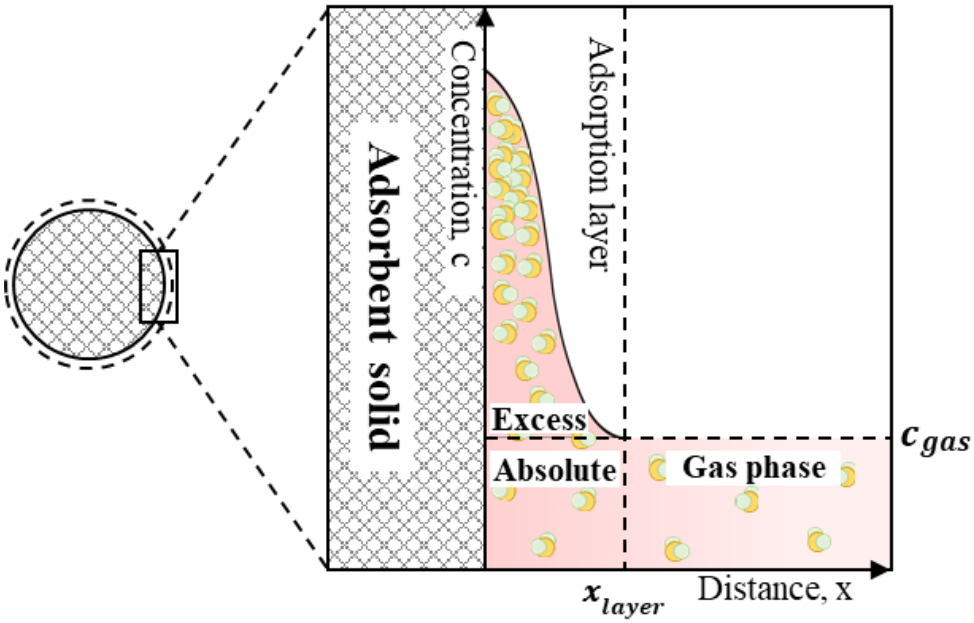

Figure 2.2 Schematic illustration of adsorption process

In gravimetric measurement apparatus, the sample is weighed while immersed in an adsorbate gas environment and is subject to a buoyancy force that is equal in magnitude to the mass of the displaced gas volume corresponding to the sample and adsorbed adsorbate. Correction for this buoyancy is often necessary. The adsorption uptake data obtained from the magnetic suspension adsorption measurement unit

represents the excess adsorption uptake, which is the result after accounting for buoyancy correction. The excess uptake only accounts for the fraction of the adsorbed molecules that exceed the ambient concentration, while neglecting a portion of the gas molecules present in the region below the adsorption layer, which can be evaluated as:

$$n_{exc} = S \int_0^{x_{layer}} c(x) - c_{gas}\, dx \tag{2.2}$$

While buoyancy correction is utilized to negate the influence of buoyancy on experimental results, it also leads to the introduction of new measurement uncertainties[4]. For this reason, it is essential to perform a correction for the absolute adsorption uptake, which can be derived from the excess adsorption values using the following methods.

The method I assumes that the specific volume of gas in the adsorbed state is equal to the specific pore volume of the adsorbent [5, 6]. The concentration of the ignored adsorbed phase is equal to the concentration of the gas phase in the environment. Therefore, the absolute adsorption amount is obtained by adding the product of the porosity of the adsorbent and the gas phase density of the adsorbate to the excess adsorption amount.

$$w_{abs}^{I} = w_{exc} + \rho_{ref} \cdot v_{pore} \tag{2.3}$$

Here, ρ_{ref} is the density of the refrigerant gas, v_{pore} denotes the specific pore volume of the adsorbent.

Method I is based on a very straightforward assumption and its calculation is very simple, therefore it has been applied by many researchers[7, 8]. However, it assumes that the pore volume of the adsorbent is used to replace the specific volume of the adsorbed phase gas molecules, this means that the entire internal volume of the porous

material's pores is assumed to be located below the adsorption layer, which can result in an overestimation of the absolute adsorption amount.

Method II assumes that the adsorbed phase gas volume can be neglected but requires a linear correction to be made to the excess adsorption amount. In method II[9], the excess uptake data are transformed twice to achieve a linear representation, and data points that do not satisfy the constraint were eliminated during the transformations. A plot of $ln[ln\, n_{exc}]$ as a function of $1/\ln p$, based on the experimental data, is thus constructed, as illustrated in Figure 2.3. To avoid evaluating logarithms of negative numbers n_{exc} is enlarged tenfold[10]. The values of intercept $\delta(T)$ and slope $\varphi(T)$ derived from this linear plot can be utilized to calculate the absolute adsorption. Obtained values of δ and φ are listed in Table 2.3.

$$\ln[\ln n_{exc}] = \delta(T) + \frac{\varphi(T)}{\ln p} \tag{2.4}$$

$$n_{abs} = exp\left[exp\left(\delta(T) + \frac{\varphi(T)}{ln\, p}\right)\right] \tag{2.5}$$

$$w_{abs}^{II} = \frac{n_{abs}}{mm_{ref}} \tag{2.6}$$

Table 2.3 Values of δ and φ at different temperatures

Temperature (°C)	25	30	50	70	90	110	130	150
δ	2.37	2.39	2.46	2.58	2.70	2.82	2.97	3.20
φ	-4.48	-4.81	-5.75	-7.03	-8.31	-9.67	-11.26	-13.41

As the above-mentioned 2 methods for determining absolute adsorption uptake represent two extremes, Berdenova et al.[4] suggested the Method III, which utilized

the mean value of Methods I and II to calculate the absolute adsorption amount, given as,

$$w_{abs,ave} = \frac{w_{abs}^{I} + w_{abs}^{II}}{2} \tag{2.7}$$

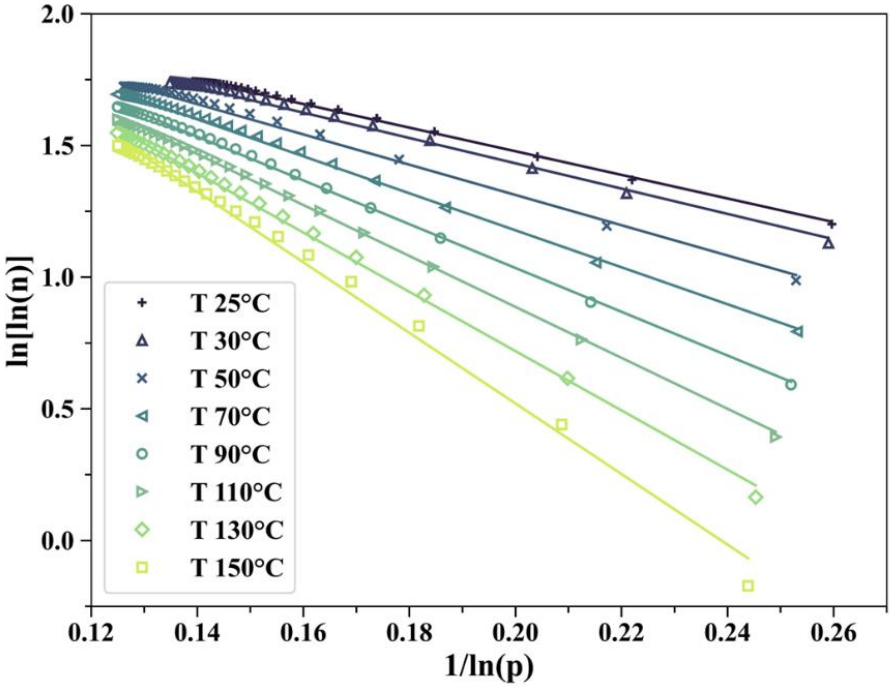

Figure 2.3 Linear plot of the excess adsorption

2.4.2 Adsorption Isotherms Models

2.4.2.1 Dubinin-Astakov (D-A) model

The Dubinin-Astakov (D-A) model is one of the most widely used Type I adsorption equilibrium models and is frequently deployed in studies of refrigerant vapor adsorption on microporous activated carbon. The D-A model is based on the theory of micropore volume filling, which assumes that the adsorption volume is related to the pore volume of the adsorbent[11]. In this model, surface heterogeneity

is considered, and it is applicable to high-pressure adsorption equilibrium[12]. The corresponding equation is:

$$\theta = \frac{w}{w_0} = \exp\left[-\left(\frac{A}{E}\right)^n\right] \tag{2.8}$$

Here, θ is the surface coverage ranging from zero to one, w is the equilibrium uptake in the mass ratio ($kg \cdot kg^{-1}$). The mass-based maximum adsorption uptake w_0 ($kg \cdot kg^{-1}$), the characteristic energy of adsorption E ($J \cdot mol^{-1}$), and the heterogeneity factor n are the three essential parameters of the D-A model. They are evaluated using adsorption isotherms data by using the best fit for non-linear regression analysis.

It is of significance to highlight that the D-A model has been derived from the Dubinin–Radushkevich (D-R) model, encompassing considerations pertaining to the non-uniformity of the adsorbent surface. When the heterogeneity factor n within the D-A model assumes a value of 2, the model seamlessly reverts to the foundational D-R model, as delineated in the subsequent equation:

$$\theta = \frac{w}{w_0} = \exp\left[-\left(\frac{A}{E}\right)^2\right] \tag{2.9}$$

In the D-A model, A is the adsorption potential ($J \cdot mol^{-1}$)

$$A = RT \cdot \ln\left(\frac{p_{sat}}{p}\right) \tag{2.10}$$

Here, R is the molar gas constant ($8.314\ J \cdot mol^{-1} \cdot K^{-1}$), T is the temperature (K), p and p_{sat} stand for the equilibrium and saturation pressure of adsorbate at the adsorption temperature respectively (kPa). The adsorption potential is an important factor in determining the thermodynamic properties of gas adsorption, particularly under supercritical conditions.

The adsorbed phase has often been assumed to be equivalent to the liquid phase

for a long time, with the same physical parameters[13]. Considering the compressibility of the liquid phase, the difference between adsorbed phase and the liquid phase cannot be ignored, especially working under high pressure[14], so the adsorbed phase volume correction has been frequently used in recent years to fit the adsorption isotherm data more accurately. The D-A isotherm model with volume correction is expressed as,

$$w = \frac{c_0}{v_{aded}} exp\left[-\left(\frac{A}{E}\right)^n\right] \tag{2.11}$$

Where c_0 is the volume-based maximum uptake ($cm^3 \cdot g^{-1}$), v_{aded} is the specific volume of the adsorbed phase, which is given by,

$$v_{aded}(T) = \begin{cases} v_{boil} \exp[\alpha(T - T_{boil})], & p_{trip} < p_{amb} \\ v_{trip} \exp[\alpha(T - T_{trip})], & p_{trip} \geq p_{amb} \end{cases} \tag{2.12}$$

Here, v_{boil} and v_{trip} are the specific volume at the boiling point and triple point, ($m^3 \cdot kg^{-1}$) respectively. α is the thermal expansion coefficient of the adsorbed phase, which is given by the Nikolayev and Dubinin model[15].

$$\alpha = \begin{cases} \frac{\ln\left(\frac{b_w}{v_{boil}}\right)}{T_{trip} - T_{boil}}, & p_{trip} < p_{amb} \\ \frac{\ln\left(\frac{b_w}{v_{boil}}\right)}{T_{crit} - T_{trip}}, & p_{trip} \geq p_{amb} \end{cases} \tag{2.13}$$

Where, b_w is the van der Waals volume of the adsorbate ($cm^3 \cdot mol^{-1}$)

For adsorption temperature below the critical temperature of the adsorbate T_{crit}, the saturation pressure p_{sat} depends on the temperature of the adsorbate. For working pairs operating in an environment above the critical temperature, the pseudo saturation pressure is commonly used in the earlier studies, which is estimated using Dubinin's empirical equation as follows[16, 17]:

$$p_{sat} = \left(\frac{T}{T_{crit}}\right)^{k} p_{crit} \tag{2.14}$$

In the D-A adsorption isotherm model, the adsorption potential is a critical parameter that represents the thermodynamic driving force for adsorption. It is defined as the difference between the Gibbs free energy of the adsorbate in the normal liquid state and the adsorbed phase at the same temperature. Traditional adsorption isotherm models often rely on empirical formula based on the pseudo saturation pressure, which may not accurately reflect the actual adsorption behavior. Therefore, in this study, we proposed a new adsorption potential model that offers a more accurate and reliable approach to predicting the adsorption behavior of the working fluid.

$$A = G_{aded} - RT \ln p \tag{2.15}$$

Here, the Gibbs free energy of the adsorbed phase, G_{aded}, is given as,

$$G_{aded} = \kappa RT + \mu RT_{trip} \ln p_{trip} \tag{2.16}$$

Here, the parameters of κ and μ are evaluated through regression of the adsorption uptake data.

2.4.2.2 Tóth adsorption isotherms

The Tóth model, first proposed by Tóth in 1971, is a four-parameter model based on the Langmuir isotherm model, which takes into account the heterogeneity of the adsorbent surface. The equilibrium adsorption is calculated in the Tóth model using the following equation:

$$w = w_0 \frac{\beta p}{(1+(\beta p)^t)^{\frac{1}{t}}} \tag{2.17}$$

Where, t is the heterogeneity parameter in Tóth model (-). It is worth noting that

this parameter reflects the heterogeneity of the adsorbent surface. As t deviates further from unity, the distribution of adsorbate molecules and the energy of adsorption sites on the adsorbent surface become increasingly uneven. When t is 1, Tóth model simplifies to the Langmuir model, as shown in the following equation:

$$w = w_0 \frac{\beta p}{1+\beta p} \tag{2.18}$$

The parameter β is the affinity constant related to the binding affinity of the working pair (kPa^{-1}). Microscopically, this parameter represents the ratio of the adsorption rate and desorption rate, which reflects the adsorption capacity of the adsorbent surface for adsorbate molecules.

$$\beta = \beta_0 \exp\left(\frac{q_{st}}{RT}\right) \tag{2.19}$$

Here, β_0 is the affinity constant at T=∞, q_{st} is the isosteric heat of adsorption ($kJ \cdot mol^{-1}$).

Similar to the D-A model with pseudo saturation pressure, the Tóth model is also a four-parameter model, and the values of t, β, and q_{st} determined as constant values through linear regression analysis. It should be mentioned that the Tóth model provides a better fit to experimental data than the Langmuir model, especially in cases with non-ideal adsorption behavior or adsorbents with heterogeneous surfaces.

2.5 Results and Discussion

In this study, adsorption isotherms of MSC 30 with R32 are measured at 25 °C, 30 °C, 50 °C, 70 °C, 90 °C, 110 °C, 130 °C, 150 °C using magnetic suspension

adsorption measurement unit. The results obtained from the adsorption isotherm measurements, the absolute adsorption uptake correction, the validation of the improved adsorption potential model are discussed in the following sections.

Firstly, Figure 2.4 presents the isotherms of the adsorption/desorption process of MSC30-R32 refrigerant at different temperatures. It can be observed that there is no hysteresis in the adsorption and desorption processes at each temperature, and the curve shape conforms to the low Type I isotherm in the IUPAC classification.

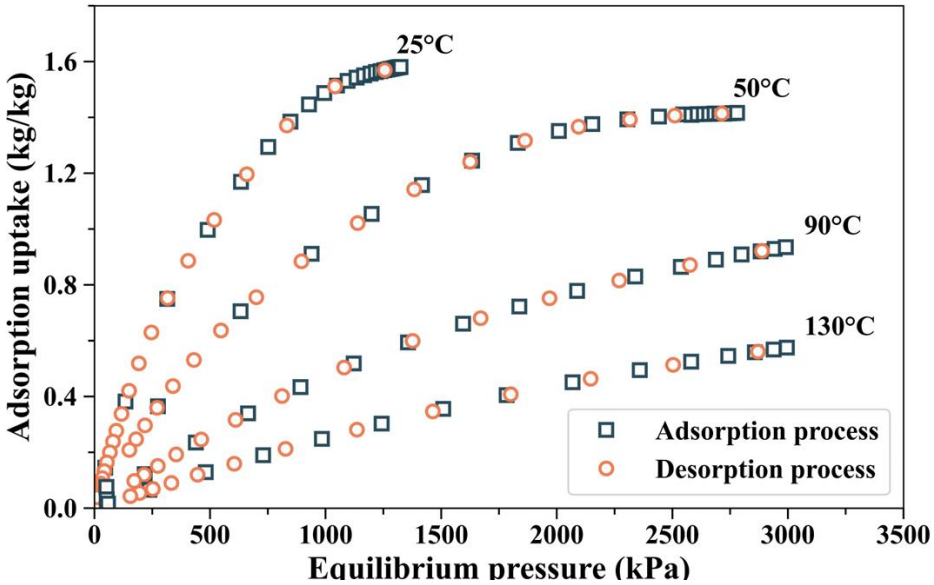

Figure 2.4 Adsorption/desorption isotherm of MSC30-R32 pair at 25°C-130°C

The adsorption isotherm data were fitted and analyzed using different adsorption isotherm models. During the analysis, the adsorbed phase volume correction with the Nikolayev and Dubinin model is invoked for both sets, and the absolute average deviation (AAD) and no-linear chi-squar (χ^2) are used to analyze the fitting error. The AAD is defined as,

$$AAD = \sum_{i=1}^{n_{exp}} \frac{|w_{exp,i} - w_{fit,i}|}{n_{exp}} \quad (2.20)$$

Where $w_{exp,i}$ and $w_{fit,i}$ are the experimental equilibrium uptake and calculated adsorption capacity, respectively. n_{exp} is the number of experiment data points.

The nolinear chi-squar (χ^2) is defined as,

$$\chi^2 = \sum \frac{(w_{exp} - w_{cal})^2}{w_{cal}^2} \quad (2.21)$$

2.5.1 Absolute Adsorption Uptake

The refrigerant molecules are adsorbed into the adsorption layer of the adsorbent, but the molecules in the free gas phase are not counted in the experimental excess uptake. With an increase in pressure, the number of refrigerant molecules which are adsorbed but not taken into account increases. To accurately depict the adsorption characteristics of R32 vapor on the MSC30 surface, absolute adsorption correction was carried out using the methods introduced in Section 2.4.1. Three correction methods were employed to calculate the absolute adsorption amount under operating conditions ranging from 25 °C to 150 °C and pressure ranging from 0 to 3000 kPa. The calculated results using different methods were compared and fitted with the D-A isotherm model.

Figure 2.5 (a) and (b) show the results of the absolute adsorption uptake calculated based on the 3 different correction methods. It can be observed that when using Method I for correction, the corrected results are always greater than the excess uptake, and the difference between the Method I correction uptake and the experimental results gradually increases with increasing pressure. The reason for this

phenomenon is that this method assumes that the volume of the adsorbed phase is equal to the pore volume of the adsorbent, and all the adsorbate molecules entering the porous structure of the adsorbent are considered to be in the adsorbed state. Based on the ideal gas law, with the increase of pressure, the density of the adsorbate gas increases, resulting in an increasing deviation of the Method I corrected results. On the other hand, for the results obtained using Method II, the calculation results are lower than the experimental results at low pressures, and the calculation results of Method II gradually exceed the excess uptake with increasing pressure and approach the absolute adsorption amount of Method I. As depicted in Figure 2.5 (b), the absolute adsorption values based on Method III tend to consistently exceed the experimental excess values, particularly under supercritical conditions. The difference between the two increases as the pressure increases.

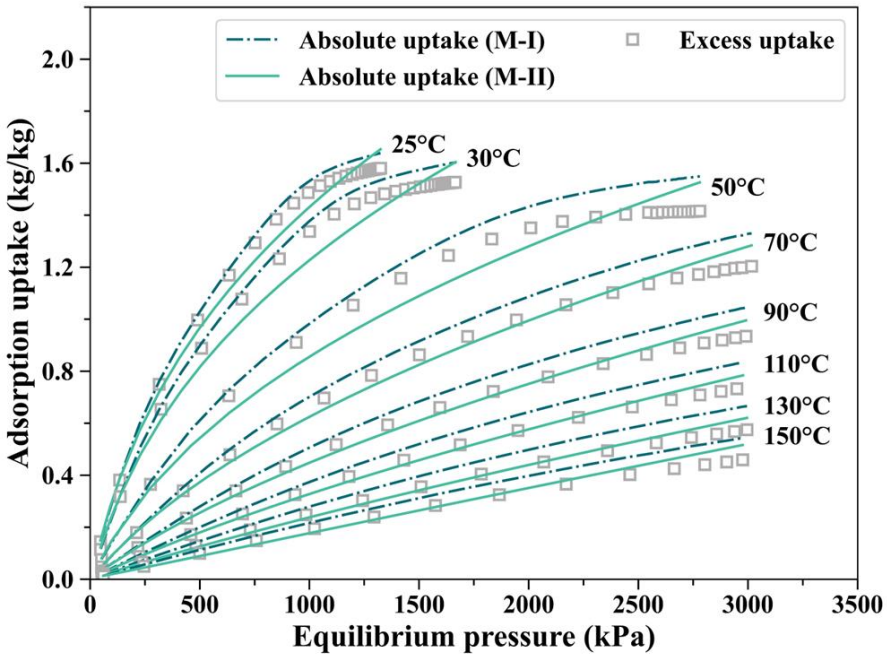

(a) Absolute uptake value of Method I and Method II

Further, the results with different absolute adsorption uptake correction methods

were fitted with the D-A isotherm model. The fitting performance was evaluated using AAD and χ^2, and the fitting parameters and performance are summarized in Table 2.4. The fitting errors of the three absolute adsorption correction methods were lower than that of the fitting without absolute adsorption correction. The direct fitting of excess uptake data with the D-A model showed the highest AAD error of 2.75, while the data corrected using Method III showed the lowest error of 2.47. Among the three absolute adsorption uptake correction methods, Method II showed higher fitting errors mainly because the fitting results differed greatly from the absolute adsorption amount below the critical temperature, as shown in Figure 2.6.

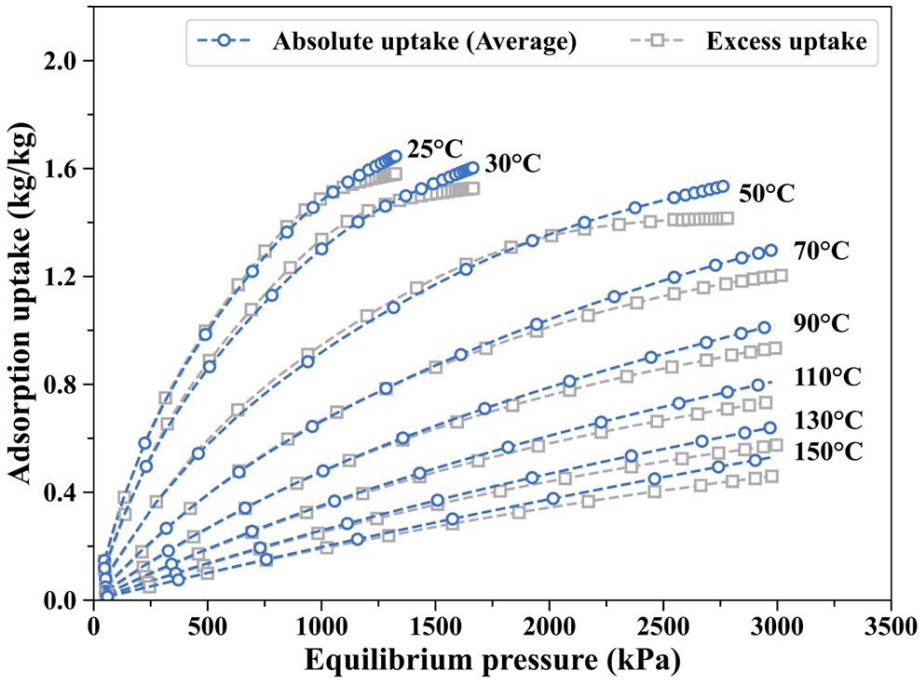

(b) Average value of Method I and Method II

Figure 2.5 Absolute adsorption uptake correction based on different methods

Table 2.4 Comparison of absolute adsorption correction methods in fitting D-A isotherm for MSC30-R32 pair

	Without absolute correction	With absolute correction		
		Method I	Method II	Method III
c_0 ($cm^3 \cdot g^{-1}$)	1.67	1.76	1.76	1.75
E ($J \cdot mol^{-1}$)	5433.97	5412.73	4949.36	5195.10
n	1.43	1.45	1.28	1.37
k	4.22	3.50	3.30	3.40
AAD	2.75	2.52	2.73	2.47
χ^2	0.73	0.74	0.79	0.54

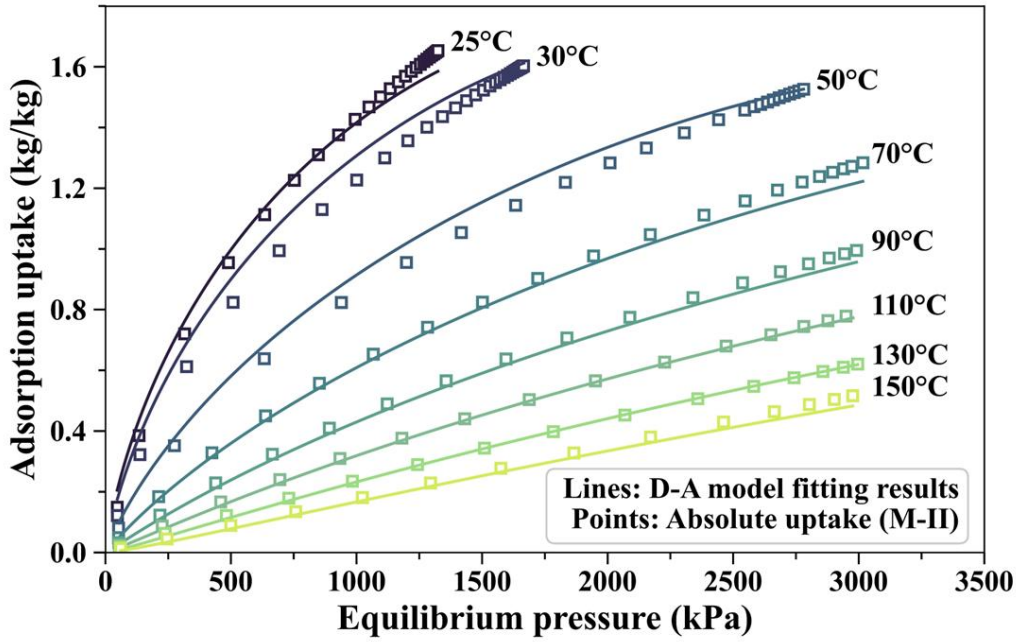

Figure 2.6 Isotherm fitting results of the D-A model with absolute adsorption correction Method II

The use of Method III for determining absolute adsorption quantities has been shown to provide the smallest fitting errors and the most accurate representation of true absolute adsorption quantities, which has also been demonstrated in previous

studies by Berdenova et al.[4], Therefore, the following data analysis was conducted using absolute adsorption uptake correction Method III.

2.5.2 Adsorption Isotherms Analysis

The adsorption isotherm of refrigerant R32 on MSC 30 was measured using the experimental setup shown in Figure 2.1, over a temperature range of 25°C to 150°C and a pressure range of 0-3000 kPa. The validity of the proposed adsorption potential model was initially assessed using the adsorption isotherm data of MSC30-R32 pair obtained from the experiments. The adsorption isotherm data were fitted using the Tóth model, D-A model with the pseudo saturation pressure, and modified D-A model with the proposed adsorption potential model, respectively. The volume correction of the adsorbed phase was taken into account, and AAD and χ^2 values were used to evaluate the fitting errors.

The fitting results are presented in Figure 2.7, and the parameters are summarized in Table 2.5. It is observed that the modified D-A model in combination with the proposed model fits the experimental data well, especially under supercritical conditions, with an AAD error of 2.42 and a χ^2 value of 0.48. The AAD fitting error of the modified D-A model is lower than that of the Tóth model by 0.45. Compared to the pseudo saturation pressure model, the proposed adsorption potential model also resulted in a higher level of accuracy. For the Tóth model at higher pressures, there is a large discrepancy between the predicted values and experimental data, but the proposed model performs well at higher pressures.

Table 2.5 Fitting parameters of the studied isotherm models for MSC30-R32 pair

Tóth model		Pseudo p_{sat}		Present model	
w_0 (kg·kg^{-1})	2.56	c_0 (cm^3·g^{-1})	1.75	c_0 (cm^3·g^{-1})	1.75
β_0 (kPa^{-1})	3.93E-08	E (J·mol^{-1})	5195.10	E (J·mol^{-1})	5133.35
q_{st} (kJ·mol^{-1})	26.81	n (-)	1.37	n (-)	1.37
t (-)	0.77	k	3.40	κ (-)	19.03
AAD	2.87	AAD	2.47	μ (-)	-2.31
χ^2	0.54	χ^2	0.54	AAD	2.42
				χ^2	0.48

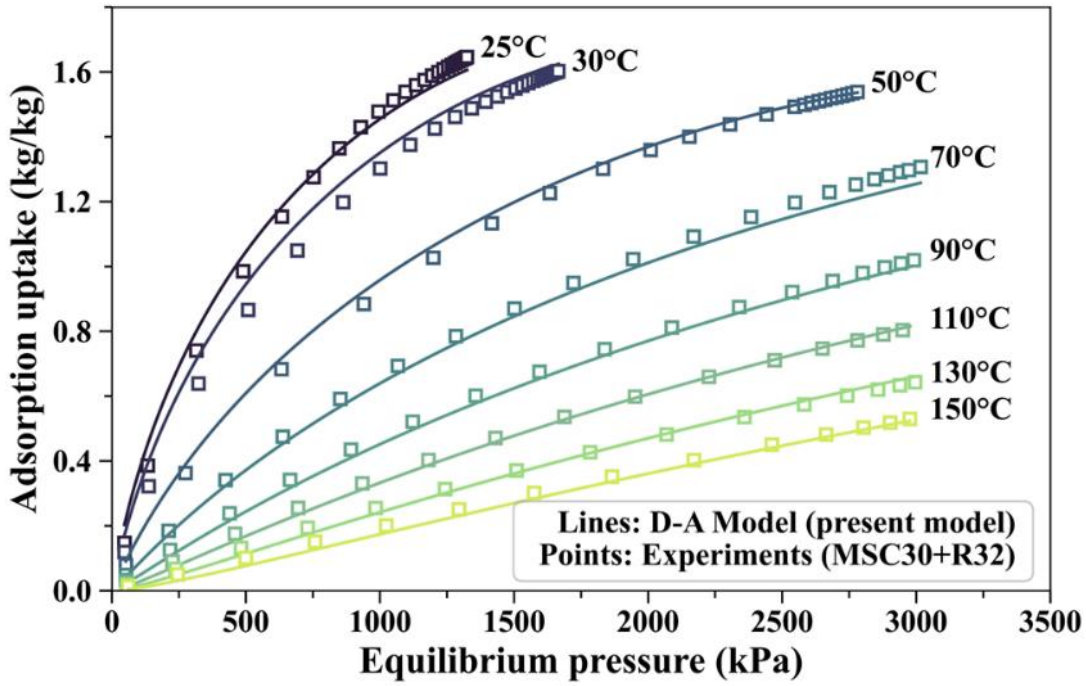

Figure 2.7 Absolute adsorption isotherms of MSC30-R32 pair. Points represent absolute uptake and lines represent the best fit using proposed model

2.5.3 Proposed Model Validation with Other Working Pairs

To thoroughly validate the effectiveness of the proposed model, the adsorption

isotherm data of other three sets of working pairs under supercritical conditions, including the adsorption of methane by MSC30[18], the adsorption of CO2 by MSC30 [19], and the adsorption of ethane by Chemviron activated carbon (AC)[20], were selected from the literature and subjected to fitting analysis using the present model. The required thermophysical properties for isotherm analysis are presented in Table 2.6.

The isotherm fitting results for each working pair are presented in Figure 2.8-Figure 2.10, and the corresponding fitting parameters are listed in Table 2.6. The experimental data for all the three working pairs from the literatures were well predicted by the proposed model, as evidenced by the good agreement between the model predictions and the experimental data. Specifically, the AAD errors were found to be 0.14, 2.01, and 0.26 for the three selected working pairs, indicating that the proposed model has high accuracy in predicting the adsorption behavior of different working pairs under supercritical conditions.

Table 2.6 Properties of refrigerants

Properties	Values		
Refrigerant	Methane	CO_2	Ethane
Critical temperature (°C)	-82.59	30.98	32.17
Critical pressure (kPa)	4599.20	7377.30	4872.20
Triple temperature (°C)	-182.46	-56.56	-182.78
Triple pressure (kPa)	11.70	517.96	0.00114
Specific volume at Triple point ($m^3 \cdot kg^{-1}$)	0.00221	0.00085	0.00153
Boiling Temperature (°C)	-161.48	-78.47	-182.78

Specific volume at boiling point ($m^3 \cdot kg^{-1}$)	0.00237	0.00080	0.00184
Van der Waals volume ($cm^3 \cdot mol^{-1}$)	0.00268	0.00097	0.00217
Molar mass ($g \cdot mol^{-1}$)	16.04	44.01	30.07

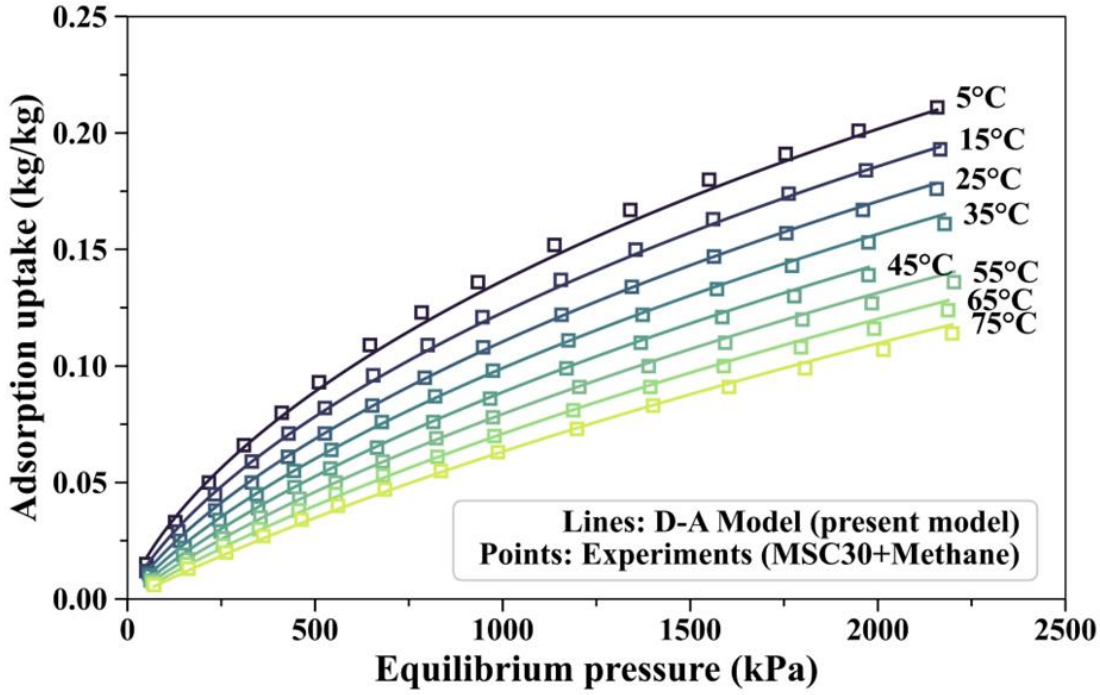

Figure 2.8 Isotherm fitting results of the present model for MSC30-methane pair

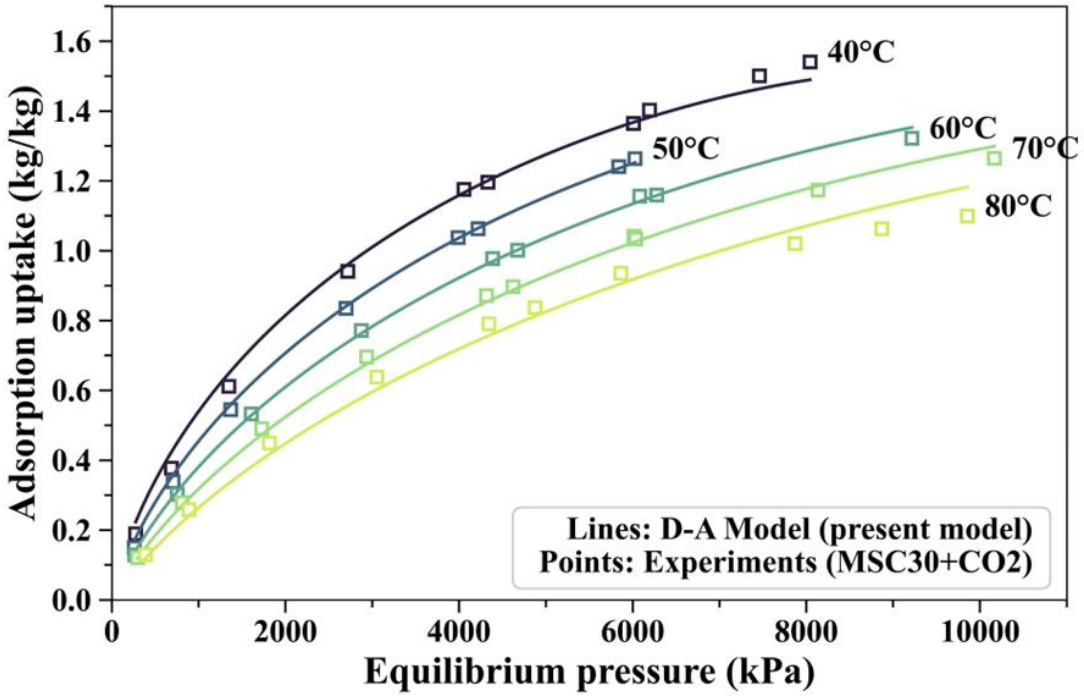

Figure 2.9 Isotherm fitting results of the present model for MSC30-CO_2 pair

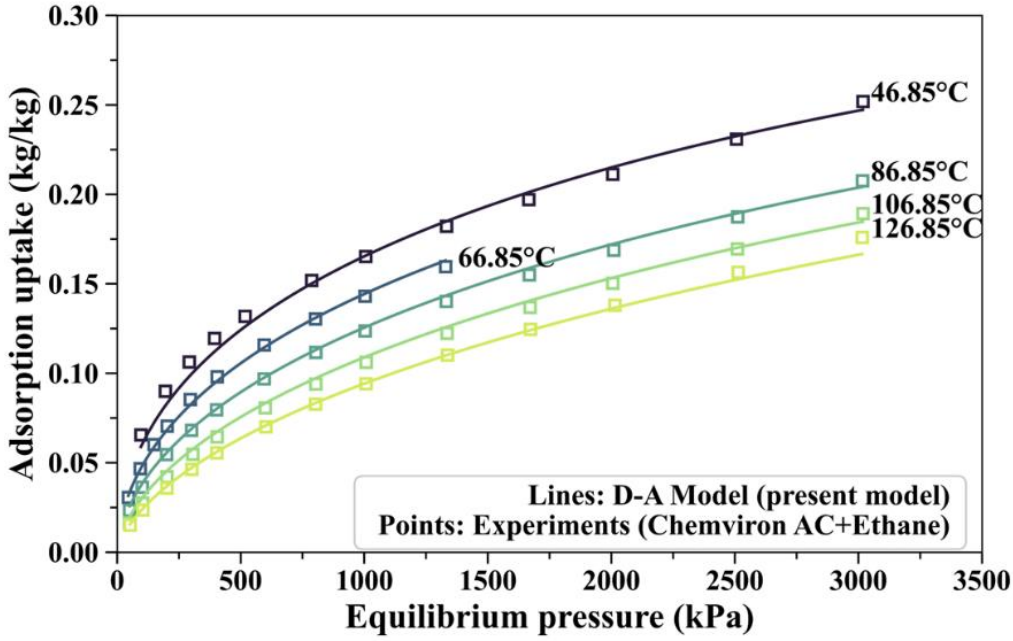

Figure 2.10 Isotherm fitting results of the present model for Chemviron AC-ethane pair

Table 2.7 Parameters for isotherm fitting using the modified D-A model with the proposed adsorption potential model

Adsorbent	MSC30	MSC30	Chemviron AC
Refrigerant	Methane	CO_2	Ethane
c_0 ($cm^3 \cdot g^{-1}$)	1.21	1.59	0.64
E ($J \cdot mol^{-1}$)	5158.23	5490.51	7313.98
n (-)	1.3	1.32	1.21
κ (-)	11.07	21.12	18.14
μ (-)	-2.29	-0.57	-69.87
AAD	0.14	2.01	0.26
χ^2	0.005	0.047	0.007

Table 2.8 Parameters for isotherm fitting using the D-A model with the pseudo saturation pressure equation

Adsorbent	MSC30	MSC30	Chemviron AC
Refrigerant	Methane	CO_2	Ethane
c_0 ($cm^3 \cdot g^{-1}$)	1.13	1.59	0.64
E ($J \cdot mol^{-1}$)	5399.1	5486.98	7339.15
n (-)	1.35	1.32	1.21
k (-)	2	4.95	2.45
AAD	0.13	2.03	0.27
χ^2	0.006	0.05	0.008

The adsorption isotherm data are also fitted and analyzed with the D-A model

with the pseudo saturation pressure. Table 2.8 shows the fitting parameters of the D-A model with the pseudo saturation pressure. The improved accuracy of the present model is also evident in the MSC30-CO_2 pair and the Chemviron AC-ethane pair, as its predictions exhibit smaller errors compared to those of the pseudo saturation pressure model. The proposed model exhibits superior fitting performance with smaller values of AAD error and χ^2 error, indicating that it provides a better overall fit to the adsorption isotherm experimental data. An exception to the improved accuracy of the present model is observed in the case of the MSC30-Methane pair, where the AAD error of the present model is slightly larger than that of the pseudo saturation pressure model. However, it should be noted that the absolute value of the errors for both models is rather small. The proposed model also has a smaller χ^2 error compared to the pseudo saturation pressure model, indicating a better fit to the experimental data. The results indicate that the proposed model exhibits excellent fitting performance for the adsorption isotherm experimental data. The model's fitting errors are smaller than that of the conventional empirical formula that relies on the pseudo saturation pressure.

2.6 Conclusion

In this chapter, adsorption equilibriums of MSC 30 with R32 have been measured experimentally using a magnetic suspension adsorption measurement unit. The measurements were taken over a range of temperatures between 25 °C to 150 °C and pressure up to 3000 kPa. An improved thermodynamic model of adsorption potential was devised for adsorption processes under supercritical conditions. The proposed

adsorption model was validated against experimental data from various working pairs. The proposed model demonstrated outstanding fitting performance for the experimental adsorption isotherm data, with the AAD error of 2.42 for the MSC30-R32 working pair. The fitting errors of the proposed model were observed to be smaller than that of Tóth adsorption isotherm model and the traditional empirical equation that relies on pseudo saturation pressure. These results highlight the potential of the proposed model as a valuable tool for accurately predicting adsorption isotherms in various adsorption systems.

2.7 Nomenclature

a_0-a_4	Coefficients for the specific heat capacity (-)
A	Adsorption potential ($J \cdot mol^{-1}$)
AAD	Absolute average deviation ($g \cdot kg^{-1}$)
b_0-b_3	Coefficients for the specific heat capacity (-)
b_w	van der Waals volume ($cm^3 \cdot mol^{-1}$)
c	Volume-based adsorption uptake ($cm^3 \cdot g^{-1}$)
c_0	Volume-based maximum uptake ($cm^3 \cdot g^{-1}$)
E	Characteristic energy of adsorption ($J \cdot mol^{-1}$)
G	Gibbs free energy ($J \cdot mol^{-1}$)
h	Specific enthalpy ($kJ \cdot kg^{-1}$)
k	Index of the pseudo-saturation equation (-)
mm	Molar mass ($g \cdot mol^{-1}$)
n	Heterogeneity parameter in D-A model (-)
n_{abs}	Absolute molar uptake ($mol \cdot g^{-1}$)
n_{exc}	Excess molar uptake ($mol \cdot g^{-1}$)
n_{exp}	Number of data points

p	Pressure (kPa)
q_{st}	isosteric heat of adsorption ($kJ \cdot mol^{-1}$)
R	Molar gas constant (8.314 $J \cdot mol^{-1} \cdot K^{-1}$)
t	Heterogeneity parameter in Tóth model (-)
T	Temperature (K)
v	Specific volume ($m^3 \cdot kg^{-1}$)
v_{pore}	Specific pore volume of adsorbent ($cm^3 \cdot g^{-1}$)
w	Equilibrium uptake in mass ratio ($kg \cdot kg^{-1}$)
w_0	Mass-based maximum uptake ($kg \cdot kg^{-1}$)
Greek symbols	
α	Thermal expansion coefficient (K^{-1})
β	Affinity constant (kPa^{-1})
β_0	Affinity constant at T=∞ (kPa^{-1})
δ	parameter of absolute uptake correction (-)
θ	Surface coverage (-)
μ	parameter of adsorption potential model (-)
κ	parameter of adsorption potential model (-)
φ	parameter of absolute uptake correction (-)
ρ	density ($kg \cdot m^{-3}$)
Subscript	
abs	Absolute
aded	Adsorbed phase
ads	Adsorbent/adsorption
amb	Ambient
atm	Atmospheric
ave	Average
boil	Normal boiling point
crit	Critical
des	Desorption
exc	Excess
exp	Experimental result
fit	Fitting result
gas	Gas phase
lat	Latent
ref	refrigerant
sat	Saturation
trip	Triple point

2.8 References

[1] K. Thu, Y.D. Kim, A. Bin Ismil, B.B. Saha, K.C. Ng. Adsorption characteristics of methane on Maxsorb III by gravimetric method, J. *Applied Thermal Engineering*. 72(2014) 200-205, doi: 10.1016/j.applthermaleng.2014.04.076.

[2] F. Rouquerol, K.S.W. Sing, G. Maurin. Adsorption by Powders and Porous Solids: Principles, Methodology and Applications, 2nd ed, 2014.

[3] J. Toth. Adsorption, 2002.

[4] B. Berdenova, A. Pal, M. Muttakin, S. Mitra, K. Thu, B.B. Saha, A. Kaltayev. A comprehensive study to evaluate absolute uptake of carbon dioxide adsorption onto composite adsorbent, J. *International Journal of Refrigeration-Revue Internationale Du Froid*. 100(2019) 131-140, doi: 10.1016/j.ijrefrig.2019.01.014.

[5] A. Pal, K. Uddin, K.A. Rocky, K. Thu, B.B. Saha. CO2 adsorption onto activated carbon-graphene composite for cooling applications, J. *International Journal of Refrigeration-Revue Internationale Du Froid*. 106(2019) 558-569, doi: 10.1016/j.ijrefrig.2019.04.022.

[6] K. Uddin, A. Pal, B.B. Saha. Improved CO2 adsorption onto chemically activated spherical phenol resin, J. *Journal of Co2 Utilization*. 41(2020), doi: ARTN 101255 10.1016/j.jcou.2020.101255.

[7] K.A. Rocky, A. Pal, M. Moniruzzaman, B.B. Saha. Adsorption characteristics and thermodynamic property fields of polymerized ionic liquid and polyvinyl alcohol based composite/CO2 pairs, J. *Journal of Molecular Liquids*. 294(2019), doi: 10.1016/j.molliq.2019.111555.

[8] A.L. Myers, P.A. Monson. Physical adsorption of gases: the case for absolute adsorption as the basis for thermodynamic analysis, J. *Adsorption*. 20(2014) 591-622, doi: 10.1007/s10450-014-9604-1.

[9] L. Zhou, S.P. Bai, W. Su, J. Yang, Y.P. Zhou. Comparative study of the excess versus absolute adsorption of CO2 on superactivated carbon for the near-critical

region, J. *Langmuir*. 19(2003) 2683-2690, doi: 10.1021/la020682z.

[10] Ya-Ping Zhou, Shu-Pei Bai, Li Zhou, B. Yang. Studies on the Physical Adsorption Equilibria of Gases on Porous Solids over a Wide Temperature Range Spanning the Critical Region—Adsorption on Microporous Activated Carbon, J. *Chinese Journal of Chemistry*. (2001), doi.

[11] M. Mozaffari Majd, V. Kordzadeh-Kermani, V. Ghalandari, A. Askari, M. Sillanpaa. Adsorption isotherm models: A comprehensive and systematic review (2010-2020), J. *Sci Total Environ*. 812(2022) 151334, doi: 10.1016/j.scitotenv.2021.151334.

[12] S. Seo, F. Miksik, Y. Maeshiro, K. Thu, T. Miyazaki. Performance Evaluation of an Adsorption Heat Pump System Using MSC-30/R1234yf Pair with the Impact of Thermal Masses, J. *Applied Sciences-Basel*. 11(2021), doi: ARTN 2279 10.3390/app11052279.

[13] K.A. Rahman, A. Chakraborty, B.B. Saha, K.C. Ng. On thermodynamics of methane plus carbonaceous materials adsorption, J. *International Journal of Heat and Mass Transfer*. 55(2012) 565-573, doi: 10.1016/j.ijheatmasstransfer.2011.10.056.

[14] S. Seo, H. Kawakami, F. Miksik, N. Takata, K. Thu, T. Miyazaki. Thermodynamic analysis and impact of thermal masses on adsorption cycles using MaxsorbIII/R245fa and SAC-2/R245fa pairs, J. *International Journal of Refrigeration*. 123(2021) 52-62, doi: 10.1016/j.ijrefrig.2020.12.005.

[15] M.M. Dubinin. Physical adsorption of gases and vapors in micropores, J. *Progress in Surface and Membrane Science*. 9(1975) 1–70, doi.

[16] K. Srinivasan, B.B. Saha, K.C. Ng, P. Dutta, M. Prasad. A method for the calculation of the adsorbed phase volume and pseudo-saturation pressure from adsorption isotherm data on activated carbon, J. *Phys Chem Chem Phys*. 13(2011) 12559-12570, doi: 10.1039/c1cp20383e.

[17] K.A.G. Amankwah, J.A. Schwarz. A Modified Approach for Estimating Pseudo-Vapor Pressures in the Application of the Dubinin-Astakhov Equation, J. *Carbon*. 33(1995) 1313-1319, doi: Doi 10.1016/0008-6223(95)00079-S.

[18] K.A. RAHMAN. Experimental and Theoretical Studies on Adsorbed Natural Gas

Storage System Using Activated Carbons, National University of Singapore, 2011.

[19] B.B. Saha, S. Jribi, S. Koyama, I.I. E-Sharkawy. Carbon Dioxide Adsorption Isotherms on Activated Carbons, J. *Journal of Chemical and Engineering Data*. 56(2011) 1974-1981, doi: 10.1021/je100973t.

[20] N. Tzabar, H.J.M. ter Brake. Adsorption isotherms and Sips models of nitrogen, methane, ethane, and propane on commercial activated carbons and polyvinylidene chloride, J. *Adsorption-Journal of the International Adsorption Society*. 22(2016) 901-914, doi: 10.1007/s10450-016-9794-9.

Chapter 3
Adsorption Thermodynamics of Activated Carbon-R32 Systems

3.1 Introduction

It is important to note that adsorption is a complex phenomenon influenced by various factors, such as temperature, pressure, and surface area, and therefore a comprehensive understanding of the thermodynamic properties is necessary to optimize the adsorption process. Adsorption isotherms provide fundamental characteristics of the interaction between adsorbent and adsorbate in the adsorption process. However, the description of adsorption process features is incomplete without thermodynamic parameters such as isosteric heat, specific heat capacity, entropy, enthalpy, etc. These thermodynamic parameters provide essential information and play a significant role in analyzing, calculating, and designing various adsorption-based applications by helping us to understand the thermodynamic characteristics and spontaneity of the adsorption phenomena. Therefore, the characterization of adsorption processes using thermodynamic parameters is crucial to the development of efficient adsorbent materials and the optimization of adsorption processes. Researchers in the field of adsorption have focused on developing theoretical frameworks and analyzing the thermodynamic characteristics of different working pairs. Chakraborty et al.[1] have proposed a theoretical framework for understanding the interaction between adsorbent-

adsorbate working pairs based on classical thermodynamics. They have used these models to study the adsorption enthalpy and specific heat of silica gel-water and activated carbon-methane working pairs. Jahan et al.[2] have investigated the adsorption characteristics and reaction mechanism of MOF801-water working pairs for use in adsorption refrigeration systems. They have analyzed the change in adsorption enthalpy during the adsorption process and compared the specific heat of the adsorbed phase with that of saturated liquid and vapor. Their findings indicate that the specific heat of the adsorbed phase is similar to that of saturated vapor at the beginning of the adsorption process, but it gradually becomes higher than that of saturated vapor as the adsorption uptake increases.

This chapter provides a detailed introduction and derivation of the theoretical framework for thermodynamic parameters of adsorption, including the adsorption enthalpy, specific heat capacity, entropy, and enthalpy of R32 vapor adsorbed on MSC30. Based on the adsorption potential model proposed in the previous chapter, the corresponding adsorption isosteric heat models with and without considering the volume correction of the adsorbed phase were derived and verified by comparing the data of different working pairs with classical models. Furthermore, based on experimental data of the adsorption uptake, this chapter calculates and analyzes the specific heat capacity, entropy, and enthalpy of the adsorbed phase of the MSC30-R32 working pair in the temperature range of 0-160 °C. The effects of temperature, pressure, and adsorption uptake on the thermodynamic properties of the working pair are evaluated, and comparisons with other working pairs are made. This research provides valuable insights into the thermodynamic behavior of adsorption systems and their potential applications in refrigeration and other fields.

3.2 Thermodynamic Frameworks

3.2.1 Isosteric Heat of Adsorption

The isosteric heat of adsorption refers to the heat released when a specific amount of adsorbent molecules are adsorbed on the surface of the adsorbent at a constant temperature[3]. Specifically, it represents the difference in the specific enthalpy between the adsorbate in its gaseous phase and the adsorbed phase. This is an important parameter for understanding the adsorption process and the interaction between the adsorbate and adsorbent[4]. It provides valuable insights into the thermodynamic behavior of the system and is often used to optimize the design and operation of adsorption-based systems in various industrial applications.

General expression for the isosteric of adsorption is given as[5],

$$q_{st} = T\left(v_{gas} - v_{aded}\right)\frac{\partial p}{\partial T}\Big|_{w} \tag{3.1}$$

Here, v_{gas} and v_{aded} are the specific volume of the gaseous phase and adsorbed phase, respectively ($m^3 \cdot kg^{-1}$), the pressure gradient at a fixed equilibrium adsorption amount $\frac{\partial p}{\partial T}\Big|_{w}$ is derived from the D-A isotherm model.

$$\ln p = \ln p_{sat} - \frac{E}{RT}(-\ln \theta)^{\frac{1}{n}} \tag{3.2}$$

Here, θ is the Surface coverage (-), which can be calculated by wv_{aded}/c_0, the characteristic energy of adsorption E ($J \cdot mol^{-1}$), the heterogeneity factor n and the volume-based maximum uptake c_0 ($cm^3 \cdot g^{-1}$), are the three fitting parameters of the D-A model.

The pressure gradient term is obtained as,

$$\frac{dp}{dT} = \frac{p}{p_{sat}} \cdot \frac{h_{fg}}{T(v_{satgas} - v_{satliq})} + \frac{pE}{RT^2}(-\ln\theta)^{\frac{1}{n}} \tag{3.3}$$

Here, v_{satgas} and v_{satliq} are the specific volume of the saturated vapor and saturated liquid, respectively ($m^3 \cdot kg^{-1}$)

When the specific volume of adsorbed phase is not neglected,

$$\frac{dp}{dT} = p \cdot \left[\frac{1}{p_{sat}} \frac{h_{fg}}{T(v_{satgas} - v_{satliq})} + \frac{E}{RT^2}\left[(-\ln\theta)^{\frac{1}{n}} + \frac{\alpha T}{n}(-\ln\theta)^{\frac{1}{n}-1}\right]\right] \tag{3.4}$$

Hence, the isosteric heat model with and without adsorbed phase volume correction are given by,

$$q_{st} = \begin{cases} h_{fg} + \frac{E}{mm}(-\ln\theta)^{\frac{1}{n}}, & T \le T_{crit} \\ \frac{kRT}{mm} + \frac{E}{mm}(-\ln\theta)^{\frac{1}{n}}, & T > T_{crit} \end{cases} \tag{3.5}$$

$$q_{st} = \begin{cases} h_{fg} + \frac{E}{mm}\left[(-\ln\theta)^{\frac{1}{n}} + \frac{\alpha T}{n}(-\ln\theta)^{\frac{1}{n}-1}\right], & T \le T_{crit} \\ \frac{kRT}{mm} + \frac{E}{mm}\left[(-\ln\theta)^{\frac{1}{n}} + \frac{\alpha T}{n}(-\ln\theta)^{\frac{1}{n}-1}\right], & T > T_{crit} \end{cases} \tag{3.6}$$

Here, below the critical temperature, the latent heat of adsorbate h_{fg} is required. For conditions above the critical temperature, kRT is substituted for the latent heat where the index k is obtained from the pseudo saturation pressure equation.

In the present work, the isosteric heat of adsorption is modelled by using the pressure gradient obtained from the modified isothermal adsorption model.

$$\ln p = \frac{G_{aded} - E(-\ln\theta)^{1/n}}{RT} \tag{3.7}$$

The general expression of the isosteric heat model with and without volume correction can be written as,

$$q_{st} = \frac{p}{R}(v_{gas} - v_{aded}) \cdot \left[\frac{dG_{aded}}{dT} - \frac{G_{aded} - E(-\ln\theta)^{\frac{1}{n}}}{T}\right] \tag{3.8}$$

$$q_{st} = \frac{p}{R}\left(v_{gas} - v_{aded}\right) \cdot \left[\frac{dG_{aded}}{dT} + E\frac{\alpha}{n}(-\ln\theta)^{\frac{1}{n}-1} - \frac{G_{aded}-E(-\ln\theta)^{\frac{1}{n}}}{T}\right] \quad (3.9)$$

3.2.2 Adsorbed Phase Specific Heat Capacity

In the simulation and design of adsorption systems, the specific heat capacity of the adsorbent and adsorbate is of paramount importance[6]. The specific heat capacity of the adsorbent-adsorbate working pair directly impacts the performance of the adsorption system, and the enthalpy and entropy of the working pair are highly dependent on the specific heat capacity. Therefore, accurate knowledge of the specific heat capacity of the adsorbent-adsorbate working pair is crucial for optimizing the performance of adsorption systems. Additionally, this property must be considered in the design of adsorption heat pumps to ensure efficient and effective heat transfer.

Several factors can affect the specific heat capacity of the adsorbate-adsorbent pair, such as the type of adsorbent and adsorbate, temperature and pressure conditions. For a considerable period of time, certain researchers have presumed that the state of the refrigerant following adsorption is comparable to either the liquid or gaseous state, and thus, they have employed the specific heat capacity of liquid or gaseous refrigerant in their computations, rather than the specific heat capacity in the adsorbed state[7, 8]. This approach inevitably leads to calculation inaccuracies. In recent years, it has become widely accepted that the adsorbed adsorbate is a unique phase known as the adsorbed phase, and its specific heat capacity is defined as the first-order partial derivative of the enthalpy of the adsorbed phase with respect to temperature, at a constant adsorption loading[1, 9, 10]. This expression can be represented as:

$$c_{p,aded} = \left(\frac{\partial h_{aded}}{\partial T}\right)_{w} \quad (3.10)$$

The enthalpy of the adsorbed phase h_{aded} can be obtained through the definition

of adsorption heat.

$$q_{st} = h_{gas} - h_{aded} \tag{3.11}$$

$$c_{p,aded} = \left(\frac{\partial h_{gas}}{\partial T}\right)_p - \left(\frac{\partial q_{st}}{\partial T}\right)_w = c_{p,gas} - \left(\frac{\partial q_{st}}{\partial T}\right)_w \tag{3.12}$$

The formula for adsorption heat discussed in Section 3.2.1 can be substituted into the equation to obtain the specific heat capacity of the adsorbed phase,

$$\left(\frac{\partial q_{st}}{\partial T}\right)_w = \left(\frac{\partial h_{fg}}{\partial T}\right)_p - \frac{E}{mm} \cdot \frac{\alpha^2(1-n)T}{n^2}\left[-\ln\left(\frac{wv_{aded}}{c_0}\right)\right]^{\frac{1-2n}{n}} \tag{3.13}$$

Here, the characteristic energy of adsorption E (J·mol^{-1}), the heterogeneity factor n and the volume-based maximum uptake c_0 (cm^3·g^{-1}), are the three fitting parameters of the D-A model.

$$c_{p,aded} = c_{p,gas} - \left(\frac{\partial h_{fg}}{\partial T}\right)_p + \frac{E}{mm} \cdot \frac{\alpha^2(1-n)T}{n^2}(-\ln\theta)^{\frac{1-2n}{n}} \tag{3.14}$$

Here, h_{fg} is the latent heat of evaporation (kJ·kg^{-1}). According to the definition, the partial derivative of the latent heat with respect to temperature $\frac{\partial h_{fg}}{\partial T}$ can also be expressed as $c_{p,gas} - c_{p,satliq}$.

$$\left(\frac{\partial h_{fg}}{\partial T}\right)_p = c_{p,gas} - c_{p,satliq} \tag{3.15}$$

Here, $c_{p,gas}$ and $c_{p,satliq}$ respectively represent the specific heat capacity of gaseous adsorbate and liquid adsorbate.

Therefore, for the adsorbed phase below the critical temperature, by substituting the above Eq.(3.15), the $c_{p,aded}$ can be expressed as:

$$c_{p,aded} = c_{p,satliq} + \frac{E}{mm} \cdot \frac{\alpha^2(1-n)T}{n^2}(-\ln\theta)^{\frac{1-2n}{n}} \tag{3.16}$$

For conditions above the critical temperature, the latent heat of evaporation cannot

be obtained, and typically, the term $\frac{kR}{mm}$ is used instead of h_{fg}.

$$c_{p,aded} = c_{p,gas} - \frac{kR}{mm} + \frac{E}{mm} \cdot \frac{\alpha^2(1-n)T}{n^2}(-\ln\theta)^{\frac{1-2n}{n}} \tag{3.17}$$

In the simulation and design of adsorption systems, it's crucial to consider the specific heat capacity of not only the adsorbent in adsorbed phase but also other system components such as the adsorbate and the metal pipes and fins in the heat exchanger. The specific heat capacity of the adsorbate-adsorbent working pair can be estimated by considering the sum of the specific heat capacities of the adsorbent $c_{p,ads}$ and the adsorbate in the adsorbed phase $c_{p,aded}$ [11], which is give as,

$$c_{p,tot} = c_{p,ads} + w \cdot c_{p,aded} \tag{3.18}$$

Here, $c_{p,tot}$ is the specific heat capacity of the adsorbent-adsorbate working pair in total ($kJ \cdot kg^{-1} \cdot K^{-1}$), $c_{p,ads}$ is the specific heat capacity adsorbent. For the MSC30 adsorbent used in this work, the specific heat capacity is given by,

$$c_{p,ads}(T) = a_0 + a_1 T + a_2 T^2 + a_3 T^3 + a_4 T^4 \tag{3.19}$$

The coefficients used in Eq. (3.25) is given in Table 3.1

Table 3.1 Coefficients for the specific heat capacity of the adsorbent

Coefficient	MSC 30[12]
a_0	27987.4
a_1	-312.06
a_2	1.32895
a_3	-0.00249144
a_4	1.74482×10^{-6}

3.2.3 Adsorbed Phase Entropy

In addition to sensible and adsorption heat, the enthalpy and entropy of the adsorbate should be given sufficient attention in the design and implementation of adsorption systems. It is well-known that the entropy of the adsorbed phase $ds_{aded}(T,p,w)$ is a function of temperature, pressure, and adsorption uptake[1, 10], and is typically expressed as follows:

$$ds_{aded} = \left(\frac{\partial s_{aded}}{\partial T}\right)_{p,w} dT + \left(\frac{\partial s_{aded}}{\partial p}\right)_{T,w} dp + \left(\frac{\partial s_{aded}}{\partial w}\right)_{T,p} dw \tag{3.20}$$

In the above equation, the first term on the right-hand side $\left(\frac{\partial s_{aded}}{\partial T}\right)_{p,w}$ can be replaced with $\frac{c_{p,aded}}{T}$.

$$\frac{\partial s_{aded}}{\partial T} \approx \frac{c_{p,aded}}{T} \tag{3.21}$$

From the Maxwell relationship,

$$\frac{\partial s_{aded}}{\partial p} = -\frac{\partial v_{aded}}{\partial T} \tag{3.22}$$

As discussed in Section 2.4.2 The time derivative of the specific volume of the adsorbed phase can be expressed as:

$$\frac{\partial v_{aded}}{\partial T} = \alpha \cdot v_{aded} \tag{3.23}$$

For the last term on the right-hand side in Eq.(3.14)

$$\left(\frac{\partial s_{aded}}{\partial w}\right)_{T,P} = \left(\frac{\partial s_{aded}}{\partial p}\right)_{T,w} \left(\frac{\partial p}{\partial w}\right)_{T} \tag{3.24}$$

The entropy of the adsorbed phase can be written as:

$$ds_{aded} = \frac{c_{p,aded}}{T}dT - \alpha v_{aded}dp - \alpha v_{aded}\left(\frac{\partial P}{\partial w}\right)_T dw \tag{3.25}$$

Based on the D-A equation, the partial term $\left(\frac{\partial P}{\partial w}\right)_T$ can be written as:

$$\left(\frac{\partial P}{\partial w}\right)_T = \frac{wP}{n}\frac{\ln\left(\frac{p_{sat}}{p}\right)}{-\ln\theta} \tag{3.26}$$

Hence, the derivative of the entropy of the adsorbed phase can be expressed as:

$$ds_{aded} = \frac{c_{p,aded}}{T}dT - \alpha v_{aded}dp - \alpha v_{aded}\frac{wp}{n}\frac{\ln\left(\frac{p_{sat}}{p}\right)}{-\ln\theta} \tag{3.27}$$

Entropy is a path-independent property, and the entropy of a particular state point $s_{aded}(p,T,w)$ can be determined by continuously integrating between the reference point $s(p_0,T_0,w_0)$ and the point of desired state[1]. It is noticed that the reference point for calculation of thermodynamic properties is selected as the triple point of the adsorbate[13].

$$s_{aded} = s(p_0,T_0,w_0) + \int_{T_0}^{T}\left[\frac{c_{p,gas}}{T} + \frac{\alpha^2(1-n)}{n^2}E(-ln\,\theta)^{\frac{1-2n}{n}} - \frac{1}{T}\left(\frac{\partial h_{fg}}{\partial T}\right)_p\right]dT - \int_{p_0}^{p}\alpha v_{aded}dP - \int_0^w \alpha v_{aded}\frac{wp}{n}\frac{ln\left(\frac{p_{sat}}{p}\right)}{-ln\,\theta}dw \tag{3.28}$$

In the system of adsorbent-adsorbate working substance, as discussed in Section 3.2.2, the thermodynamic properties of the adsorbent itself cannot be ignored. Therefore, the total entropy of the adsorbent-adsorbate working pair system can be expressed as:

$$s_{tot} = s_{ads} + w \times s_{aded} \tag{3.29}$$

Where, the entropy of the adsorbent s_{ads} can be obtained simply by:

$$s_{ads} = \int_{T_0}^{T}\frac{c_{p,ads}}{T}dT \tag{3.30}$$

3.2.4 Adsorbed Phase Enthalpy

On the other hand, the differential enthalpy of the adsorbed phase can be obtained from the Gibbs free energy equation[9].

$$dh_{aded} = Tds_{aded} + v_{aded}dp \tag{3.31}$$

Using the ds_{aded} expression in equation (3.27), the above equation becomes:

$$dh_{aded} = c_{p,aded}dT + v_{aded}(1 - \alpha T)dp - \frac{\alpha v_{aded} Twp}{n} \frac{\ln\left(\frac{p_{sat}}{p}\right)}{-\ln\theta} dw \tag{3.32}$$

Analogously, the enthalpy is a property independent of the path, and the enthalpy of a given state point $h_{aded}(p, T, w)$ can be ascertained by carrying out an integration between the reference point $h(p_0, T_0, w_0)$ and the said point[1]. The triple point of the refrigerant is chosen as the reference point[13]. Thus, the enthalpy of the adsorbed phase becomes:

$$h_{aded} = h(p_0, T_0, w_0) + \int_{T_0}^{T} \left[c_{p,gas} + \frac{\alpha^2(1-n)}{n^2} ET(-\ln\theta)^{\frac{1-2n}{n}} - \left(\frac{\partial h_{fg}}{\partial T}\right)_p \right] dT -$$

$$\int_{p_0}^{p} v_{aded}(1 - \alpha T)dp - \int_0^w \frac{\alpha v_{aded} Twp}{n} \frac{ln\left(\frac{p_{sat}}{p}\right)}{-ln\,\theta} dw \tag{3.33}$$

The total enthalpy of the adsorbent-adsorbate working pair system can be expressed as:

$$h_{tot} = h_{ads} + w \times h_{aded} \tag{3.34}$$

Here, h_{ads} is the enthalpy of the adsorbent, which is obtained by,

$$h_{ads} = \int_{T_0}^{T} c_{p,ads}dT + \int_{p_0}^{p} v_{ads}dp \tag{3.35}$$

3.3 Results and Discussion

3.3.1 Isosteric Heat of Adsorption

To verify the reliability of the new proposed isosteric heat model, the comparison of the isosteric heat of adsorption between the present models and Rahman's model, with and without adsorbed phase volume correction, was performed. Rahman's model is a well-established model that has been widely used in adsorption studies, and its accuracy has been verified in previous works[9]. Figure 3.1 and Figure 3.2 depict the isosteric heat of adsorption plotted against coverage for the selected working pairs, demonstrating the present model's performance compared to Rahman's model.

As can be seen from Figure 3.1 and Figure 3.2, the isosteric heat calculated by the present model shows a good agreement with the results of the Rahman model, both with and without volume correction applied. The present model exhibits a high degree of concordance with the Rahman model across all four selected working pairs. Moreover, the isosteric heat decreased as the uptake increased, and the inclusion of the volume correction consistently resulted in higher values of the isosteric heat as compared to the model without volume correction. The difference between the isosteric heat obtained from the models that consider and do not consider the volume correction increased as the extent of adsorption increased. This result suggests that the effect of the volume correction becomes more significant as the number of adsorbed molecules increases.

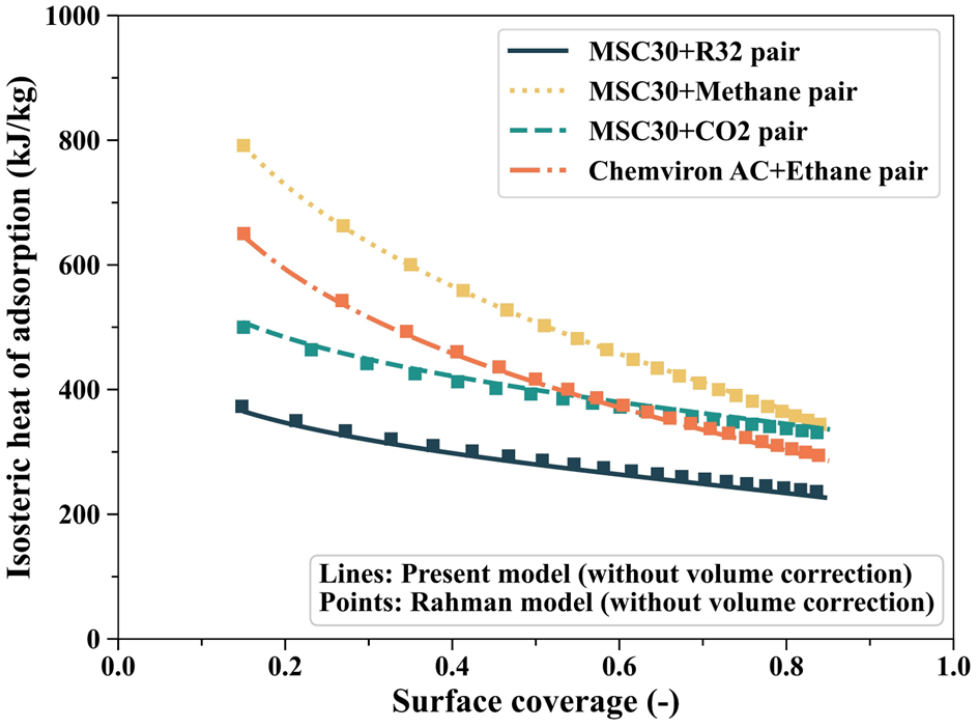

Figure 3.1 Isosteric heat of adsorption validation (without volume correction)

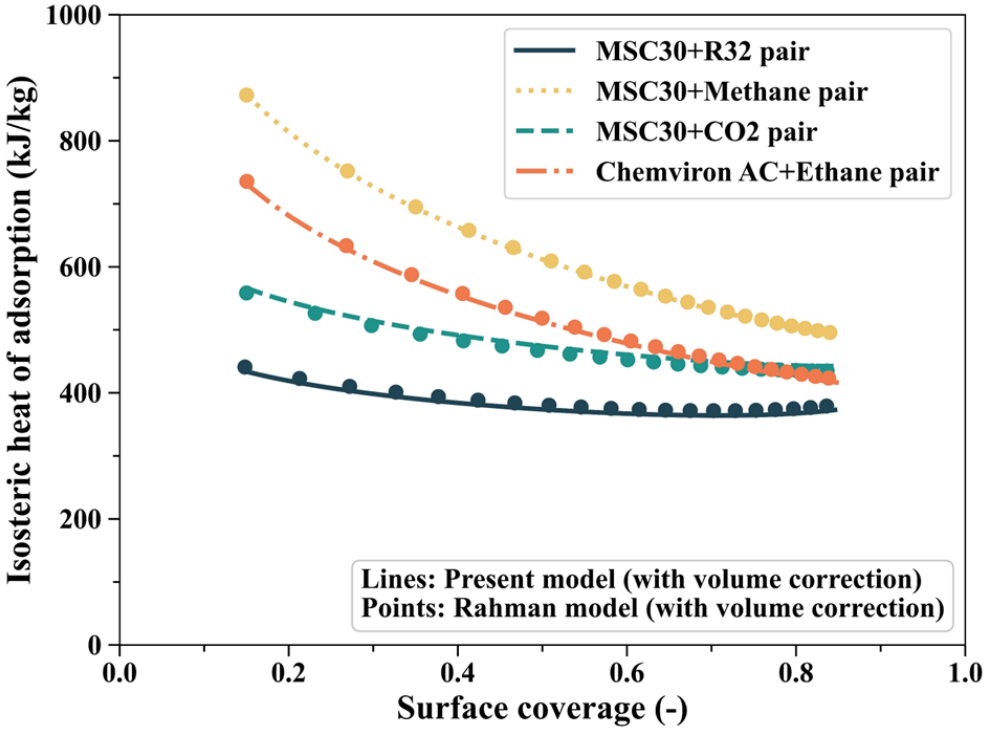

Figure 3.2 Isosteric heat of adsorption validation (with volume correction)

In consideration of the fact that the effect of the adsorbed phase volume correction on the isosteric heat of adsorption cannot be neglected, especially at high surface coverage (around 0.8), the subsequent equilibrium cycle analysis uses the isosteric heat model with the volume correction taken into account.

The adsorption heat of MSC30-R32 under supercritical and subcritical temperature conditions was calculated using Eqs. (3.8)-(3.9) and plotted in Figure 3.3 (a) and (b), respectively. As shown in the figures, the isosteric heat of adsorption decreases as the surface coverage increases. This phenomenon is attributed to the fact that, at the beginning of the adsorption process, there are many empty adsorption sites on the adsorbent surface. When refrigerant gas molecules come into contact with the adsorbent surface, they are simultaneously attracted to multiple active adsorption sites and form van der Waals bonds with them. This results in the release of a large amount of energy and a high adsorption isosteric heat. As the adsorption process continues, the adsorption sites on the adsorbent surface gradually become saturated, and subsequent refrigerant molecules can only bind to inactive adsorption sites. The reduced interaction between the refrigerant molecules and the adsorbent leads to a decrease in bonds and van der Waals thus a lower isosteric heat.

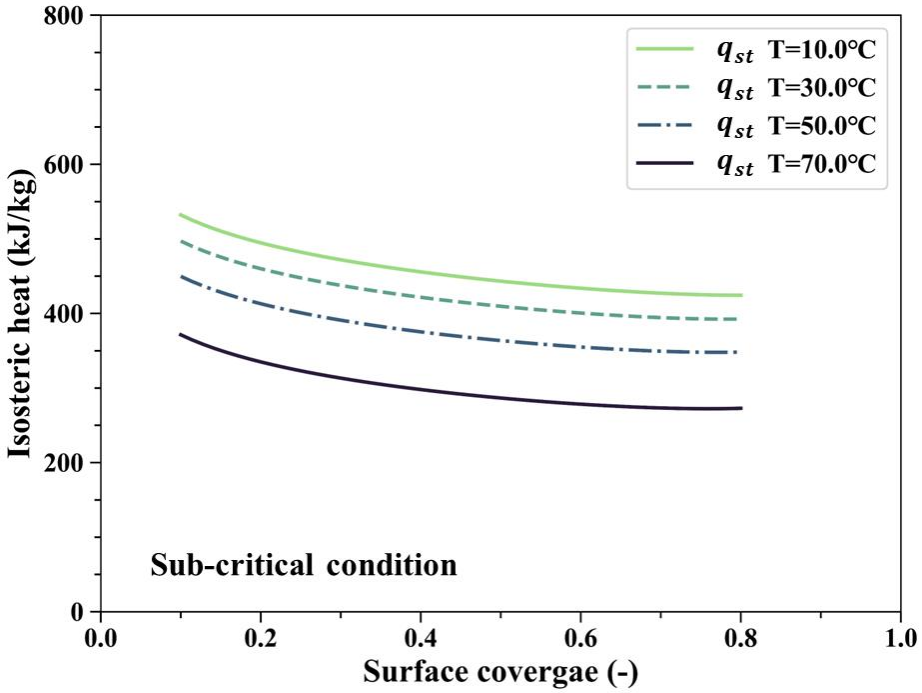

(a) Isosteric heat variation at super-critical conditions

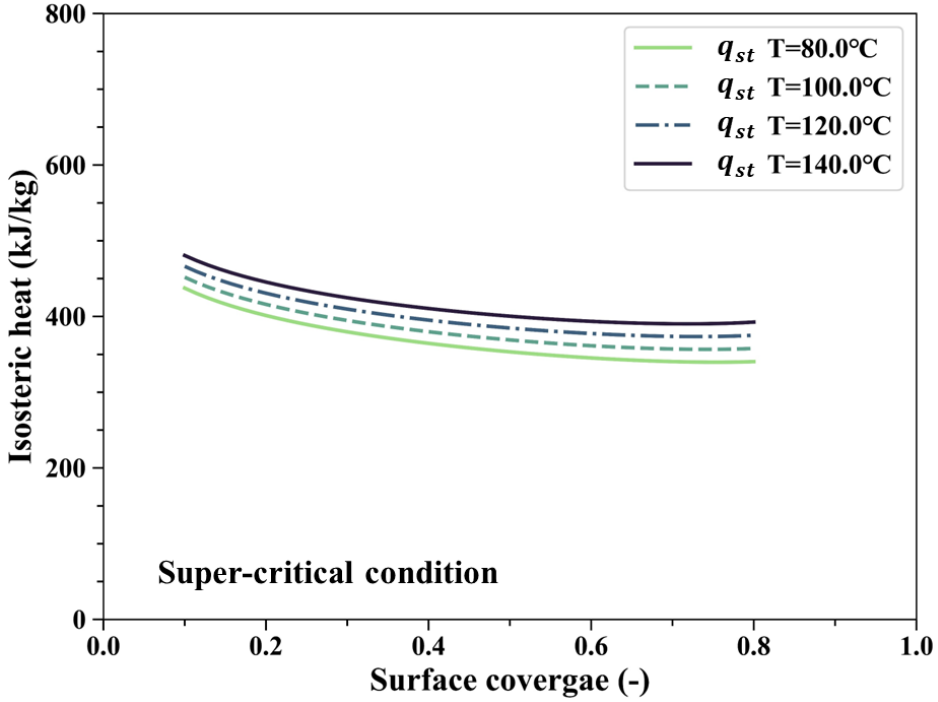

(b) Isosteric heat variation at super-critical conditions

Figure 3.3 Isosteric heat of the MSC30-R32 working pair variation with respect to surface coverage and temperature at both sub-critical and super-critical conditions

Moreover, the plots reveal that under sub-critical conditions, the adsorption heat decreases with an increase in temperature at the same adsorption loading. However, when adsorption occurs at the super critical temperature, the trend is reversed, and the adsorption heat gradually increases with temperature. This is due to the significant influence of refrigerant evaporation heat on the adsorption heat at temperatures below the critical point. With increasing temperature, the evaporative heat decreases, leading to a decrease in the adsorption heat. However, under supercritical conditions, the Gibbs free energy slowly increases with temperature, resulting in a gradual increase in the adsorption heat.

3.3.2 Adsorbed Phase Specific Heat Capacity

As a crucial physical quantity in designing and simulating adsorption systems, the specific heat capacity of the adsorbate in adsorbed phase ($c_{p,aded}$) is influenced by the temperature, pressure, and adsorption loading conditions. Understanding the behavior of specific heat can help optimize the performance of adsorption systems and improve their energy efficiency. Its value can be calculated using Eqs (3.10)-(3.19) The specific heat performance of the MSC30-R32 working fluid under different operating conditions is analyzed below.

Figure 3.4 illustrates the variation of the specific heat of the adsorbed phase with temperature under sub-critical and super-critical conditions. For temperatures above the critical temperature, pressures ranging from 100 kPa to 3000 kPa are considered. For temperatures below the critical temperature, the absolute adsorption uptake is set at 1.36 ($kg \cdot kg^{-1}$) and the surface coverage is 0.82. These values correspond to the maximum adsorption uptake achievable by the MSC30-CO2 working pair in an adsorption heat

pump system operating at an adsorption temperature of 30 °C and an evaporation temperature of 7 °C. The influence of temperature on the specific heat of saturated liquid and vapor of R32 can also be seen in the Figure 3.5

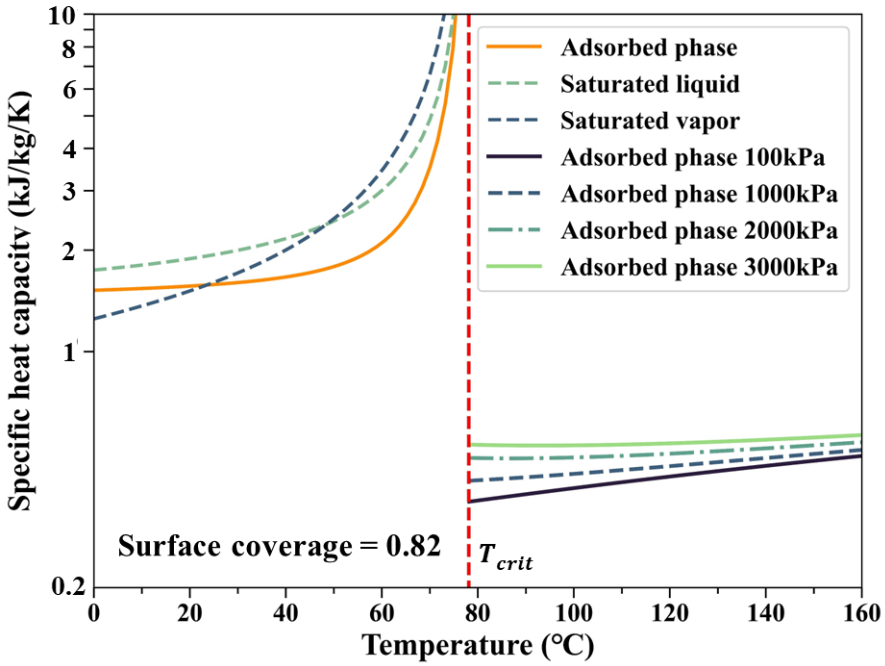

Figure 3.4 Specific heat capacity of the adsorbed phase of MSC30-R32 Pair for both sub-critical and super-critical conditions

From Figure 3.4, it can be observed that below the critical temperature, the specific heat capacity of the adsorbed phase gradually increases with the temperature, and the rate of specific heat capacity growth increases faster as the temperature approaches the critical temperature. This can be mainly attributed to the significant influence of the specific heat capacity of the saturated liquid on the adsorbed phase specific heat capacity. At a surface coverage of 0.82, the specific heat capacity of the adsorbed phase is slightly lower than that of the saturated liquid, and as the temperature approaches the critical temperature, it becomes closer to the saturated liquid specific heat capacity. As discussed in Section 2.5.2, the value of the heterogeneity factor n is greater than 1, so

in Eq (3.16), the second term on the right-hand side is negative, indicating that the specific heat capacity of the adsorbed phase is always lower than that of the saturated liquid phase.

Under conditions where the temperature is above the critical temperature, there is no saturated liquid or saturated vapor, and thus the specific heat capacity of gaseous refrigerants is used to calculate the adsorbed phase specific heat capacity. It can be observed that the specific heat capacity of the adsorbed phase is generally lower when the temperature is above the critical temperature than when it is below. As the temperature increases, the specific heat capacity of the adsorbed phase increases, but the rate of increase is very slow. With increasing pressure, the adsorbed phase specific heat capacity also slightly increases.

The changes in the specific heat of the adsorbed phase with respect to different surface coverages are illustrated in. It is evident that, as the surface coverage increases, the interpolation of the adsorbed phase specific heat with the specific heat of the saturated liquid becomes larger. At a surface coverage of 0.5, the adsorbed phase specific heat capacity is observed to be nearly equivalent to the value of the saturated liquid. Hence, at low surface coverage, the specific heat capacity of the saturated liquid can be utilized to approximate the value of the adsorbed phase. Nevertheless, at higher surface coverage, this substitution can result in an overestimation of the adsorbed phase specific heat capacity. Moreover, in the super-critical operating condition, the disparity between the specific heat capacity of the gaseous refrigerant and the adsorbed phase cannot be disregarded. If the specific heat capacity of the refrigerant in gaseous phase is simply employed to substitute that of the adsorbed phase, it will lead to an overestimation of the calculated result.

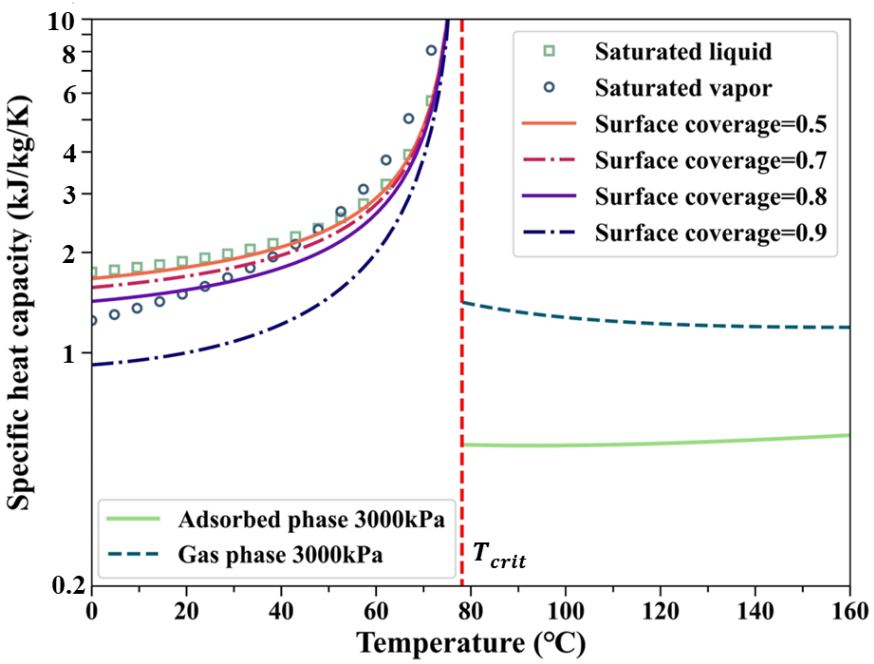

Figure 3.5 Specific heat capacity of the adsorbed phase under different surface coverage

Further, the specific heat capacity of the MSC30-R32 working pair system was calculated using Eqs. (3.16)-(3.19). The specific heat capacity of MSC30 was obtained through a polynomial empirical formula (3.19)[3]. Figure 3.6 shows the relationship between the total specific heat capacity $c_{p,tot}$ and pressure for the refrigerant under both sub-critical and super-critical conditions. It can be observed that the total specific heat capacity of the system increases with pressure, regardless of whether it is under supercritical or subcritical conditions. When the pressure is 0 kPa, there are no refrigerant molecules adsorbed on the surface of MSC30, and the specific heat capacity is that of the adsorbent itself. Under subcritical conditions, the total specific heat capacity gradually increases with temperature, as confirmed in, which is also verified in Figure 3.4. However, under supercritical conditions, the total specific heat capacity increases with temperature in the low-pressure region but exhibits the opposite trend in the high-pressure region.

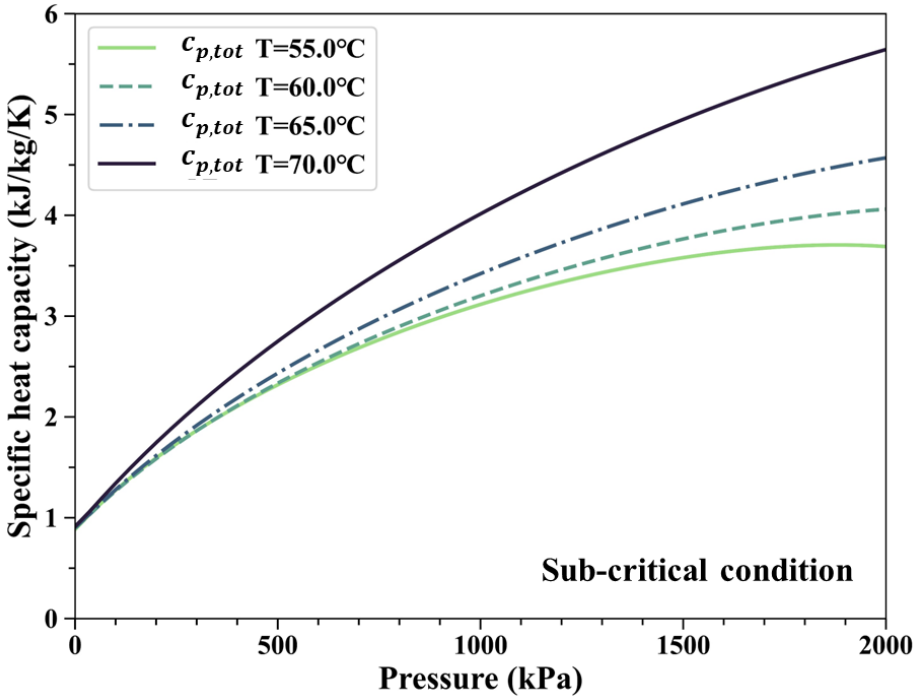

(a) Total specific heat capacity variation at super-critical conditions

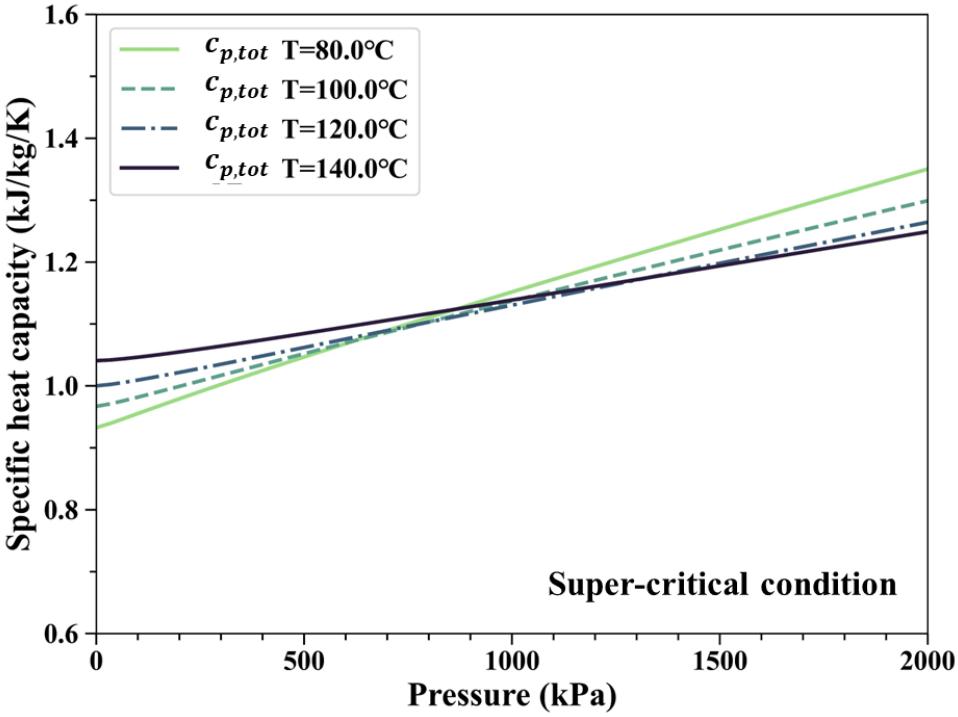

(b) Total specific heat capacity variation at super-critical conditions

Figure 3.6 Total specific heat capacity of the MSC30-R32 working pair variation with respect to pressure and temperature at both sub-critical and super-critical conditions

Comparing Figure 3.6 (a) and (b), it can be found that, under the same pressure, the total specific heat capacity under subcritical conditions is always greater than that under supercritical conditions. This is due to the fact that the specific heat capacity of the adsorbed phase under super-critical conditions is lower than that under sub-critical conditions.

Moreover, the dependence of the specific heat capacity of the MSC30-R32 working pair on the surface coverage (relative adsorption loading) can be obtained from Figure 3.7. It can be observed that under both super-critical and sub-critical conditions, the total specific heat capacity of the system increases almost linearly with the increase in surface coverage and reaches a maximum at around surface coverage of 0.8, followed by a gradual decrease. This is mainly due to the heterogeneity factor n of MSC30-R32 working pair having a value greater than 1, which causes the term related to surface coverage in the specific heat capacity calculation equations to be negative (the second term on the right-hand side of equation (3.16) and the third term on the right-hand side of equation (3.17)). As a result, as the surface coverage increases, the influence of these terms gradually increases, leading to a gradual decrease in the total specific heat capacity.

It can also be seen from Figure 3.7 (a) and (b) that the total specific heat capacity under the sub-critical temperature condition is always greater than that under the super-critical condition for the same adsorption loading. As the temperature increases, the specific heat of the system gradually increases, but the effect of temperature on the specific heat under super-critical conditions is not significant. When the temperature changes between 80-140 °C, the specific heat of the system only increases by about 0.1 $kJ \cdot kg^{-1} \cdot K^{-1}$, which is confirmed by Figure 3.4 and Figure 3.5.

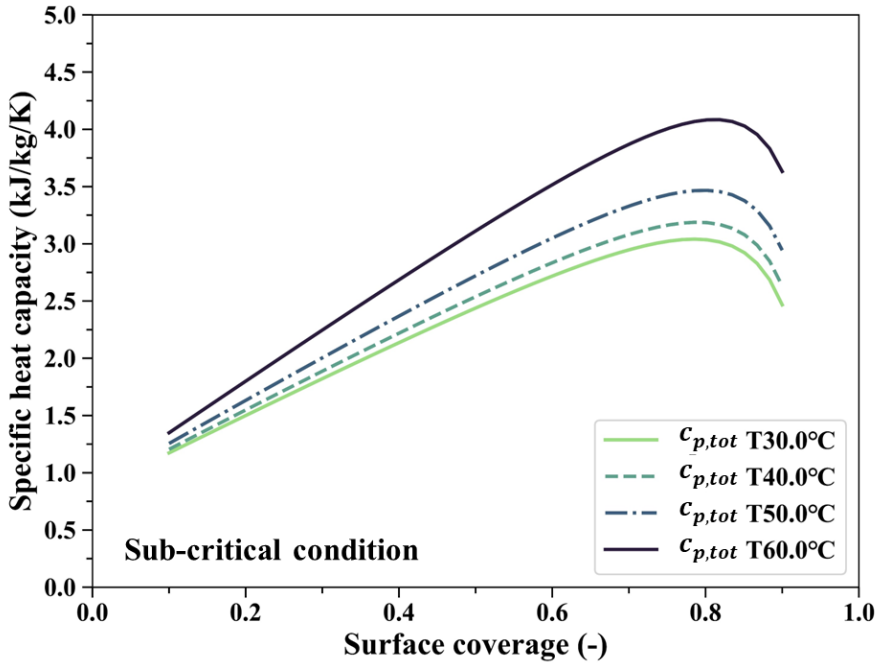

(a) Total specific heat capacity variation at sub-critical conditions

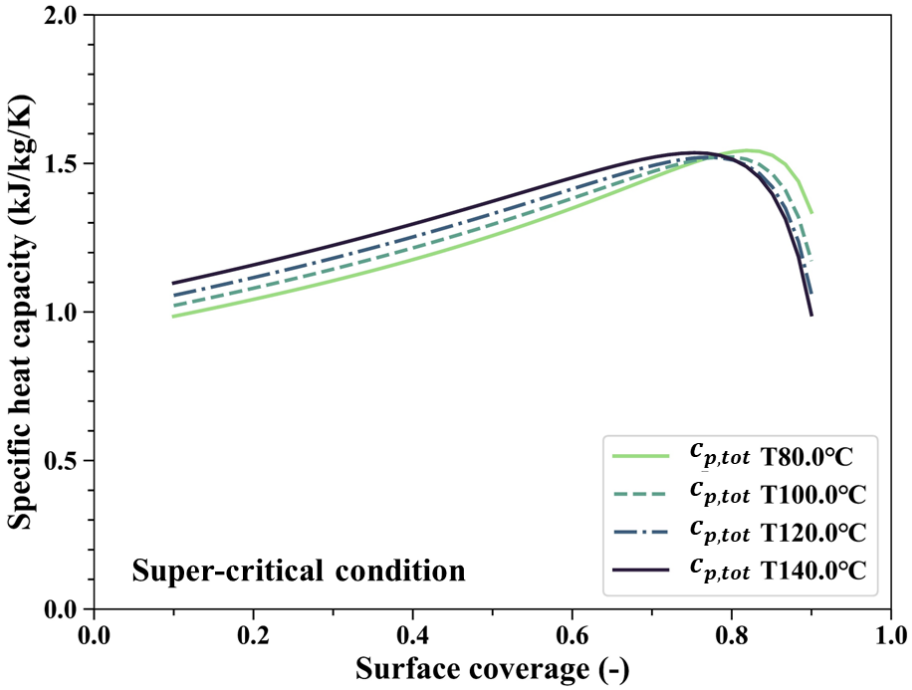

(b) Total specific heat capacity variation at super-critical conditions

Figure 3.7 Total specific heat capacity of the MSC30-R32 working pair variation with respect to surface coverage and temperature at both sub-critical and super-critical conditions

As evidenced by Figure 4.6, the impact of adsorption loading on the total specific heat capacity of the MSC30-R32 working pair cannot be ignored. Unlike the specific heat of gaseous or liquid refrigerants, which is only affected by temperature and pressure, the specific heat capacity of the adsorbed refrigerant depends on temperature, pressure, and adsorption loading. Consequently, substituting the specific heat of the adsorbed refrigerant with that of the gaseous or liquid refrigerant may lead to errors and is not advisable.

Table 3.2 specific heat capacity calculation parameters of different adsorbent-adsorbate working pairs

Adsorbent	MSC30	MSC30	MSC30	Chemviron AC	MSC30
Adsorbate	R32	R410a[14]	CO2	Ethane	Methane
T_{crit} (°C)	78.11	71.34	30.98	32.17	-82.59
mm (g·mol^{-1})	52.02	72.59	44.01	30.07	16.04
c_0 (cm^3·g^{-1})	1.75	5.96	1.59	0.64	1.13
E (J·mol^{-1})	5195.10	4326.09	5486.98	7339.15	5399.10
n (-)	1.37	1.17	1.32	1.21	1.35
k (-)	3.40	-	4.95	2.45	2.00
θ_{max} (-)	0.82	0.73	0.85	0.89	-

Figure 3.8 compares the specific heat capacity values of different adsorbate-adsorbent working pairs at sub-critical and super-critical conditions. For temperatures below the critical temperature, the values are evaluated at the maximum surface coverage θ_{max} corresponding to the typical operating conditions of an adsorption heat pump cycle (an adsorption temperature of 30 °C and an evaporation temperature of 7 °C), and at a fixed pressure of 3000 kPa for super-critical conditions. The calculation

parameters for different working pairs are summarized in Table 3.2.

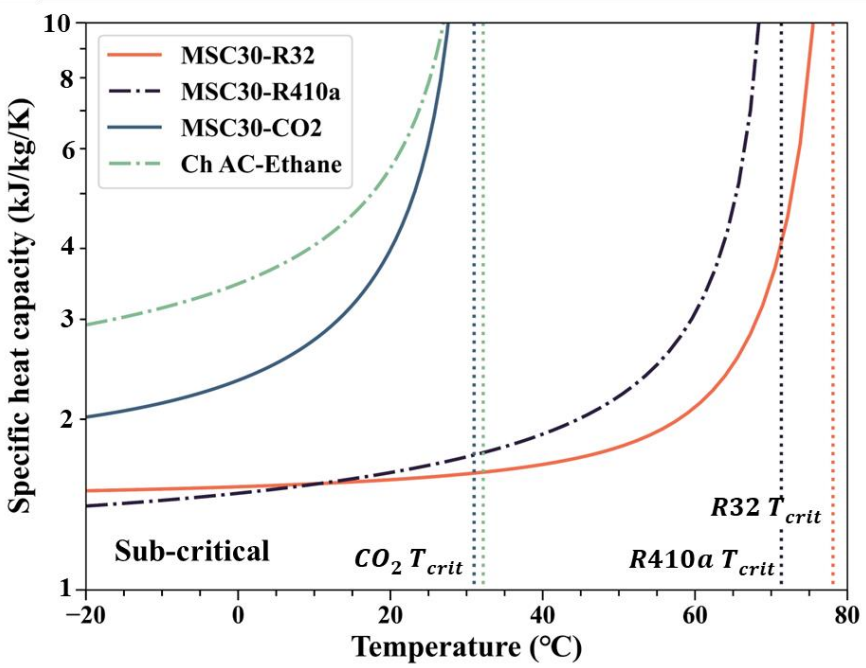

(a) Comparison of specific heat capacity values at sub-critical conditions

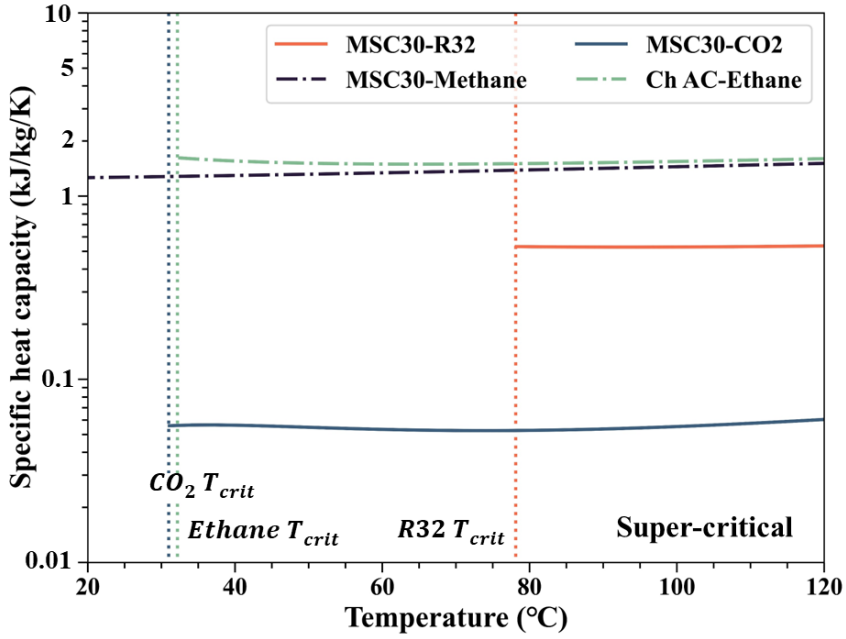

(b) Comparison of specific heat capacity values at super-critical conditions

Figure 3.8 Comparison of specific heat capacity values evaluated for different types of working pairs at both sub-critical and super-critical conditions

Figure 3.8 (a) depicts that, under subcritical temperature conditions, as the temperature approaches the critical temperature of the adsorbate, the specific heat capacity of the adsorbed phase increases rapidly. This is mainly due to the influence of the saturated liquid specific heat capacity on the adsorbed phase specific heat capacity. The $c_{p,aded}$ value of R32 and R410a is lower than that of the two natural working pairs (CO_2 and Ethane). At most temperatures, the adsorbed phase of the MSC30-R32 working pair displays the lowest specific heat capacity. The lower c_p value indicates that less heat is required to increase or decrease the system temperature in actual heat pump cycles. This outcome suggests that the system based on the MSC30-R32 working pair exhibits the lowest energy waste compared to systems based on other working pairs. Figure 3.8 (b) illustrates that under supercritical conditions, as temperature increases, the specific heat capacity of the adsorbed phase for each working pair increases slowly. The MSC30-CO_2 and MSC30-R32 pairs exhibit lower specific heat capacity values, while the Chemviron AC-Ethane and MSC30-Methane pairs show similar values for the adsorbed phase specific heat capacity.

The MSC30-R32 working pair used in this study is compared with the SAC2-R32 working pair studied by Sultan et al.[15]. The latter employed a newly developed adsorbent, SAC2, which is a phenol resin-based material treated with KOH. The specific heat capacity of the adsorbed phase of the adsorbent was computed using different thermophysical parameters and was evaluated when adsorbing R32 vapor. The adsorption parameters and the evaluation results of these calculations are presented in Table 3.3 and Figure 3.9, respectively. It is evident that the SAC2-R32 working pair can achieve a maximum relative adsorption capacity of only 0.63 under typical adsorption heat pump operating conditions. Hence, under subcritical temperature conditions, the specific heat capacity of the adsorbed phase is close to the saturated liquid specific heat

capacity of R32. Notably, the specific heat capacity of the adsorbed phase of the MSC30-R32 working pair is consistently lower than that of the SAC2-R32 working pair, irrespective of whether the operating conditions are super-critical or sub-critical, indicating lower energy waste.

Table 3.3 Thermophysical properties of adsorbents and adsorption parameters

Properties	MSC30	SAC2
Total surface area ($m^2 \cdot g^{-1}$)	3045	2992
Average pore width (nm)	1.11	1.62
Pore volume ($cm^3 \cdot g^{-1}$)	1.70	2.52
c0 ($cm^3 \cdot g^{-1}$)	1.75	3.13
E ($J \cdot mol^{-1}$)	5195.10	3498.10
n (-)	1.37	1.02
k (-)	3.40	3.65
θ_{max} (-)	0.82	0.63

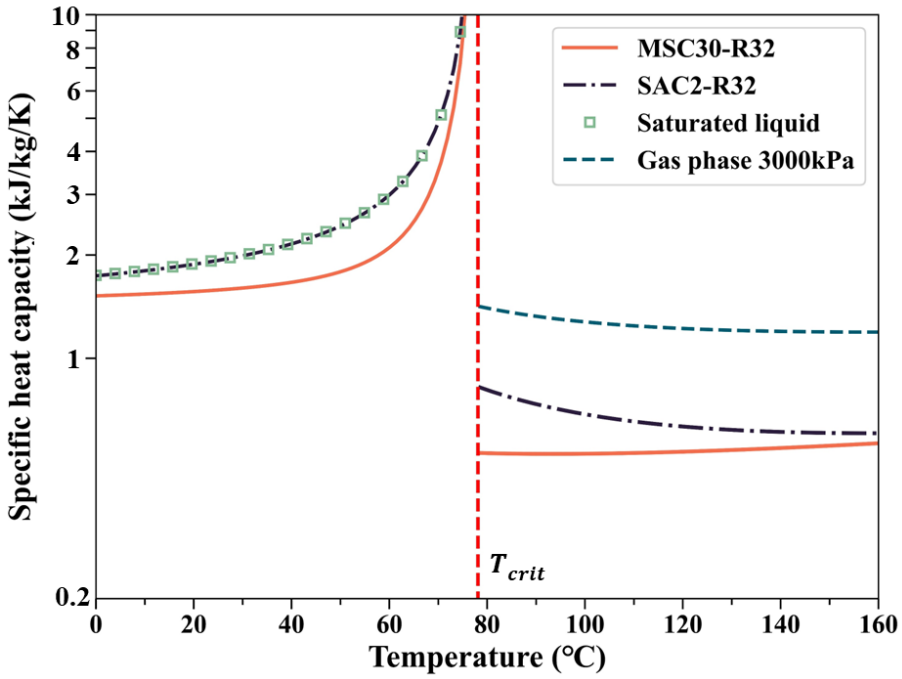

Figure 3.9 Comparison of specific heat capacity values R32 adsorption onto different adsorbents at both sub-critical and super-critical conditions

3.3.3 Adsorbed Phase Entropy

Entropy is an essential thermophysical parameter that characterizes the adsorbent-refrigerant interactions and is fundamental to understanding and analyzing adsorption based cooling or heating systems. As a physical quantity based on the adsorption isotherm and specific heat capacity, entropy is a function of temperature, pressure, and adsorption amount, and can be calculated using Eqs (3.27)-(3.30). Since entropy is a path-independent quantity, the triple point of the R32 refrigerant was selected as the reference point in this work, and the entropy at this point is considered to be zero.

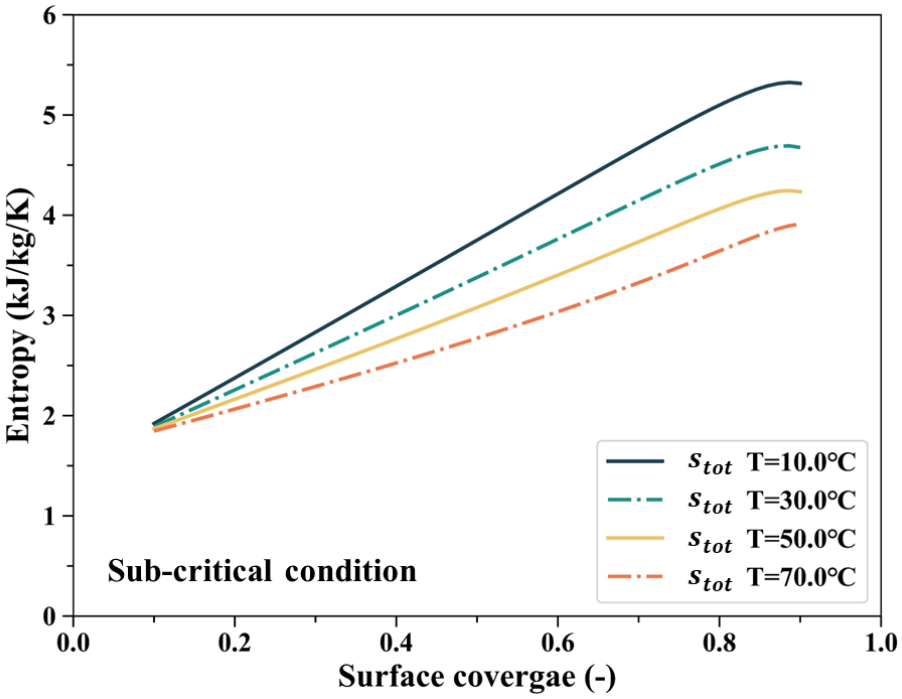

(a) Total entropy variation at sub-critical conditions

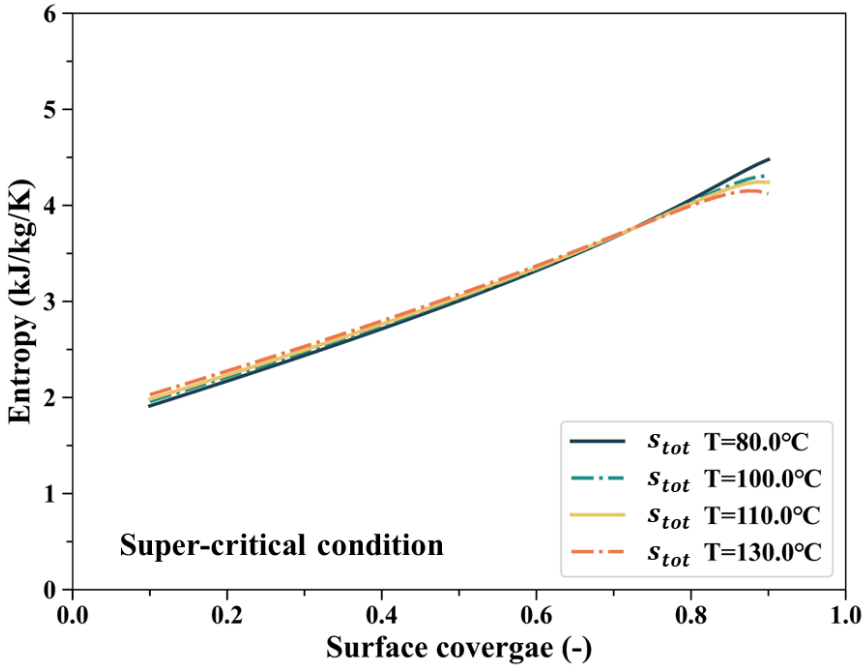

(b) Total entropy variation at super-critical conditions

Figure 3.10 Total entropy of the MSC30-R32 working pair variation with respect to surface coverage and temperature at both sub-critical and super-critical conditions

Figure 3.10 and Figure 3.11 illustrate the dependence of the total entropy of the MSC30-R32 working pair on the surface coverage (relative adsorption loading) under sub-critical and super-critical conditions. It is observed that the entropy is a monotonically increasing function of the surface coverage in both sub-critical and super-critical regimes. As the adsorption amount increases, the interaction between the refrigerant molecules and the adsorbent surface is enhanced, leading to an increase in the entropy. Under sub-critical conditions, the total entropy of the working pair gradually decreases with increasing temperature, and the differences between different temperatures increase with increasing surface coverage. However, under super-critical conditions, the variation in the total entropy at different temperatures is not significant. This is because, under supercritical conditions, the influence of temperature on the specific heat capacity is limited, and consequently, the impact on the entropy, which is based on specific heat, is relatively small.

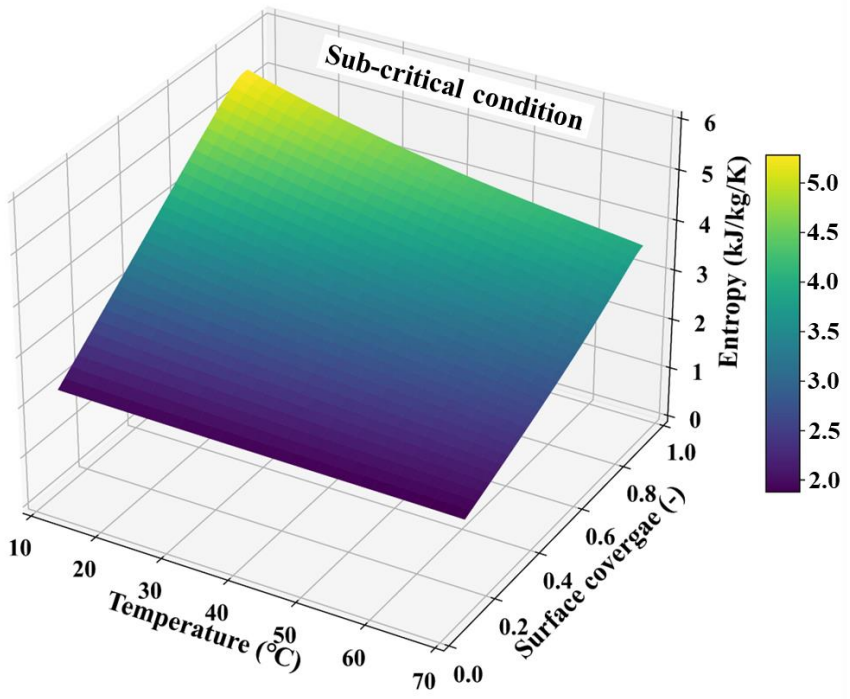

(a) Total entropy variation at sub-critical conditions

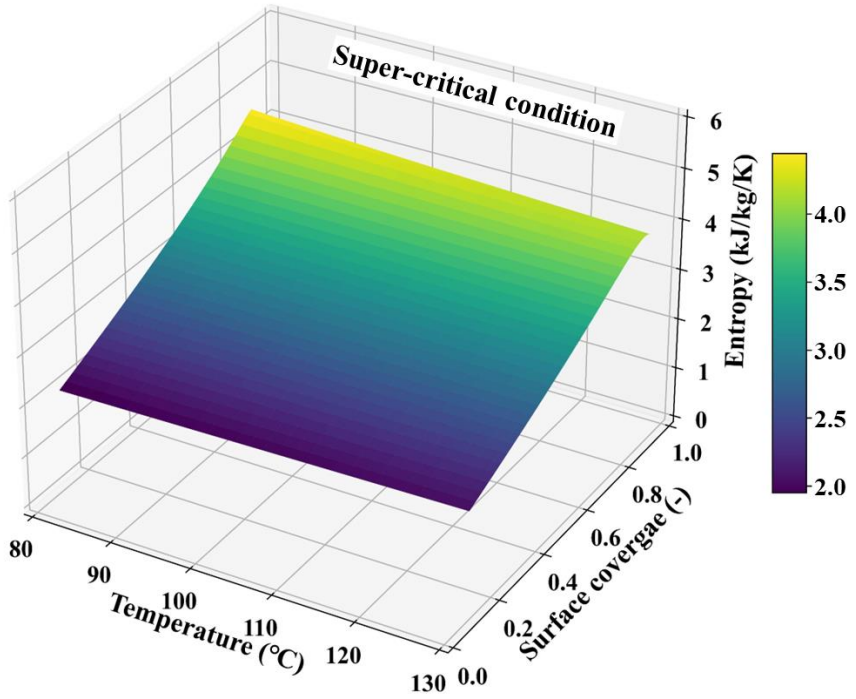

(b) Total entropy variation at super-critical conditions

Figure 3.11 Total entropy of the MSC30-R32 working pair under different surface coverage and temperature

3.3.4 Adsorbed Phase Enthalpy

Enthalpy is another fundamental thermodynamic parameter for understanding and analyzing adsorption systems. The enthalpy of the adsorbed phase and the total enthalpy of the working pair are calculated using Eqs (3.32)-(3.35). Enthalpy is also a path-independent physical quantity, and the triple point of R32 is chosen as the reference point, with the enthalpy assumed to be zero at this point.

The relationship between the enthalpy of the adsorbed phase and the surface coverage in the MSC30-R32 working pair system is shown in Figure 3.12. As more refrigerant molecules are captured by the adsorbent, the enthalpy of the adsorbed phase gradually increases both below and above the critical condition. This is due to the fact

that, as adsorption proceeds, gaseous refrigerant molecules convert to the adsorbed phase, and a portion of the energy released during this process is acquired by the adsorbed phase, resulting in the gradual increase of its enthalpy. Furthermore, as the temperature increases, the enthalpy of the adsorbed phase also increases. Moreover, it is notable that the impact of temperature on the enthalpy of the adsorbed phase is more significant below the critical condition than above it.

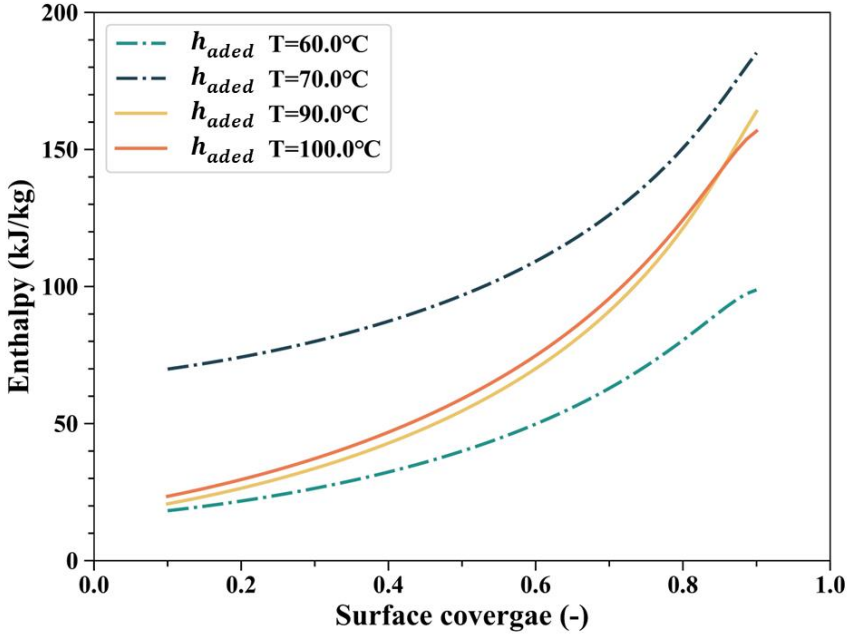

Figure 3.12 enthalpy of adsorbed phase variation with respect to surface coverage and temperature at both sub-critical and super-critical conditions

Figure 3.13 and Figure 3.14 depict the variation of the total enthalpy of the MSC30-R32 system with surface coverage. Comparing with Figure 3.12, it can be observed that the change in total enthalpy exhibits a similar trend to that of the adsorbed enthalpy. As the adsorption amount increases, the total enthalpy gradually rises at a faster rate due to the energy released from the conversion of gas-phase refrigerant molecules to adsorbed phase is transferred to the MSC30-R32 system. The total enthalpy under supercritical conditions is higher than that under subcritical conditions,

mainly due to the increase in the enthalpy of the adsorbent caused by the rise in temperature.

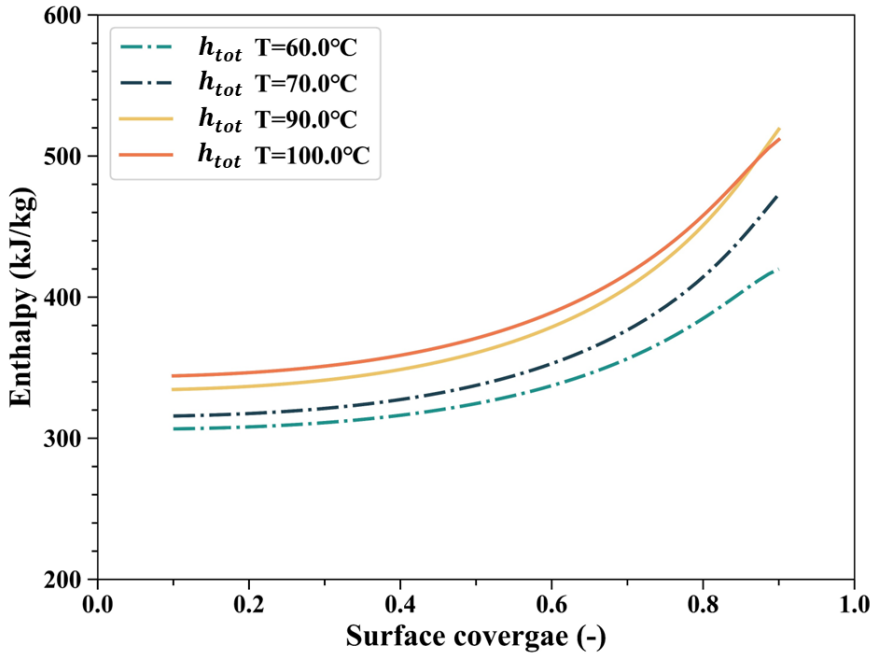

Figure 3.13 Total enthalpy of the MSC30-R32 working pair variation with respect to surface coverage and temperature at both sub-critical and super-critical conditions

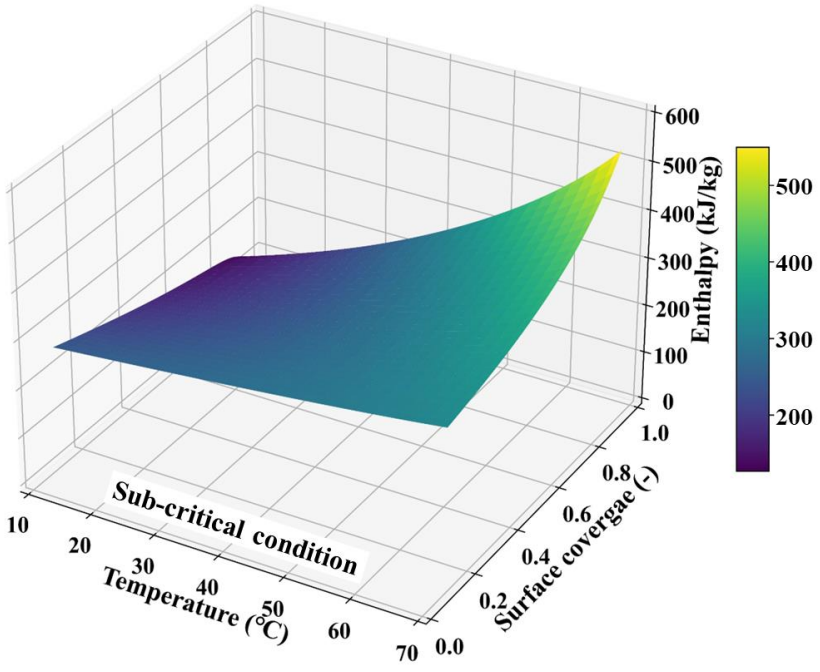

(a) Total enthalpy variation at sub-critical conditions

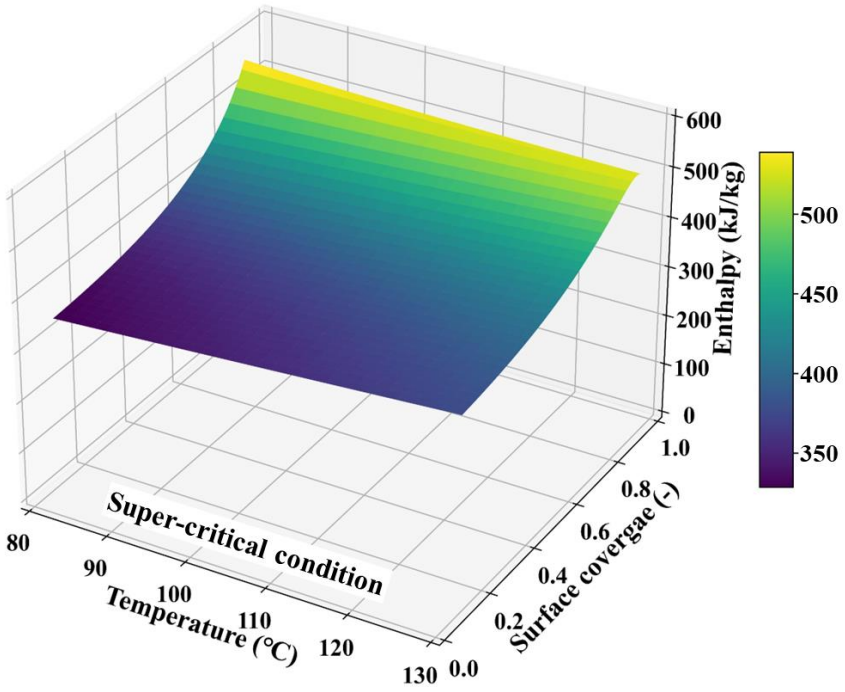

(b) Total enthalpy variation at super-critical conditions

Figure 3.14 Total enthalpy of the MSC30-R32 working pair under different surface coverage and temperature

3.4 Conclusions

A thorough understanding of the thermodynamic parameters of the adsorption working pairs, including isosteric heat of adsorption, specific heat capacity, entropy, and enthalpy, is a prerequisite for the research and design of adsorption systems. In this chapter, the theoretical framework for adsorption thermodynamic parameters is first introduced and derived, incorporating the micropore filling theory approach and considering volume correction of the adsorbed phase. The isosteric heat model proposed in this study was validated through experimental data for four working pairs: MSC30-R32, MSC30-Methane, MSC30-CO2, and Chemviron AC-Ethane. The results show

good consistency between the proposed model and the existing conventional model.

Furthermore, based on the experimental data of the MSC30-R32 working pair's adsorption uptake, this chapter calculates and analyzes the specific heat capacity, entropy, and enthalpy thermodynamic properties of the adsorbed phase of the MSC30-R32 working pair within the temperature range of 0-160 °C. The effects of temperature, pressure, and adsorption capacity on the thermodynamic properties of the working pair under subcritical and supercritical conditions are fully evaluated. The results show that at temperatures below the critical point, it is acceptable to use the specific heat capacity of the adsorbate's saturated liquid phase instead of the adsorbed phase's specific heat capacity when the relative adsorption loading is less than 0.6. However, if the specific heat capacity of the saturated liquid is still used to replace the specific heat capacity of the adsorbed phase at higher adsorption uptake, it will overestimate the value of the specific heat capacity. Under supercritical conditions, the difference between the specific heat capacity of the gaseous refrigerant and the adsorbed phase specific heat capacity cannot be ignored. Moreover, the specific heat capacity of the MSC30-R32 working pair is compared with that of other working pairs such as methane, ethane, and CO_2. Compared to these working pairs, the specific heat capacity of the adsorbed phase of the MSC30-R32 working pair is significantly lower, indicating less energy waste during heating or cooling.

Additionally, the effect of temperature and adsorption amount on the entropy and enthalpy of the adsorbate was evaluated. Regardless of whether under super-critical or sub-critical conditions, an increasing trend was observed in the entropy and enthalpy of the adsorbate with increasing surface coverage. When the temperature varied between 10-70 °C and the surface coverage varied between 0.1-0.9, the entropy and enthalpy ranged between 1.88-5.28 $kJ \cdot kg^{-1} \cdot K^{-1}$ and 126.40-550.08 $kJ \cdot kg^{-1}$, respectively. When

the temperature varied between 80-130 °C and the surface coverage varied between 0.1-0.9, the entropy and enthalpy ranged between 1.95-4.45 $kJ \cdot kg^{-1} \cdot K^{-1}$ and 328.47-538.99 $kJ \cdot kg^{-1}$, respectively.

A thorough understanding of the thermodynamic behavior of these systems is critical for the design and optimization of adsorption-based systems. The knowledge obtained from this research can be utilized to develop more accurate models and simulations for predicting the performance of adsorption systems, thereby facilitating the development of more efficient and effective adsorption-based processes for various applications such as heat pumps, and refrigeration.

3.5 Nomenclature

a_0-a_4	Coefficients for the specific heat capacity (-)
A	Adsorption potential ($J \cdot mol^{-1}$)
b_w	van der Waals volume ($cm^3 \cdot mol^{-1}$)
c_0	Volume-based maximum uptake ($cm^3 \cdot g^{-1}$)
c_p	Specific heat capacity ($kJ \cdot kg^{-1} \cdot K^{-1}$)
E	Characteristic energy of adsorption ($J \cdot mol^{-1}$)
G	Gibbs free energy ($J \cdot mol^{-1}$)
h	Specific enthalpy ($kJ \cdot kg^{-1}$)
h_{fg}	Latent heat of evaporation ($kJ \cdot kg^{-1}$)
k	Index of the pseudo-saturation equation (-)
mm	Molar mass ($g \cdot mol^{-1}$)
n	Heterogeneity factor (-)
p	Pressure (kPa)
q_{st}	Isosteric heat of adsorption ($kJ \cdot kg^{-1}$)
R	Molar gas constant (8.314 $J \cdot mol^{-1} \cdot K^{-1}$)
s	Specific entropy ($kJ \cdot kg^{-1} \cdot K^{-1}$)
T	Temperature (K)
v	Specific volume ($m^3 \cdot kg^{-1}$)

w	Equilibrium uptake in mass ratio ($kg \cdot kg^{-1}$)
w_s	Mass-based maximum uptake ($kg \cdot kg^{-1}$)
Greek symbols	
α	Thermal expansion coefficient (K^{-1})
θ	Surface coverage (-)
ρ	density ($kg \cdot m^{-3}$)
Subscript	
0	Reference state
aded	Adsorbed phase
ads	Adsorbent/adsorption
crit	Critical
gas	Gas phase
sat	Saturation
satgas	Saturated liquid phase
satliq	Saturated gas phase
tot	Total
trip	Triple point

3.6 References

[1] A. Chakraborty, B.B. Saha, K.C. Ng, S. Koyama, K. Srinivasan. Theoretical Insight of Physical Adsorption for a Single-Component Adsorbent plus Adsorbate System: I. Thermodynamic Property Surfaces, J. *Langmuir*. 25(2009) 2204-2211, doi: 10.1021/la803289p.

[2] I. Jahan, T.H. Rupam, M.L. Palash, K.A. Rocky, B.B. Saha. Energy efficient green synthesized MOF-801 for adsorption cooling applications, J. *Journal of Molecular Liquids*. 345(2022), doi: 10.1016/j.molliq.2021.117760.

[3] F.H.M. Azahar, S. Mitra, A. Yabushita, A. Harata, B.B. Saha, K. Thu. Improved model for the isosteric heat of adsorption and impacts on the performance of heat pump cycles, J. *Applied Thermal Engineering*. 143(2018) 688-700, doi: 10.1016/j.applthermaleng.2018.07.131.

[4] M. Sultan, T. Miyazaki, S. Koyama, Z.M. Khan. Performance evaluation of hydrophilic organic polymer sorbents for desiccant air-conditioning applications, J.

Adsorption Science & Technology. 36(2017) 311-326, doi: 10.1177/0263617417692338.

[5] A. Chakraborty, B.B. Saha, K.C. Ng, S. Koyama, K. Srinivasan. Theoretical insight of physical adsorption for a single component adsorbent+adsorbate system: II. The Henry region, J. *Langmuir*. 25(2009) 7359-7367, doi: 10.1021/la900217t.

[6] K.A. Rocky, M.A. Islam, A. Pal, S. Ghosh, K. Thu, Nasruddin, B.B. Saha. Experimental investigation of the specific heat capacity of parent materials and composite adsorbents for adsorption heat pumps, J. *Applied Thermal Engineering*. 164(2020), doi: 10.1016/j.applthermaleng.2019.114431.

[7] S.M. Sami, C. Tribes. An improved model for predicting the dynamic behaviour of adsorption systems, J. *Applied Thermal Engineering*. 16(1996) 149-161, doi: 10.1016/1359-4311(95)00054-h.

[8] H.T. Chua, K.C. Ng, A. Malek, T. Kashiwagi, A. Akisawa, B.B. Saha. Modeling the performance of two-bed, sillica gel-water adsorption chillers, J. *International Journal of Refrigeration*. 22(1999) 194-204, doi: 10.1016/s0140-7007(98)00063-2.

[9] K.A. Rahman, A. Chakraborty, B.B. Saha, K.C. Ng. On thermodynamics of methane plus carbonaceous materials adsorption, J. *International Journal of Heat and Mass Transfer*. 55(2012) 565-573, doi: 10.1016/j.ijheatmasstransfer.2011.10.056.

[10] H.T. Chua, K.C. Ng, N. Chakraborty, N.M. Oo. Thermodynamic property fields of an adsorbate-adsorbent system, J. *Langmuir*. 19(2003) 2254-2259, doi: 10.1021/la0267140.

[11] A. Pal, K.A. Rocky, B.B. Saha. Thermodynamic analysis of promising biomass-derived activated carbons/CO2 based adsorption cooling systems, J. *Journal of Co2 Utilization*. 46(2021), doi: ARTN 101457 10.1016/j.jcou.2021.101457.

[12] S. Seo, H. Kawakami, F. Miksik, N. Takata, K. Thu, T. Miyazaki. Thermodynamic analysis and impact of thermal masses on adsorption cycles using MaxsorbIII/R245fa and SAC-2/R245fa pairs, J. *International Journal of Refrigeration*. 123(2021) 52-62, doi: 10.1016/j.ijrefrig.2020.12.005.

[13] V.K. Singh, E.A. Kumar. Experimental investigation and thermodynamic analysis of CO 2 adsorption on activated carbons for cooling system, J. *Journal of CO2*

Utilization. 17(2017) 290-304, doi: 10.1016/j.jcou.2016.12.004.

[14] A.A. Askalany, B.B. Saha, I.M. Ismail. Adsorption isotherms and kinetics of HFC410A onto activated carbons, J. *Applied Thermal Engineering*. 72(2014) 237-243, doi: 10.1016/j.applthermaleng.2014.04.075.

[15] M. Sultan, T. Miyazaki, B.B. Saha, S. Koyama, H.S. Kil, K. Nakabayashi, J. Miyawaki, S.H. Yoon. Adsorption of Difluoromethane (HFC-32) onto phenol resin based adsorbent: Theory and experiments, J. *International Journal of Heat and Mass Transfer*. 127(2018) 348-356, doi: 10.1016/j.ijheatmasstransfer.2018.07.097.

Chapter 4
Adsorption Kinetics of Activated Carbon-R32 Systems

4.1 Introduction

The diffusion of adsorbate molecules into the pores of the adsorbent is governed by adsorption kinetics. The dynamic uptake of adsorbate by porous adsorbents plays a critical role in determining the performance of adsorption-based cooling systems. The adsorption kinetics represents the rate of adsorption, and a high-quality adsorbent must offer both high adsorption capacity and rapid kinetics in order to achieve efficient adsorption. A critical factor influencing the performance of an adsorption heat pump system is the kinetics of the working pair. Increasing the adsorption kinetics can lead to a reduction in the cycle time of the system, thereby enhancing its cooling or heating capacity per unit time. Therefore, to design an adsorption heat pump system that can operate under variable working conditions, it is imperative to comprehend the kinetics models and parameters of the adsorbent-refrigerant working pair.

Extensive research has been conducted to investigate the kinetics of various adsorbent-refrigerant pairs, and numerous adsorption kinetic models have been formulated., including the Langmuir model[1], Linear driving force (LDF) model[2], Fickian diffusion (FD) model[3] and pseudo-first order reaction model[4] et al.. Arisov et al.[5] investigated the adsorption kinetics of water vapor on loosely packed silica

gel particles within the temperature range of 29-64 °C and pressure range of 6.5-34 mbar. The results indicated that the effects of particle size, temperature, and pressure on the adsorption kinetics could be well described by the Fickian diffusion model. El-Sharkawy et al.[6] measured and compared the adsorption isotherms and kinetics of parent Maxsorb III-ethanol, KOH-H2 treated Maxsorb III-ethanol and H2 treated Maxsorb III pairs. It was found that the adsorption kinetics of ethanol on KOH-H2 treated Maxsorb III was faster than the other two studied adsorbents. Ghazy et al.[7] utilized the CVVP method to measure the adsorption kinetics of R404A on activated carbon coated with bitumen particles. They compared the fitting performance of the semi-infinite model, LDF model, and FD model with the experimental data, and the results indicated that both LDF and FD models showed a good fitting with the experimental data.

The adsorption of R32 on activated carbon spans from sub-critical to supercritical conditions while the attempts on the development and validation of adsorption kinetics for such conditions are rather limited. This chapter conducts an experimental analysis of the adsorption kinetics of R32 on the MSC30 adsorbent at different temperatures and pressures covering both sub- and supercritical conditions. A comparison was carried out among the widely used models, including the LDF model, FD model, and Semi-infinite model, for adsorption kinetics analysis. The diffusion time constants of MSC30-R32 working pairs have been calculated and contrasted with those of other pairs involving MSC30 and refrigerants. Additionally, a new mass transfer coefficient model has been proposed to enhance the precision and applicability range of the Jribi modified LDF model. The model was developed by introducing empirical parameters to modify Jribi's model, which were evaluated by regression of the transient adsorption uptake data. The proposed model was then validated using adsorbent-adsorbate pairs

at different temperatures to verify its reliability and effectiveness.

4.2 Experimental Section

The gravimetric method was employed to measure the temporal changes in R32 vapor adsorption uptake by MSC30, utilizing a magnetic suspension balance (Bel Japan, Inc. MSB-VG-S2). The experimental setup, as shown in Figure 2.1, was composed of magnetic suspension adsorption measurement unit, electromagnet, position sensor, evaporator, oil bath, air bath, pressure gauge, rotary pump and turbo-molecular pump. The sample mass was recorded using the magnetic suspension balance (MSB) with a repeatability of ±30μg and a relative error of ±0.002%. Water vapor pressure was measured using the pressure gauge type of Keller PAA-35XHTT-35, with an accuracy of 0.15-0.25% of full scale. Pressurized helium gas was utilized to ensure leak absence and calculate excluded volume for buoyancy correction.

The adsorption kinetics of the MSC30/R32 working pair were studied over a wide range of temperatures from 25 to 150 °C. Before conducting the measurements, the adsorbent sample was regenerated and degassed under a vacuum pressure of 3×10^{-4} Pa for 4 hours at 130 °C. Then, the experimental setup maintained the adsorbent and refrigerant temperatures at the target temperature, and the valve between the refrigerant and adsorbent was opened to initiate the adsorption process. The refrigerant temperature was raised to the next target temperature after the equilibrium state in the sample cell was achieved, indicating further adsorption. The adsorption kinetics were evaluated based on the instantaneous measurements of the adsorbent sample at each temperature set point.

While conducting the measurements, it's important to note that the automatic buoyancy correction is applied to reduce the impact of buoyancy on the experimental outcomes, however, it can also introduce additional uncertainties in the measurements[8]. The following equation is used to correct for absolute adsorption amount[9].

$$w_{abs} = w_{exc} + \rho_{ref} \cdot v_{pore} \tag{4.1}$$

Here, w_{abs} is absolute adsorption uptake ($kg \cdot kg^{-1}$), w_{exc} is the excess uptake ($kg \cdot kg^{-1}$), ρ_{ref} is the density of the refrigerant gas ($kg \cdot m^{-3}$), v_{pore} is the specific pore volume of the adsorbent ($m^3 \cdot kg^{-1}$).

4.3 Adsorption Kinetics Models

4.3.1 Commonly used adsorption kinetic models

4.3.1.1 Linear Driving Force Model

As one of the earliest proposed adsorption kinetics models, the Linear Driving Force (LDF) model has gained widespread acceptance and application in various adsorption systems because of its straightforward mathematical formulation[2, 10]. The model postulates that the adsorption rate is directly related to the difference between the transient adsorbed amount of the refrigerant at any given time $w(t)$ and its equilibrium concentration w_e. The adsorption rate equation is given in equation:

$$\frac{\partial w}{\partial t} = k_s a_v [w_e - w(t)] \tag{4.2}$$

Where w_e is the equilibrium uptake in the mass ratio ($kg \cdot kg^{-1}$). $w(t)$ is the

instantaneous adsorbed amount ($kg \cdot kg^{-1}$), $k_s a_v$ is the overall mass transfer coefficient (s^{-1}).

The LDF model has gained popularity among researchers who seek to fit experimental data related to adsorption kinetics due to its mathematical straightforwardness and its ability to provide a fundamental understanding of the adsorption process. This model considers the adsorption process as a time-dependent process that describes the adsorption from the initial stage to the point of reaching the equilibrium state, assuming a uniform temperature and neglecting the heat transfer rate of the adsorbent particles, as well as the effects of surface structural heterogeneity[11, 12].

The LDF equation is versatile in terms of its applicability to different coordinate systems[13].

$$\mathrm{k_s a_v} = \frac{\mathrm{F_0 D_s}}{\mathrm{R_p^2}} \tag{4.3}$$

Where F_0 is the shape factor (-). For the study of adsorbent particles or powders with uniform structures, F_0=15. Therefore, the LDF model expressed in a spherical coordinate system can be written as:

$$\frac{\partial w}{\partial t} = \frac{F_0 D_s}{R_p^2}[w_e - w(t)] \tag{4.4}$$

Here, D_s defines the diffusion coefficient ($m^2 \cdot s^{-1}$) which is usually assumed to be a constant, R_p is the adsorbent particle radius (m).

At $t = t_0$, $w = w_0$ and at $t = t$, $w = w$, by integrating the Eq.(4.4), the correlation of fractional uptake F and dimensionless time θ_t can be derived:

$$\int_{w_0}^{w} \frac{1}{w_e - w} dw = \int_{t_0}^{t} \frac{15 D_s}{R_p^2} dt \tag{4.5}$$

$$\ln\frac{w_e-w}{w_e-w_0} = -\frac{15D_s}{R_p^2}(t-t_0) \tag{4.6}$$

$$F = \frac{w-w_0}{w_e-w_0} = 1-\exp\left[-\frac{15D_s}{R_p^2}(t-t_0)\right] \tag{4.7}$$

Linearizing the above equation, one obtains:

$$ln(1-F) = -\frac{15D_s}{R_p^2}t = -15\theta_t \tag{4.8}$$

Where, F is the fractional uptake (-), given by $F = \frac{w-w_0}{w_e-w_0}$, θ_t is the dimensionless time (-), and written as $\theta_t = \frac{D_s}{R_p^2}t$.

A linear relationship can be observed by plotting $ln(1-F)$ against adsorption time t, with a slope of $-\frac{15D_s}{R_p^2}$ and passing through the origin.

4.3.1.2 Fickian Diffusion Model

Within the FD model, it is postulated that the rate of adsorption is proportional to the concentration gradient of the adsorbate in the porous material[14]. A steeper concentration gradient translates to a faster rate of adsorbate transport and surface adsorption. Meanwhile, heat transfer is assumed to be sufficiently rapid, such that any temperature gradients throughout the particle and the encompassing fluid are negligible[15, 16]. Under these assumptions, the diffusion equation by a spherical adsorbent material can be derived as:

$$\frac{\partial w}{\partial t} = \frac{1}{r^2}\left[\frac{\partial}{\partial r}\left(D_s r^2\frac{\partial w}{\partial r}\right)\right] \tag{4.9}$$

A solution to the above expression is commonly expressed in the following well-known form, given by:

$$F = 1-\frac{6}{\pi^2}\sum_{n=1}^{\infty}\frac{1}{n^2}exp\left(-15n^2\pi^2\frac{D_s}{R_p^2}t\right) \tag{4.10}$$

Here, n is the integer number. This equation exhibits rapid convergence as the adsorption approaches saturation, with higher-order terms being negligible[6], thereby enabling its re-expression in a simplified form:

$$F = 1 - \frac{6}{\pi^2} exp\left(-\pi^2 \frac{D_S}{R_p^2} t\right) \tag{4.11}$$

$$ln(1 - F) = ln\frac{6}{\pi^2} - \pi^2 \frac{D_S}{R^2} t \tag{4.12}$$

A linear relationship between $ln(1 - F)$ and t can be observed from the plot, with a slope of $-\pi^2 \frac{D_S}{R^2}$ and an intercept of $ln\frac{6}{\pi^2}$.

4.3.1.3 Semi-Infinite Model

During the early stages of diffusion, the transport mechanism can be approximated as occurring within a semi-infinite medium[16, 17]. Consequently, at short time region, the uptake curve for any particle shape can be simplified to:

$$F \approx \frac{2A}{V}\left(\frac{D_S}{\pi} t\right)^{1/2} \tag{4.13}$$

Here, A is the surface area (m^2) and V represent the volume (m^3) of the adsorbent granule. For spherical adsorbent particles, the above equation can be rewritten as:

$$F = 6\left(\frac{D_S}{\pi R_p^2} t\right)^{1/2} \tag{4.14}$$

By plotting the fractional uptake F versus the square root of time $\sqrt{t}$, a straight line with a slope of $6\sqrt{\frac{D_S}{\pi R_p^2}}$ and an intercept of zero is expected.

It is worth highlighting that the assumption of semi-infinite flat plates is valid only during the initial stage of diffusion. Hence, typically, the Semi-Infinite model demonstrates high accuracy only during the early adsorption period[16].

4.3.1.4 Arrhenius plot

One can utilize the classical Arrhenius equation to establish a correlation between the activation energy, adsorption temperature, and the surface diffusion coefficient, which is a critical factor in predicting the overall mass transfer coefficient.

$$D_s = D_{s0} \exp\left(\frac{-E_a}{RT}\right) \tag{4.15}$$

Here, D_{s0} is the pre-exponential constant ($m^2 \cdot s^{-1}$), E_a is the activation energy ($kJ \cdot kg^{-1}$). Linearizing the above equation, the following can be obtained:

$$\ln D_s - \ln D_{s0} = \left(\frac{-E_a}{RT}\right) \tag{4.16}$$

Or:

$$\ln\left(\frac{D_s}{R_p^2}\right) = \ln\left(\frac{D_{s0}}{R_p^2}\right) - \left(\frac{E_a}{R}\right)\left(\frac{1}{T}\right) \tag{4.17}$$

A plot of $\ln\left(\frac{D_s}{R_p^2}\right)$ against $1/T$ can generate a straight line with a slope of $-\left(\frac{E_a}{R}\right)$ and intercept of $\ln\left(\frac{D_{s0}}{R_p^2}\right)$, which is known as the Arrhenius plot.

4.3.2 Modified adsorption kinetic model

4.3.2.1 Sultan's model

A modification to the LDF model was introduced by Sultan et al[18] through the incorporation of a fitting parameter, denoted as m. This modification involves raising the θ_t to the power of m. The Sultan model is represented by the following equation[14]:

$$\frac{\partial w}{\partial t} = \frac{15m}{t}\theta_t^m[w_e - w(t)] \tag{4.18}$$

Here, θ_t is the dimensionless time given by,

$$\theta_t = \frac{D_s t}{R^2} \tag{4.19}$$

The Sultan model is equivalent to the original LDF model when m equals 1.

To determine the transient adsorption uptake, the Eq. (4.18) was integrated within certain limits of $t = 0,\ w = w_0$ and $t = t,\ w = w$, resulting in:

$$\int_{w_0}^{w} \frac{1}{w_e - w} d\,w = 15m\left(\frac{D_s}{R_p^2}\right)^m \int_0^t t^{m-1}\,dt \tag{4.20}$$

$$\ln\frac{w_e - w}{w_e - w_0} = -15\left(\frac{\mathrm{D_s}}{\mathrm{R_p^2}}\right)^{\mathrm{m}} \mathrm{t^m} = -15\theta_t^m \tag{4.21}$$

$$F = 1 - \exp\left[-15\left(\frac{D_s}{R_p^2}t\right)^m\right] \tag{4.22}$$

$$ln(1 - F) = -15\left(\frac{D_s}{R_p^2}t\right)^m \tag{4.23}$$

By plotting $ln(1 - F)$ against t^m a linear relationship can be observed with a slope of $-15\left(\frac{D_s}{R_p^2}\right)^m$ and passing through the origin. The instantaneous uptake w can be obtained by:

$$w = \exp\left[-15\left(\frac{D_s}{R_p^2}t\right)^m\right](w_e - w_0) + w_0 \tag{4.24}$$

4.3.2.2 Jribi's model

Sultan model introduces a new fitting parameter, which increases the degrees of freedom of the model, and is therefore expected to improve the model's fitting performance. In contrast, the modified LDF model suggested by Jribi et al[19]

proposes the use of the modified mass transfer coefficient $k_{m.LDF}$, whose value being dependent on both the instantaneous and equilibrium adsorption uptake, as a replacement for $k_s a_v$.

$$k_{m.LDF} = k_2^{\frac{w}{w_e}} \tag{4.25}$$

The mass transfer coefficient k_2 is given by:

$$k_2 = \exp\left(\frac{w_e}{w(t)} \ln\left(\frac{w(t+\triangle t)-w(t)}{\triangle t(w_e-w(t))}\right)\right) \tag{4.26}$$

Jribi et al.[19] conducted experimental research to examine the adsorption kinetics of CO_2 onto MSC30 and validated the accuracy of their new model. The Jribi model displayed favorable predictive capabilities for instantaneous adsorption uptake, particularly in the long-time region.

It should be noted that the Jribi model does not employ a diffusion coefficient D_s, but instead calculates the adsorption amount at the next time step based on the instantaneous adsorption amount from the previous time step. The Jribi model differs from other models that use the Arrhenius equation to calculate the diffusion coefficient at different temperatures. Instead, it employs the average value of the mass transfer coefficient parameter at different temperature and pressure conditions for analyzing adsorption kinetics. This approach may reduce the accuracy of the Jribi model and limit its range of applicability. If this model is used in conditions where there is no prior experimental data on dynamic adsorption, there may be deviations in the fit of the dynamic adsorption due to parameter bias. To ensure the reliability and predictive accuracy of dynamic adsorption models, it is crucial to accurately determine the mass transfer coefficients at different temperature ranges.

In this study, instead of using the average value of k_2 across all temperatures, a

new mass transfer coefficient model was proposed to calculate mass transfer coefficient at different temperatures as follows:

$$k_2 = k_0 exp(s_0 T) \tag{4.27}$$

$$\ln k_2 = \ln k_0 + s_0 T \tag{4.28}$$

Here, the parameters of k_0 and s_0 are evaluated through regression of the transient adsorption uptake data. A plot of $\ln k_2$ versus T should be linear with slope of s_0 and intercept of $\ln k_0$. With the proposed model, the mass transfer coefficient at any given temperature can be obtained by using the provided parameters and the proposed equation. By accurately determining these parameters, it is possible to achieve more precise and reliable predictions of dynamic adsorption behavior.

4.4 Results and Discussion

Adsorption kinetics of R32 vapor on the MSC30 adsorbent were experimentally measured at various temperatures including 25 °C, 30 °C, 50 °C, 70 °C, 90 °C, 110 °C, 130 °C, and 150 °C. The adsorption pressures were varied up to a maximum of 3000 kPa. Temporal histories of vapor pressures and adsorption uptake during the first 400 minutes at different adsorption temperatures are shown in Figure 4.1 (a) and (b). As depicted in the figure, the adsorption kinetics exhibit a consistent pattern across all adsorption steps. Immediately following an increase in pressure, the amount of adsorbed amount rises rapidly before gradually stabilizing around the equilibrium uptakes.

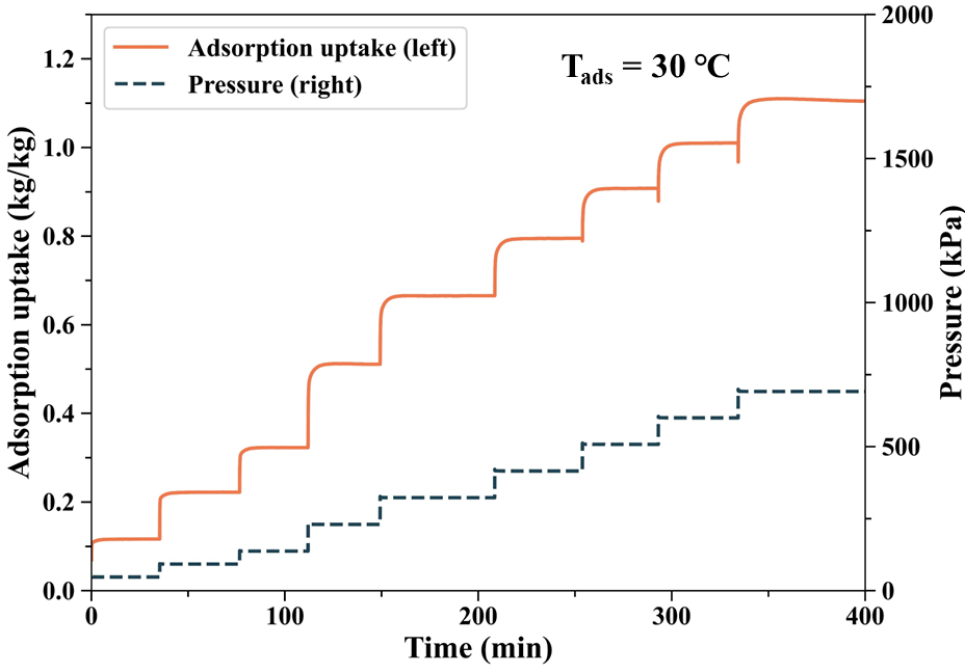

(a) Temporal histories of at adsorption temperature of 30°C

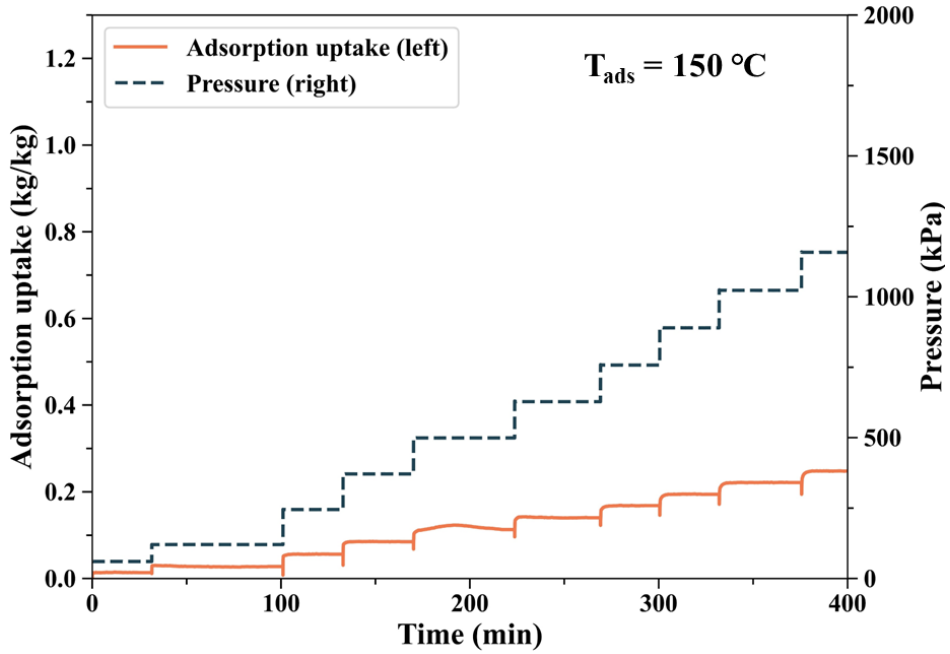

(b) Temporal histories of at adsorption temperature of 150°C

Figure 4.1 Temporal histories of adsorption uptake and pressure of MSC30-R32 pair at adsorption temperature of: (a) 30°C, (b) 150°C

4.4.1 Commonly used adsorption kinetic models

The experimental adsorption kinetics were first fitted using the three most commonly used adsorption kinetic models, LDF model, FD model and Semi-infinite model, as described in Section 4.3.1

As discussed in section 4.3.1.3, the applicability of the semi-infinite model depends on the plot of fractional uptake F against $\sqrt{t}$, which is presented in Figure 4.2

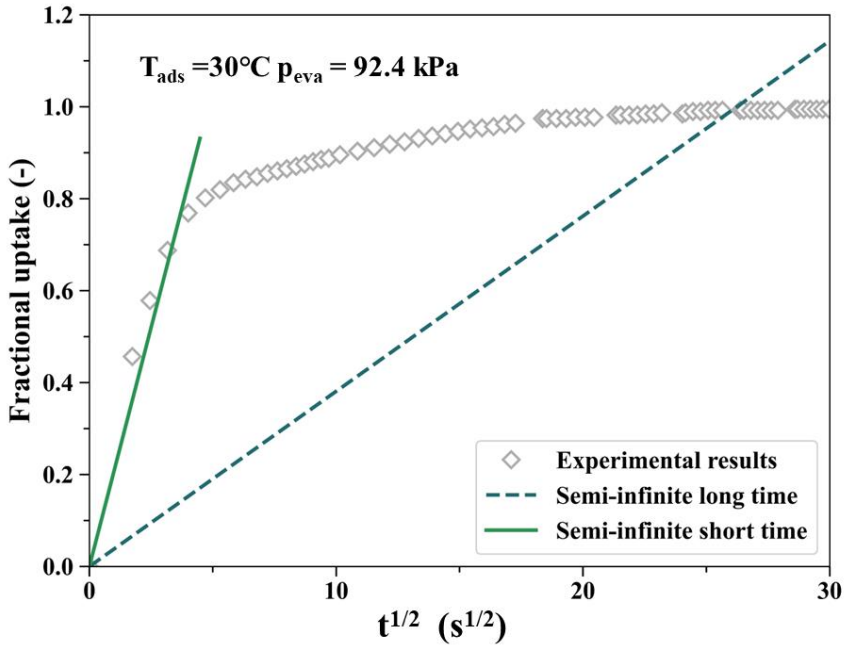

Figure 4.2 Plot of fractional uptake against $t^{1/2}$ for MSC30-R32 pair at adsorption temperature of 30°C and evaporation pressure of 92.4 kPa

Figure 4.2 demonstrates the adequacy of the semi-infinite model in describing the early stage of adsorption, but its predictive capability declines as the adsorption approaches saturation. During the early stages of adsorption, there is a rapid increase in the relative adsorption amount, which follows an almost linear trend. At this point, the semi-infinite model can be effectively aligned with the experimental data. As the

adsorption process approaches equilibrium, the rate of adsorption progressively declines until it reaches zero. However, owing to the linear nature of the semi-infinite model, it is unable to effectively capture this trend. Consequently, the projected outcomes of the semi-infinite equation exhibit substantial disparities from experimental results at long-time approximation.

The LDF and FD models are popularly utilized for investigating adsorption kinetics. A linear plot of $ln(1-F)$ against time allows for the determination of the diffusional time constant[20]. Figure 4.3 illustrates such a plot for the MSC30-R32 pair at evaporation pressures of 1056 kPa and adsorption temperature of 25 ℃. The plot showed that the FD model had better agreement with the experimental data compared to the LDF model. At the initiation of the adsorption process, the $ln(1-F)$ value exhibits a nonlinear characteristic, but as adsorption progresses, the $ln(1-F)$ value gradually displays a stable linear trend.

As depicted in Figure 4.3 and Figure 4.4, Both the LDF and FD models demonstrate satisfactory accuracy in predicting the adsorption uptake rates near the saturation state. However, the accuracy of the LDF and FD models in predicting adsorption uptake rates may be limited at or near the initial phase of adsorption. The linear form of the FD model exhibits a fixed intercept of $ln\frac{6}{\pi^2}$, whereas the LDF model has a fixed intercept of 0. Therefore, during the initial stages, the predicted outcomes of the FD model and LDF model may still exhibit some variation from the experimental results.

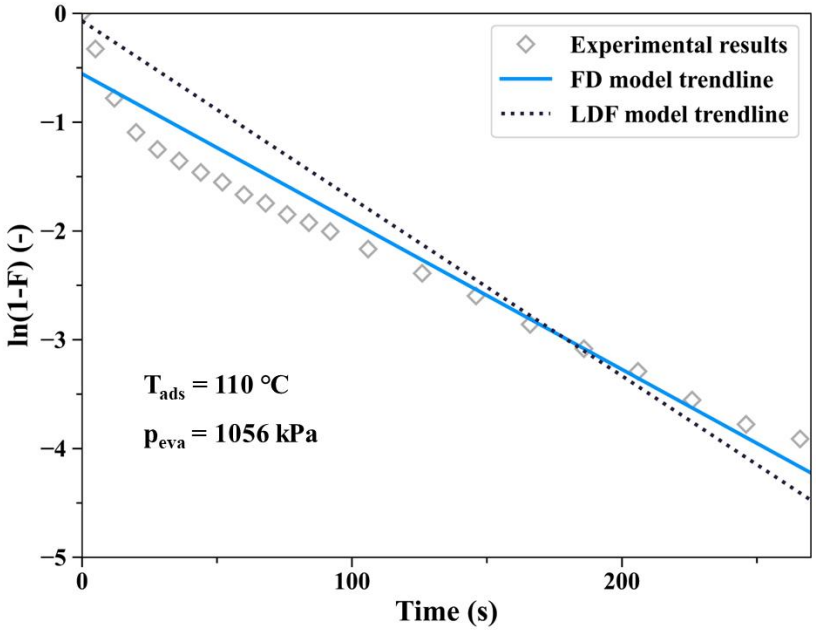

Figure 4.3 Plot of ln(1-F) versus time for MSC30-R32 pair at adsorption temperature of 25°C

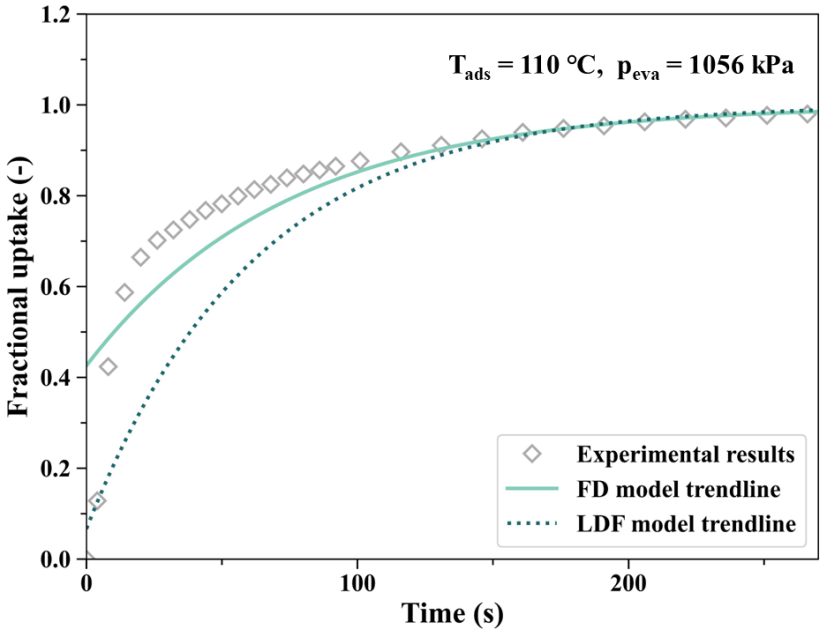

Figure 4.4 Fitting of LDF and FD models with experimental adsorption kinetics of MSC30-R32 pair at adsorption temperature of 110°C and evaporation pressure of 1056 kPa

As shown in Figure 4.1, multiple adsorption steps are observed at different adsorption temperatures. In this study, the values of corresponding diffusion time constant were computed for each adsorption step. The diffusion time constant at a given temperature was represented by utilizing the average value of $\frac{D_s}{R_p^2}$ across all adsorption steps. Figure 4.5 shows the plotted $\ln\left(\frac{D_s}{R_p^2}\right)$ against $1/T$, which results in a straight line. The slope of the plot signifies the magnitude of $-\left(\frac{E_a}{R}\right)$, while the point at which it intersects with the y-axis indicates the value of $\ln\left(\frac{D_{s0}}{R_p^2}\right)$. The values D_{s0} and E_a are furnished in Table 4.1. By utilizing the provided parameters and the Arrhenius equation, one can readily get the surface diffusion coefficient of the MSC30-R32 working pair at any given temperature. This facilitates a comprehensive understanding of the adsorption process of R32 vapor onto MSC30 and serves as a fundamental basis for the simulation and design of an adsorption heat pump system.

As a carbon-based adsorbent material with favorable thermal performance, MSC30 exhibits excellent adsorption properties for various refrigerants. Many researchers have studied the adsorption characteristics of MSC30 with different refrigerants. The adsorption kinetic characteristics of the MSC30-R32 working fluid pair utilized in this study were compared with those of five other refrigerants, including ethanol, R134a, R507a, R152a and R410a, as illustrated in Figure 4.5 and Table 4.1. It is evident that the diffusion time constant of different working pairs increases with the rise in adsorption temperature. This observation suggests that as the adsorption temperature increases, the adsorption rate is likely to be accelerated. Among the selected refrigerant pairs, the MSC30-R32 refrigerant pair exhibits the highest value of $\ln\left(\frac{D_{s0}}{R_p^2}\right)$, indicating that MSC30 has a higher adsorption rate for R32 compared to

the other refrigerants.

Table 4.1 Comparison of fitting parameters for different MSC30-Refrigerant pairs

Working pair	E_a (J/mol)	D_{s0}/R_p^2 (1/s)
MSC30-R32	6262.37	0.00853
MSC30-Ethanol[6]	10365.40	0.0161
MSC30-R134a[16]	9232.38	0.0111
MSC30-R507a[16]	11806.54	0.0264
MSC30-R152a[7]	1903.18	0.00016
MSC30-R410a[21]	1161.37	0.00010

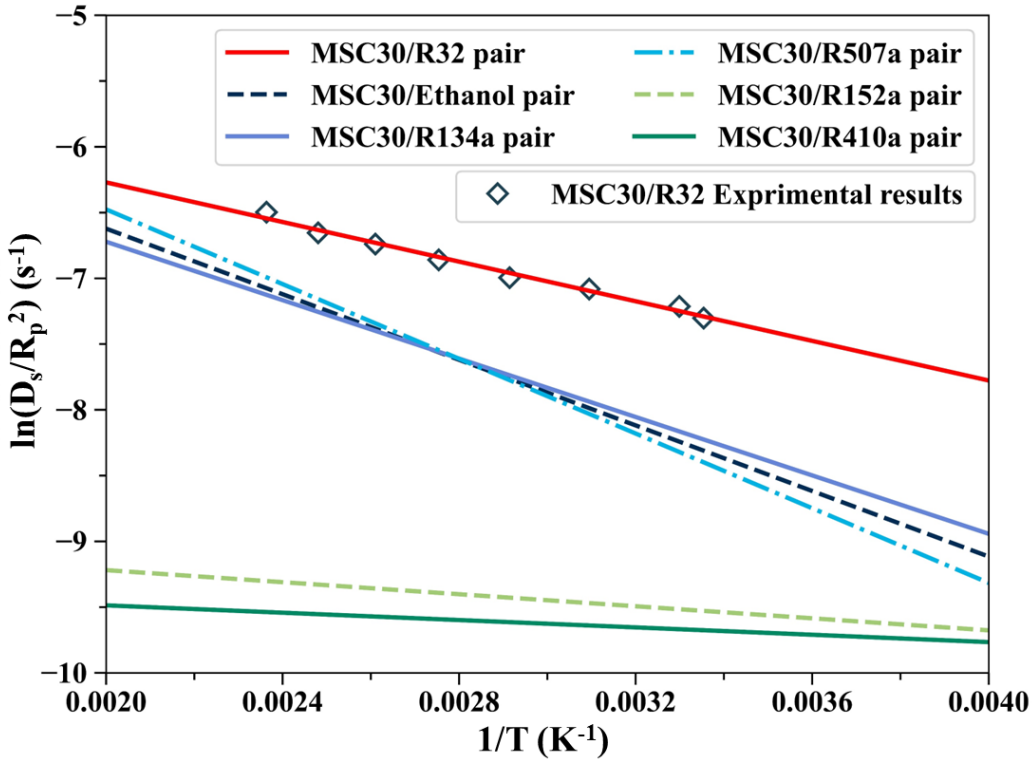

Figure 4.5 Comparison of Arrhenius plots for different MSC30-Refrigerant pairs

4.4.2 Modified adsorption kinetic models

As evidenced by the study above, neither the LDF nor FD models can accurately predict the adsorption kinetics of the MSC30-R32 working pair investigated in this study. To accurately predict the adsorption kinetics at diverse thermal and pressure regimes, the Sultan model and Jribi model were also used to fit the experimental data.

As detailed in section 4.3.2.1, the applicability of the Sultan model depends on the plot of fractional uptake $ln(1-F)$ against t^m, as shown in Figure 4.6. The computed outcomes of the Sultan model demonstrate a remarkable concurrence with the experimental results, so that fitting parameters can be estimated with a high degree of accuracy.

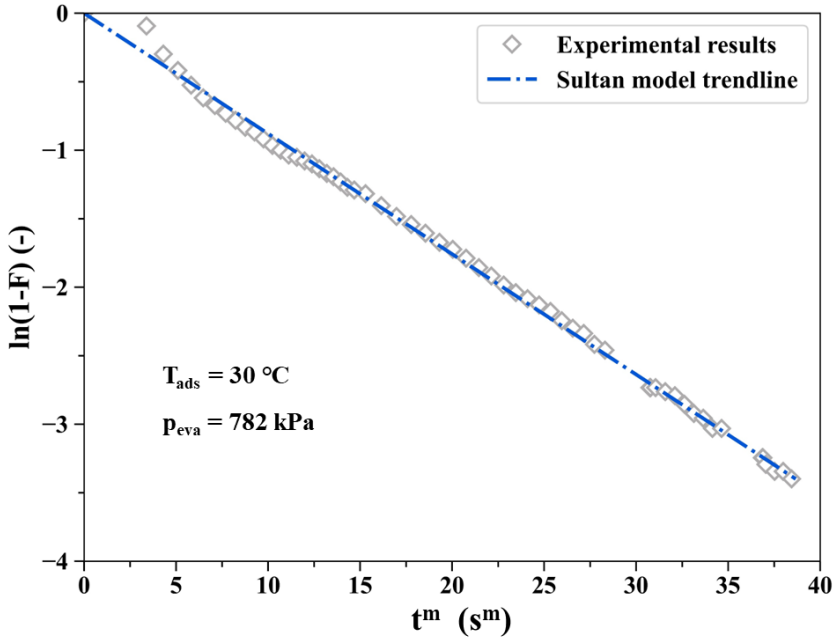

Figure 4.6 Plot of ln(1-F) against tm for MSC30-R32 pair at adsorption temperature of 30 °C and evaporation pressure of 782 kPa

The experimental fractional uptake of the MSC30-R32 pair and the estimated values obtained from the LDF model, FD model, and Sultan model are presented in

Figure 4.7 (a) and (b). The FD and LDF models demonstrate good agreement with experimental results during the long-time stages of adsorption. Nonetheless, notable inaccuracies persist during the initial stages of adsorption. In comparison to the LDF and FD models, the Sultan model provides the most optimal performance. As demonstrated in Figure 4.7 (b), the calculated values of the Sultan model demonstrate an exact match with the experimental results not only in the initial phase but also near the equilibrium phase. The inclusion of parameter m imparts greater degrees of freedom to the LDF model, thereby facilitating a more precise fit of the experimental data. However, in some operational conditions during the initial phase, there are still deviations between the Sultan model's calculations and experimental data, as illustrated in Figure 4.7 (a).

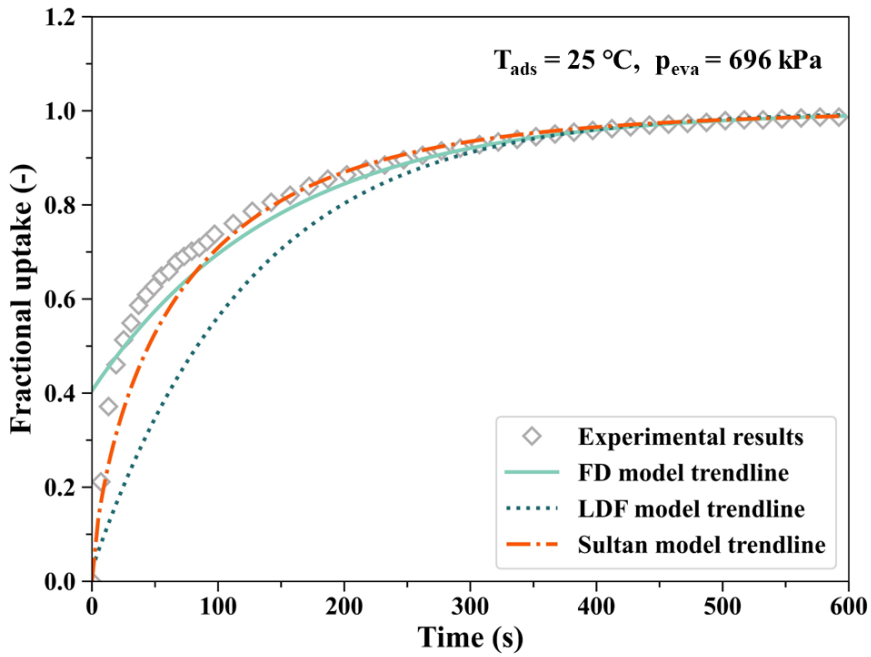

(a) Adsorption temperature of 25°C and evaporation pressure of 696 kPa

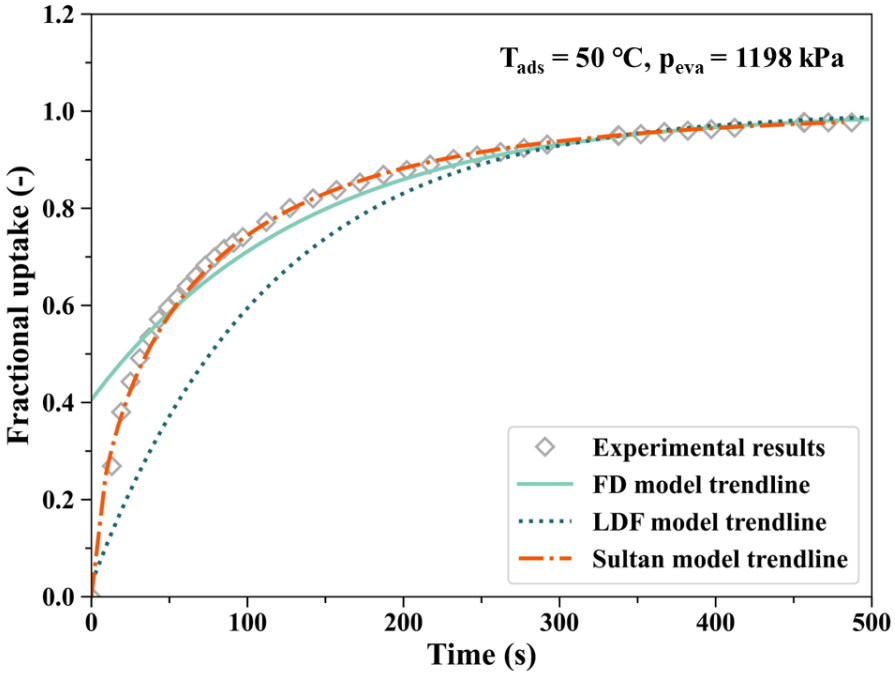

(b) Adsorption temperature of 50°C and evaporation pressure of 1198 kPa

Figure 4.7 Comparison of Sultan model estimation of fractional uptake with LDF and FD models for MSC30-R32 pair at different adsorption temperatures.

Figure 4.8 illustrates the instantaneous uptake of R32 vapor adsorption onto MSC30, with fitting performed using the Jribi model, LDF model, FD model, and Sultan model. The Jirbi model has a better fitting performance than the other three models, especially in the initial phase. The Jribi model is demonstrated to be in excellent agreement with the experimental results across all adsorption stages, and thus mitigates the uncertainties that may arise during the initial stages of adsorption uptake.

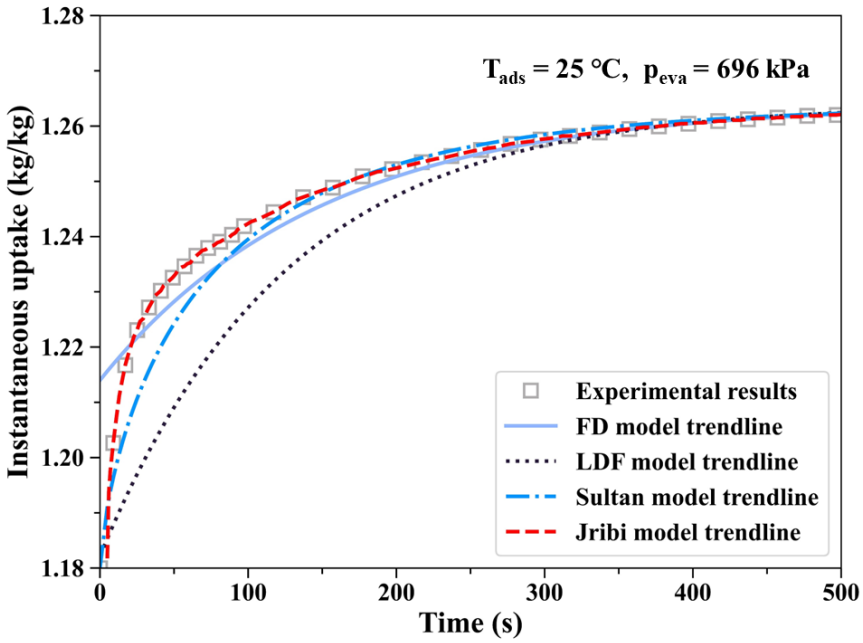

Figure 4.8 Comparison of Jribi model estimation of instantaneous uptake with Sultan, LDF and FD models for MSC30-R32 pair at adsorption temperature of 25°C and evaporation pressure of 696 kPa

4.4.3 Proposed model validation with experimental data

In Jiribi's study, the average value of the mass transfer coefficients k_2 was used for all experimental temperature ranges[19]. As a consequence, this approach may lead to parameter bias and deviations in dynamic adsorption fitting, especially when used under conditions without prior experimental data. Such limitations can result in reduced accuracy and a limited range of applicability, as shown in Figure 4.9. To address these limitations, this study proposes a new mass transfer coefficient model, as shown in Eq.(4.27), to accurately determine the mass transfer coefficient at different temperature ranges and ensure the reliability and accuracy of predictive dynamic adsorption models.

Linear plots of $\ln k_2$ versus T for MSC30-R32 pair is shown in Figure 4.10,

and the fitted parameters are listed in Table 4.2. The proposed model enables the determination of the mass transfer coefficient for the those working pair at any given temperature, utilizing the provided parameters and the proposed equation.

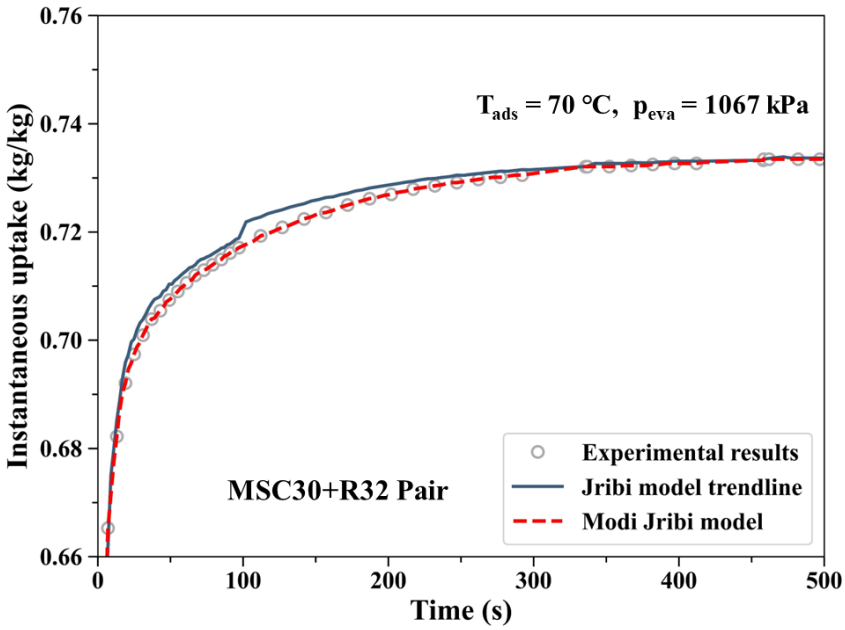

Figure 4.9 Plot of instantaneous uptake against time for MSC30-R32 pair at adsorption temperature of 70°C and evaporation pressure of 1067 kPa

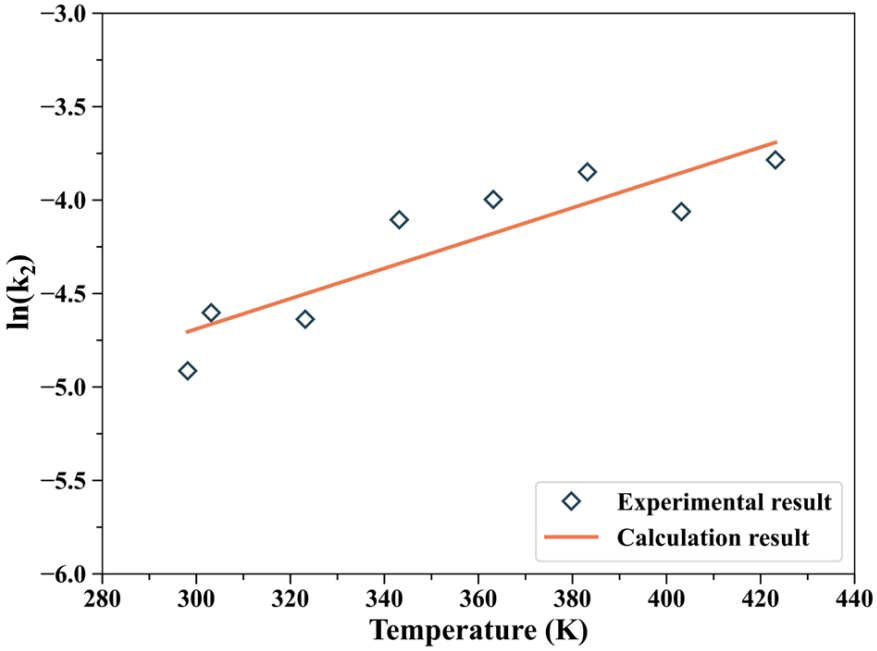

Figure 4.10 Plot of ln(k_2) against temperature for MSC30-R32 pair

In this study, the applicability of the newly proposed equation at different temperatures was first verified by reinserting the mass transfer coefficient calculated based on this model and the fitting parameters into the Jribi model and re-fitting it to experimental data at different temperature-pressure conditions. The fitting results are presented in Figure 4.11 (a) and (b). These images demonstrate that the Jribi model with the newly proposed mass transfer coefficient equation provides a satisfactory representation of the experimental data.

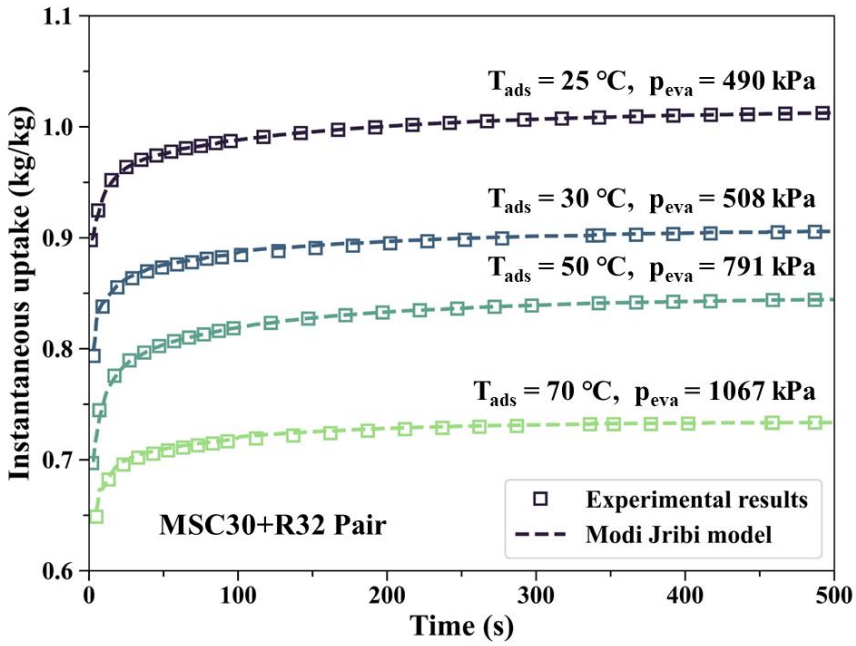

(a) Plot of instantaneous uptake against time at adsorption temperatures below the critical temperature of 78.11 °C

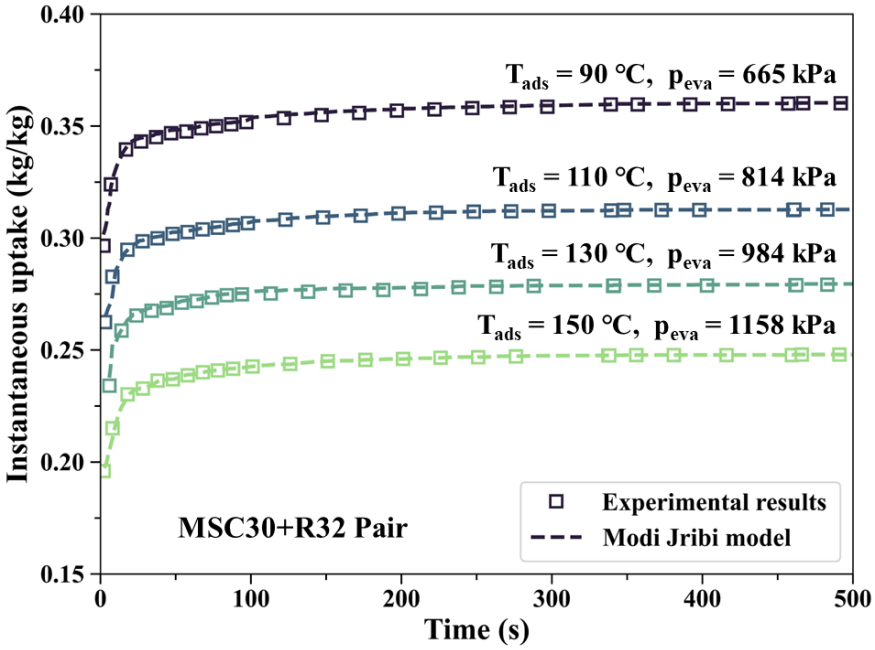

(b) Plot of instantaneous uptake against time at adsorption temperature above the critical temperature of 78.11 ℃

Figure 4.11 Plot of instantaneous uptake against time for MSC30-R32 pair at adsorption temperature of 25, 30, 50, 70, 90, 110, 130, 150℃

The effectiveness of the proposed mass transfer coefficient model for different working pairs was evaluated by analyzing 6 additional sets of adsorption kinetics data obtained from the literatures, including the MSC30-CO_2 pair[19], activated carbon fibers (A-20)-Ethanol pair[22], activated carbon powder-R410a[21], granular activated carbon (AquaSorb 2000)-R404a pair[7], MSC30-R134a pair[16], MSC30-R507a pair[16].

The fitting results of the proposed mass transfer coefficient model are shown in Figure 4.12 and the fitting parameters are furnished in Table 4.2. The proposed model exhibits good fitting performance for all tested working pairs. Based on the fitting parameters in Table 4.2, the mass transfer coefficient values for these working pairs at different temperatures can be readily obtained.

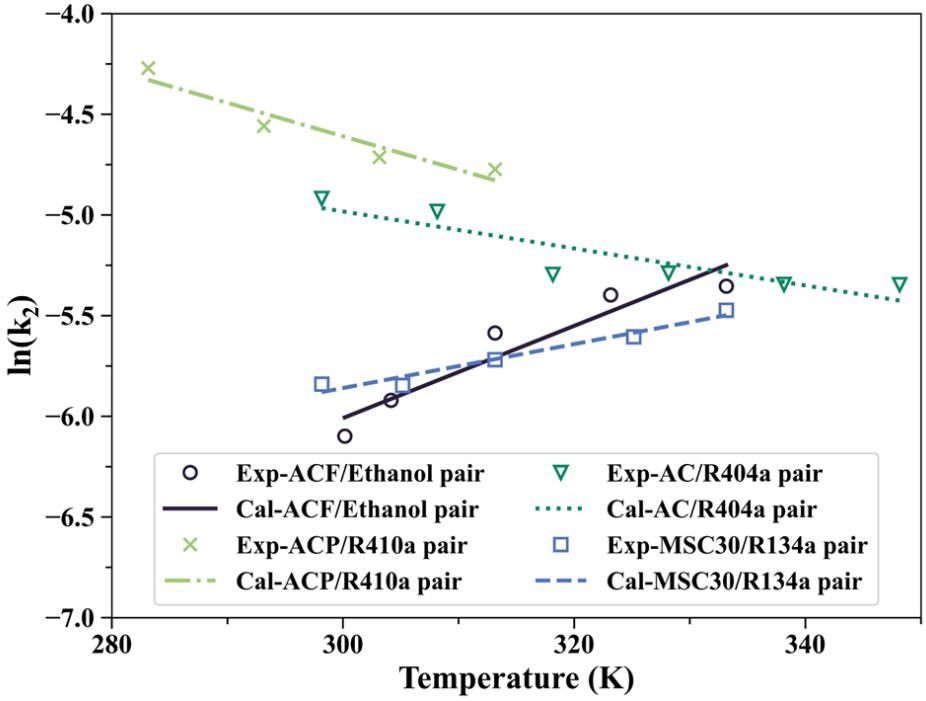

Figure 4.12 Plot of $\ln(k_2)$ against temperature for different working pairs

Table 4.2 Comparison of fitting parameters for different working pairs

Adsorbent	Adsorbate	References	k0	s0
MSC30	R32	Present study	8.09E-04	8.10E-03
MSC30	CO_2	[19]	4.35E-02	-4.10E-03
ACF(A-20)	Ethanol	[22]	2.55E-06	2.29E-02
ACP	R410a	[21]	1.46E+00	-1.66E-02
AC	R404a	[7]	1.08E-01	-9.19E-03
MSC30	R134a	[16]	1.08E-04	1.09E-02
MSC30	R507a	[16]	MSC30	R507a

Similar to the MSC30-R32 working pair, the mass transfer coefficients calculated based on the proposed model and fitted parameters were incorporated into the Jribi model, and the experimental data were fitted at different temperature and pressure

conditions. The fitting results are shown in Figure 4.13-Figure 4.18. The LDF model was used for comparison.

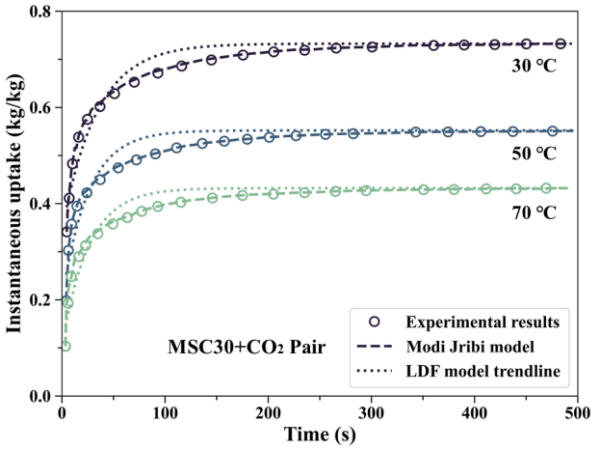

Figure 4.13 Plot of instantaneous uptake against time for MSC30-CO_2 pair at adsorption temperature of 30 50 70℃

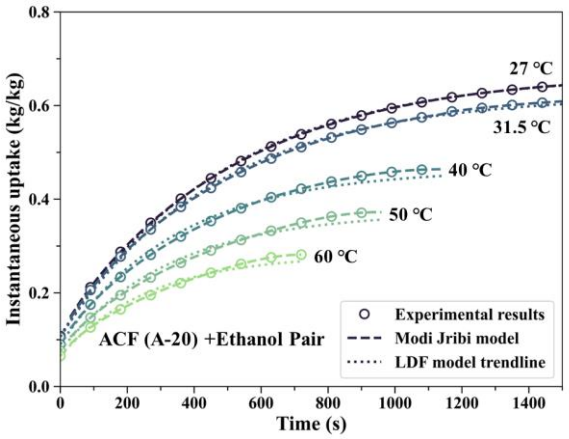

Figure 4.14 Plot of instantaneous uptake against time for activated carbon fibers -Ethanol pair at adsorption temperature of 27, 31.5, 40, 50, 60℃

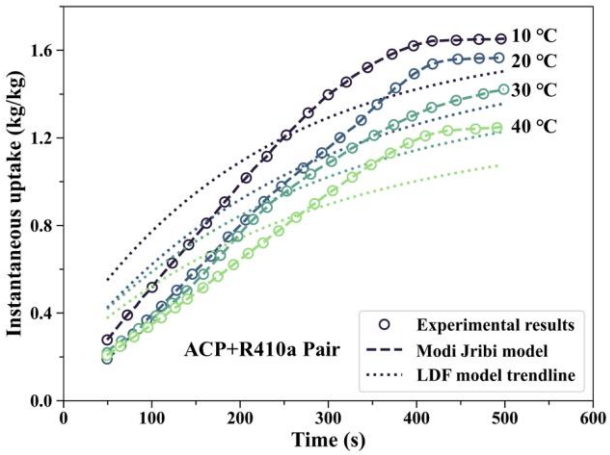

Figure 4.15 Plot of instantaneous uptake against time for activated carbon powder-R410a pair at adsorption temperature of10, 20, 30, 40℃

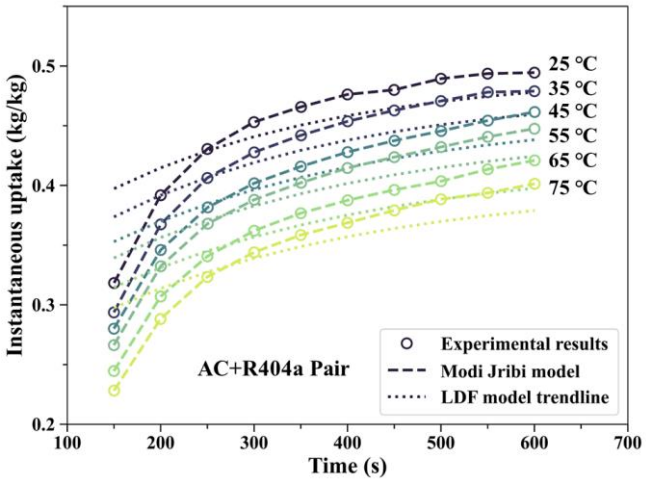

Figure 4.16 Plot of instantaneous uptake against time for granular activated carbon (AquaSorb 2000)-R404a pair at adsorption temperature of 25, 35, 45, 55, 65, 75℃

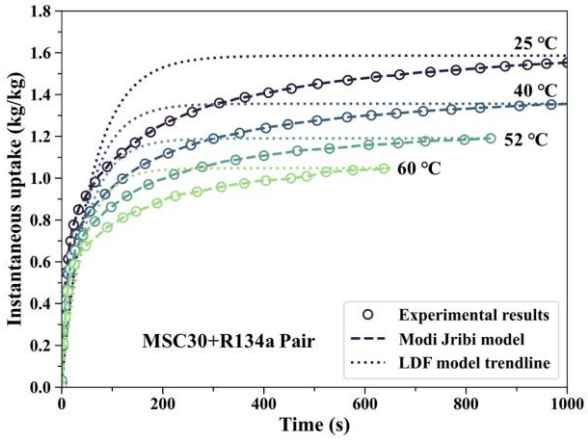

Figure 4.17 Plot of instantaneous uptake against time for MSC30-R134a pair at adsorption temperature of 25, 40, 52, 60℃

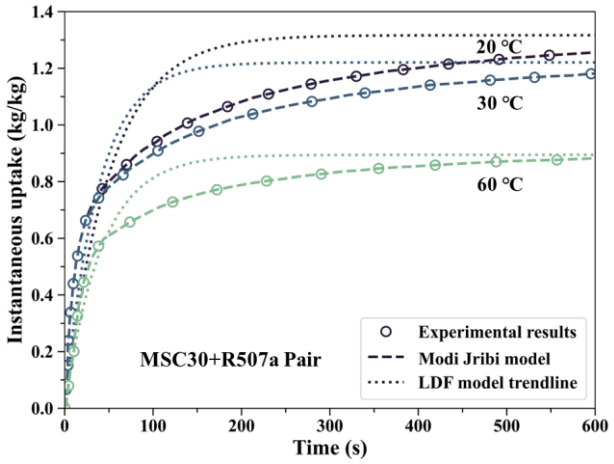

Figure 4.18 Plot of instantaneous uptake against time for MSC30-R507a pair at adsorption temperature of 20, 30, 60℃

Figure 4.13-Figure 4.18 indicates that the Jribi model with the proposed equations exhibited excellent predictive capabilities for the kinetics uptake of various adsorbate - adsorbent pairs at different temperatures. In contrast, the calculation results of the LDF model showed good fitting only for a few working pairs, such as those of ACF-Ethanol pair (Figure 4.14).

4.5 Conclusions

The kinetics of adsorption is a crucial aspect that influences the efficacy of adsorption systems. In this work, the adsorption kinetics of R32 vapor on MSC30 activated carbon powder adsorbent were measured gravimetrically using a MSB unit over a wide range of temperatures from 25 ℃ to 150 ℃. The accuracy of various adsorption kinetics models, including FD model, LDF model, semi-infinite model, and modified adsorption kinetics models, were assessed to determine their suitability for

predicting the kinetics uptake of the MSC30-R32 working pair. Based on the fitting of the Arrhenius equation, the activation energy E_a and pre-exponential coefficient $\frac{D_s}{R_p^2}$ for the MSC30-R32 pair were estimated to be 6262.37 ($kJ \cdot kg^{-1}$). and 0.00853 (s^{-1}), respectively. Among the common MSC30-refrigerant working pairs, the MSC30-R32 pair exhibits the highest diffusion time constant and adsorption rate.

In the evaluation of adsorption kinetics models, Sultan's modified LDF model and Jribi's modified LDF model exhibited superior fitting performance. However, deviations from experimental data were observed under certain operating conditions, particularly in the initial stages of adsorption. In response, this study proposed a new mass transfer coefficient model to enhance the accuracy and extend the applicability range of the Jribi model. Comprehensive validation was carried out using various adsorbent-adsorbate pairs across a wide temperature range. The Jribi model, in combination with the proposed mass transfer coefficient model, accurately and precisely predicts the adsorption kinetics of diverse working pairs, providing valuable insight into their performance under various operating conditions. This research can significantly contribute to the optimization of adsorption systems employing various working pairs for applications such as refrigeration and air conditioning.

4.6 Nomenclature

A	Adsorbent particle surface area (m^2)
AC	Activated carbon
ACF	activated carbon fibers
ACP	activated carbon powder
D_s	Surface diffusion coefficient ($m^2 \cdot s^{-1}$)

D_{s0}	Pre-exponential constant ($m^2 \cdot s^{-1}$)
D_s/R_p^2	Diffusion time constant (s^{-1})
E_a	Activation energy ($kJ \cdot kg^{-1}$)
F	Fractional uptake (-)
F_0	Shape factor of the adsorbent particle (-)
FD	Fickian diffusion
k_2	Mass transfer coefficient in Jribi model (s^{-1})
k_0	Parameter of mass transfer coefficient model (-)
$k_s a_v$	Overall mass transfer coefficient (s^{-1})
LDF	linear driving force
n	Integer number (-)
R	Molar gas constant (8.314 $J \cdot mol^{-1} \cdot K^{-1}$)
R_p	Radius of the adsorbent particle (m)
s_0	Parameter of mass transfer coefficient model (-)
t	Time (s)
T	Temperature (K)
v_{pore}	Specific pore volume of the adsorbent ($m^3 \cdot kg^{-1}$)
V	Adsorbent particle volume (m^3)
w	Instantaneous adsorption uptake ($kg \cdot kg^{-1}$)
w_{abs}	Absolute adsorption uptake ($kg \cdot kg^{-1}$)
w_e	Equilibrium adsorption uptake ($kg \cdot kg^{-1}$)
w_{exc}	Excess adsorption uptake ($kg \cdot kg^{-1}$)
w_0	Initial adsorption uptake ($kg \cdot kg^{-1}$)
θ_t	Dimensionless time (-)
ρ_{ref}	Density of the refrigerant gas ($kg \cdot m^{-3}$)

4.7 References

[1] I. Langmuir. The Adsorption of Gases on Plane Surfaces of Glass, Mica and Platinum, J. *Journal of the American Chemical Society*. 40(2002) 1361-1403, doi: 10.1021/ja02242a004.

[2] E. Glueckauf. Theory of chromatography. Part 10.—Formulæ for diffusion into spheres and their application to chromatography, J. *Trans Faraday Soc*. 51(1955) 1540-1551, doi: 10.1039/tf9555101540.

[3] S.K. Bhatia, M.R. Bonilla, D. Nicholson. Molecular transport in nanopores: a theoretical perspective, J. *Phys Chem Chem Phys*. 13(2011) 15350-15383, doi: 10.1039/c1cp21166h.

[4] J.L. Latham, A.E. Burgess. Elementary Reaction Kinetics, 1918.

[5] Y.I. Aristov, M.M. Tokarev, A. Freni, I.S. Glaznev, G. Restuccia. Kinetics of water adsorption on silica Fuji Davison RD, J. *Microporous and Mesoporous Materials*. 96(2006) 65-71, doi: 10.1016/j.micromeso.2006.06.008.

[6] I.I. El-Sharkawy, K. Uddin, T. Miyazaki, B.B. Saha, S. Koyama, J. Miyawaki, S.H. Yoon. Adsorption of ethanol onto parent and surface treated activated carbon powders, J. *International Journal of Heat and Mass Transfer*. 73(2014) 445-455, doi: 10.1016/j.ijheatmasstransfer.2014.02.046.

[7] M. Ghazy, A.A. Askalany, K. Harby, M.S. Ahmed. Adsorption isotherms and kinetics of HFC-404A onto bituminous based granular activated carbon for storage and cooling applications, J. *Applied Thermal Engineering*. 105(2016) 639-645, doi: 10.1016/j.applthermaleng.2016.03.057.

[8] B. Berdenova, A. Pal, M. Muttakin, S. Mitra, K. Thu, B.B. Saha, A. Kaltayev. A comprehensive study to evaluate absolute uptake of carbon dioxide adsorption onto composite adsorbent, J. *International Journal of Refrigeration-Revue Internationale Du Froid*. 100(2019) 131-140, doi: 10.1016/j.ijrefrig.2019.01.014.

[9] L. Zhou, S.P. Bai, W. Su, J. Yang, Y.P. Zhou. Comparative study of the excess versus absolute adsorption of CO2 on superactivated carbon for the near-critical region, J. *Langmuir*. 19(2003) 2683-2690, doi: 10.1021/la020682z.

[10] E. Glueckauf, J.I. Coates. Theory of chromatography. Part IV. The influence of incomplete equilibrium on the front boundary of chromatograms and on the effectiveness of separation, J. *Journal of the Chemical Society* (1947) 1315-1321, doi.

[11] R.H. Mohammed, O. Mesalhy, M.L. Elsayed, L.C. Chow. Novel compact bed design for adsorption cooling systems: Parametric numerical study, J. *International Journal of Refrigeration-Revue Internationale Du Froid*. 80(2017) 238-251, doi: 10.1016/j.ijrefrig.2017.04.028.

[12] Y.I. Aristov. Optimal adsorbent for adsorptive heat transformers: Dynamic

considerations, J. *International Journal of Refrigeration-Revue Internationale Du Froid*. 32(2009) 675-686, doi: 10.1016/j.ijrefrig.2009.01.022.

[13] M. Mahdavikhah, H. Niazmand. Effects of plate finned heat exchanger parameters on the adsorption chiller performance, J. *Applied Thermal Engineering*. 50(2013) 939-949, doi: 10.1016/j.applthermaleng.2012.08.033.

[14] M. Muttakin, A. Pal, M.J. Rupa, K. Ito, B.B. Saha. A critical overview of adsorption kinetics for cooling and refrigeration systems, J. *Adv Colloid Interface Sci*. 294(2021) 102468, doi: 10.1016/j.cis.2021.102468.

[15] C. Yang, Y. Gu. Modeling of the adsorption kinetics of surfactants at the liquid-fluid interface of a pendant drop, J. *Langmuir*. 20(2004) 2503-2511, doi: 10.1021/la0360097.

[16] K. Habib, B.B. Saha, K.A. Rahman, A. Chakraborty, S. Koyama, K.C. Ng. Experimental study on adsorption kinetics of activated carbon/R134a and activated carbon/R507A pairs, J. *International Journal of Refrigeration-Revue Internationale Du Froid*. 33(2010) 706-713, doi: 10.1016/j.ijrefrig.2010.01.006.

[17] M.J. Rupa, A. Pal, S. Mitra, B.B. Saha. Time adapted linear driving force model for gas adsorption onto solids, J. *Chemical Engineering Journal*. 420(2021), doi: ARTN 129785 10.1016/j.cej.2021.129785.

[18] M. Sultan, I.I. El-Sharkawy, T. Miyazaki, B.B. Saha, S. Koyama, T. Maruyama, S. Maeda, T. Nakamura. Water vapor sorption kinetics of polymer based sorbents: Theory and experiments, J. *Applied Thermal Engineering*. 106(2016) 192-202, doi: 10.1016/j.applthermaleng.2016.05.192.

[19] S. Jribi, T. Miyazaki, B.B. Saha, A. Pal, M.M. Younes, S. Koyama, A. Maalej. Equilibrium and kinetics of CO2 adsorption onto activated carbon, J. *International Journal of Heat and Mass Transfer*. 108(2017) 1941-1946, doi: 10.1016/j.ijheatmasstransfer.2016.12.114.

[20] S.W. Rutherford, J.E. Coons. Equilibrium and kinetics of water adsorption in carbon molecular sieve: theory and experiment, J. *Langmuir*. 20(2004) 8681-8687, doi: 10.1021/la049330d.

[21] A.A. Askalany, B.B. Saha, I.M. Ismail. Adsorption isotherms and kinetics of HFC410A onto activated carbons, J. *Applied Thermal Engineering*. 72(2014) 237-

243, doi: 10.1016/j.applthermaleng.2014.04.075.

[22] B.B. Saha, I.I. El-Sharkawy, A. Chakraborty, S. Koyama, S.H. Yoon, K.C. Ng. Adsorption rate of ethanol on activated carbon fiber, J. *Journal of Chemical and Engineering Data*. 51(2006) 1587-1592, doi: 10.1021/je060071z.

Chapter 5
Steady-State Cycle Analysis for Adsorption Cooling Application

5.1 Introduction

The adsorption heat pump system possesses notable advantages that make it an attractive potential alternative to conventional vapor compression heat pump cycles and absorption heat pump systems. Firstly, it exhibits the capability to operate efficiently with low-grade heat sources, such as solar energy or industrial waste heat, which enhances its energy sustainability and promotes the utilization of otherwise wasted thermal energy. Secondly, due to its simplified design and minimal moving components, the system exhibits reduced noise and vibration levels, thereby ensuring a more favorable operating environment. Additionally, the primary power-consuming element in the adsorption heat pump system is the circulation pump for the refrigerant, leading to significantly reduced power consumption compared to other heat pump technologies. This feature enhances the system's energy efficiency and contributes to its economic viability. Moreover, the utilization of environmentally friendly refrigerant working pairs eliminates concerns related to environmental harm, corrosion, and toxicity[1-4]. These distinctive merits position adsorption heat pump systems as promising alternatives to conventional steam compression heat pump cycles and absorption heat pump systems. Consequently, researchers have increasingly directed

their attention towards exploring and investigating the potential of adsorption heat pump systems[5-7].

Steady-state equilibrium cycle analysis is a well-established approach employed in the study of adsorption heat pump performance. This method involves a thorough examination of the thermodynamic cycle of the adsorption process, aiming to ascertain the interrelations among equilibrium pressures, temperatures, and adsorption capacities within the adsorbent bed. These parameters serve as key indicators of the heat pump's performance characteristics. It is important to note that equilibrium analysis disregards the influence of adsorption kinetics, assuming a state of thermodynamic equilibrium between the adsorbent and the adsorbate. This pivotal assumption significantly impacts the outcomes of the analysis. Additionally, the method assumes time-independent operation of the cycle, thereby neglecting the effects of pressure drop and thermal losses. Despite these simplifying assumptions, equilibrium cycle analysis is widely embraced due to its straightforwardness, expediency, and ability to provide estimations of the thermodynamic performance of specific working pairs under ideal conditions. Seo et al[8]. developed an improved equilibrium model and investigated the performance of two different adsorption cooling and adsorption heat transformer cycles, using Maxsorb III + R245fa and spherical activated carbon (SAC-2)-R245fa. Animesh et al[7]. investigated the thermodynamic properties of activated carbons prepared from waste palm trunk with high CO_2 adsorption capacity, to understand the performance of practical adsorption cooling systems. The result showed that the studied activated carbons showed promising results with an SCE improvement of up to 74% compared to Maxsorb III.

This chapter focuses on the development of the equilibrium thermodynamic model for equilibrium adsorption refrigeration cycles, taking into account the

adsorption isotherm models, adsorption heat, and specific heat capacity models derived from previous chapters. The main objective is to investigate the thermodynamic performance of a low-temperature-driven adsorption heat pump utilizing the MSC30-R32 working pair. The analysis includes a comprehensive examination of the impact of operating parameters, such as adsorption temperature, evaporation temperature, desorption temperature, and mass ratio, on key performance indicators like Specific Cooling Energy (SCE) and Coefficient of Performance (COP) of the heat pump cycle.

Moreover, a comparative study is conducted to compare the working conditions and performance characteristics of the MSC30-R32 working pair with other commonly employed adsorbent-refrigerant pairs, such as MSC30-CO_2, MSC30-R245fa and Chemviron AC-Ethane, etc. This analysis aims to provide insights into the suitability and effectiveness of different working pairs in adsorption heat pump systems. The findings from this research contribute to a better understanding of the thermodynamic behavior and optimization of adsorption-based refrigeration cycles.

5.2 Theory and Mathematical Approach

The schematic representation of a typical adsorption heat pump system, as depicted in Figure 5.1, comprises of key components including evaporator, condenser, expansion valve, and two adsorption beds filled with a suitable adsorbent material. The relationship between the pressure, temperature, and the amount of adsorbed refrigerant at equilibrium can be represented by a pressure-temperature-concentration (p-T-w) diagram, which provides a visual representation of the thermodynamic properties of the adsorption process. In the context of typical operating conditions in an adsorption

refrigeration system, where the adsorption temperature, desorption temperature, and evaporation temperature are set at 30°C, 90°C, and 7°C, respectively, the p-T-w diagram for the ideal adsorption cooling cycle utilizing the MSC30-R32 working pair is presented in Figure 5.2. Moreover, in order to visually depict the variations in adsorption capacity and pressure throughout the adsorption cycle, the w-p diagram showcasing the adsorption cycle under the same operating conditions is illustrated in Figure 5.3

The ideal cycle can be described as follows:

(i). During the adsorption process (a-b), the adsorption bed is connected to the evaporator. The refrigerant vapor evaporates in the evaporator, absorbing its latent heat from the chilled water, and is then adsorbed by the adsorbent material packed in the adsorption bed through valve V3. As the adsorption process progresses, the adsorption uptake increases from w_{min} to w_{max}, while the pressure is maintained at a constant value of p_{evap}. As adsorption is an exothermic process, it is important to have a cooling system in place to keep the process running smoothly.

(ii). In the pre-heating (b-c) process, the adsorption bed is kept separate from the evaporator and condenser and is heated by a high-temperature heat source, typically a waste heat source. As the temperature rises, the refrigerant is continuously desorbed from the adsorbent surface, leading to an increase in pressure within the adsorption bed, from p_{evap} to p_{cond}.

(iii). Once the pressure reaches p_{cond}, the adsorption bed and condenser are connected, initiating the desorption process (c-d). This process is an endothermic process, in which the adsorption bed is continually heated and the quantity of adsorbed refrigerant within the adsorption bed decreases from w_{max} to w_{min}. The refrigerant vapor is liquefied inside the condenser, and the heat generated during this process is

removed by the circulation of cooling water. The cooled liquid refrigerant is then directed back to the evaporator through the expansion valve.

(iv). In the pre-cooling(d-a) process, the valves connecting the adsorption bed to the evaporator and condenser are simultaneously closed and the adsorption bed is cooled by the cooling load, resulting in a decrease in pressure from p_{cond} to p_{evap}.

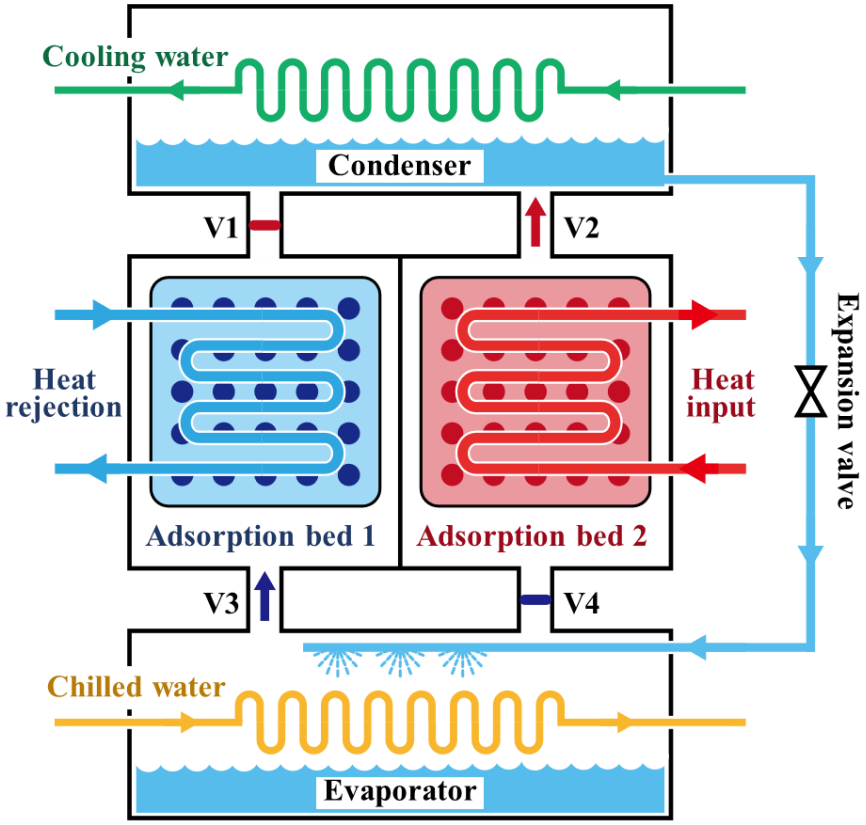

Figure 5.1 Schematic diagram of ideal adsorption cooling system

Figure 5.2 and Figure 5.3, illustrate the performance of an adsorption refrigeration cycle employing the MSC30-R30 working pair. The cycle operates under specific conditions, with the adsorption and desorption temperatures set at 30°C and 90°C, respectively, while the evaporation and condensation temperatures are maintained at 7°C and 30°C. Notably, the maximum adsorption uptake achieved in this

cycle is recorded as 1.36 kg·kg^{-1}, while the adsorption uptake after desorption is found to be 0.75 kg·kg^{-1}, effective adsorption amount is 0.61 kg·kg^{-1}. These values represent 82% and 54% of the corresponding saturated adsorption capacity under the given operating conditions. Furthermore, the adsorption-desorption cycle reveals that the adsorption bed experiences a maximum pressure of 1927.51 kPa and a minimum pressure of 1011.50 kPa. Following the preheating process, the adsorption bed reaches a temperature of 49.62°C, while it achieves a temperature of 63.27°C after the precooling process. These findings provide valuable insights into the performance characteristics and operating parameters of the MSC30-R30 adsorption refrigeration system.

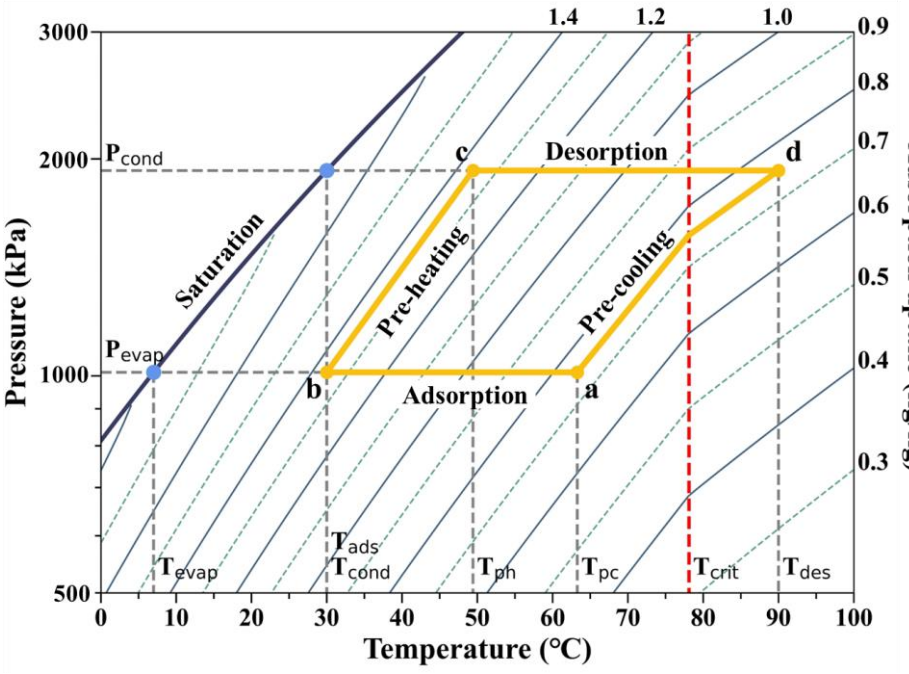

Figure 5.2 Representation of cooling cycle on p-T-w diagram of MSC30-R32 pair with adsorption temperature of 30 °C and desorption temperature of 90 °C

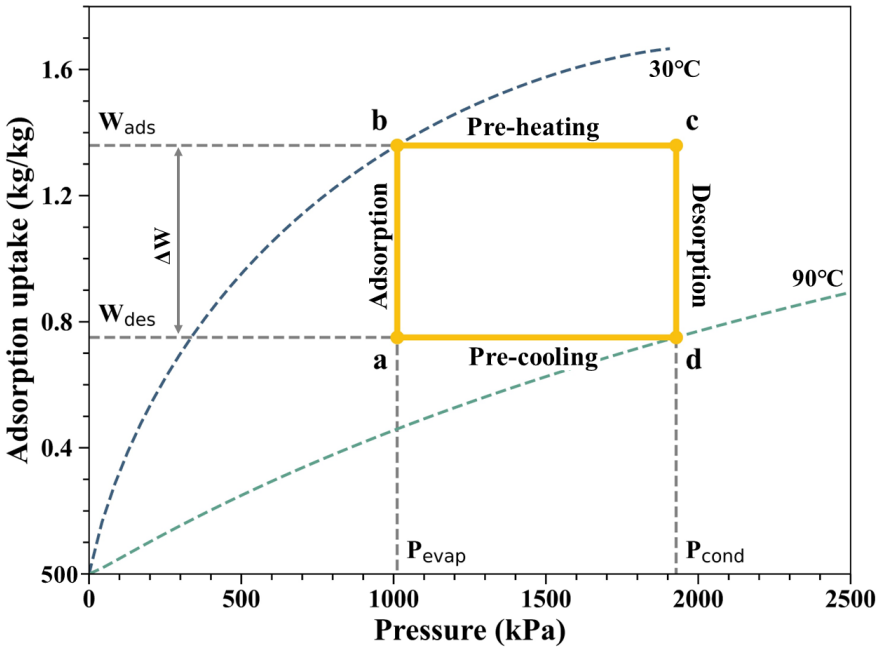

Figure 5.3 Representation of cooling cycle on w-p diagram of MSC30-R32 pair with adsorption temperature of 30 °C and desorption temperature of 90 °C

For the evaluation of adsorption cooling cycles, the evaluation metrics commonly used are the specific cooling energy (SEC) and coefficient of performance (COP),

$$SEC = (w_{max} - w_{min})\left[h_{fg}(T_{evap}) + \int_{cond}^{evap} dh_{satliq}\right] \tag{5.1}$$

$$COP = \frac{SCE}{q_{tot}} \tag{5.2}$$

Here, $w_{max} - w_{min}$ corresponds to the disparity between the maximum and minimum adsorption uptakes observed during the cycle, thereby denoting the effective adsorption capacity Δw (kg·kg^{-1}), $h_{fg}(T_{evap})$ is the specific enthalpy of evaporation of the adsorbate at the evaporation temperature (kJ·kg^{-1}), h_{satliq} is the specific enthalpy of saturated liquid (kJ·kg^{-1}), q_{tot} is the total specific heat input, which consists of latent and sensible heat as,

$$q_{tot} = q_{lat} + q_{sen} \tag{5.3}$$

$$q_{lat} = \int_{T_{ph},p_{cond}}^{T_{des},p_{cond}} q_{st}(p,T)\, dw \tag{5.4}$$

$$q_{sen,term1} = \int_{T_{ads}}^{T_{des}} c_{p,ads}(T)\, dT \tag{5.5}$$

$$q_{sen,term2} = w_{max} \int_{T_{ads},p_{evap}}^{T_{ph},p_{cond}} c_{p,aded}(p,T)\, dT \tag{5.6}$$

$$q_{sen,term3} = \int_{T_{ph},p_{cond}}^{T_{des},p_{cond}} w(p,T) c_{p,aded}(p,T)\, dT \tag{5.7}$$

$$q_{sen,term4} = \frac{m_{bed}}{m_{ads}} \int_{T_{ads}}^{T_{des}} c_{p,bed}\, dT \tag{5.8}$$

$$q_{sen} = q_{sen,term1} + q_{sen,term2} + q_{sen,term3} + q_{sen,term4} \tag{5.9}$$

Here, Eq.(5.4) represents the latent heat of the refrigerant adsorbed in the adsorption bed during the pre-heating process. The right-hand side of Eq. (5.9) comprises of four distinct terms, the first of which represents the sensible heat of the adsorbent during both the pre-heating and desorption processes. The second and third terms correspond to the sensible heat of the adsorbed phase during the pre-heating and desorption process, respectively. The fourth term represents the sensible heat of the metal heat exchanger of the adsorption bed, during both the pre-heating and desorption processes.

$c_{p,aded}$ is the specific heat capacity of the adsorbate in adsorbed phase ($J \cdot kg^{-1} \cdot K^{-1}$), the model is given by[9],

$$c_{p,aded}(T,p) = \begin{cases} c_{p,satliq}, & p < p_{atm} \\ c_{p,satliq} + \alpha^2 T \frac{E(1-n)}{mm \cdot n^2} [-\ln\theta]^{\frac{1}{n}-2}, & \mathrm{T} < \mathrm{T_{crit}} \\ c_{p,gas} - \frac{kR}{mm} + \alpha^2 T \frac{E(1-n)}{mm \cdot n^2} [-\ln\theta]^{\frac{1}{n}-2}, & T > T_{crit}\ \&\ p < p_{crit} \\ c_{p,gas}(T,p), & \text{otherwise} \end{cases} \tag{5.10}$$

$c_{p,ads}$ is the specific heat capacity of adsorbent which is given as[8],

$$c_{p,ads}(T) = a_0 - a_1 T + a_2 T^2 - a_3 T^3 + a_4 T^4 \quad (5.11)$$

In present study, the heat exchanger is assumed to be made of aluminium and its specific heat capacity $c_{p,bed}$ is calculated by[8],

$$c_{p,bed}(T) = (b_0 + b_1 T) \times b_2 / b_3 \quad (5.12)$$

Table 5.1 gives the coefficients for the specific heat capacity used in Eq. (5.11) and Eq. (5.12)

Table 5.1 Coefficients for the specific heat capacity of the adsorbent and heat exchanger

Coefficient	MSC 30[8]	Coefficient	Heat exchanger[8]
a_0	27987.4	b_0	4.94
a_1	-312.06	b_1	0.00296
a_2	1.32895	b_2	4184
a_3	-0.00249144	b_3	26.981539
a_4	1.74482×10-6		

5.3 Results and Discussion

5.3.1 Steady-state Equilibrium Cycle Analysis

In this section, to further assess the impact of the MSC30-R32 working pair on the thermodynamic performance of the adsorption cycle for cooling applications, the

equilibrium cycle analysis is performed. The heat pump system is thermally powered using a heat source at different temperatures, from 30 °C to 150 °C. The performance indicators of the equilibrium cycle, the SCE and the COP, are estimated using Eqs. (5.1)-(5.12) at different desorption temperatures and evaporation temperatures.

Figure 5.4 and Figure 5.7 depict the influence of varying adsorption and desorption temperatures on the SCE and COP of an adsorption heat pump system utilizing MSC30-R32 as the working pair The simulation were conducted with a fixed evaporating temperature of 7°C while systematically altering the adsorption temperature between 10°C and 40°C, and the desorption temperature between 50°C and 150°C. The results demonstrate that lowering the adsorption temperature or increasing the desorption temperature leads to an incremental enhancement in both SCE and COP of the heat pump system. The maximum values observed for SCE and COP are 461.09 kJ/kg and 0.48, respectively. Notably, it should be emphasized that selecting inappropriate adsorption and desorption temperature combinations, particularly when the adsorption temperature exceeds 30°C and the desorption temperature approaches 50°C, may result in an unfavorable scenario where the input energy surpasses the output energy, thereby yielding negative SCE and COP values. This region, characterized by energy inefficiency, is referred to as the "inefficient region" as highlighted in Figure 5.4 and Figure 5.7.

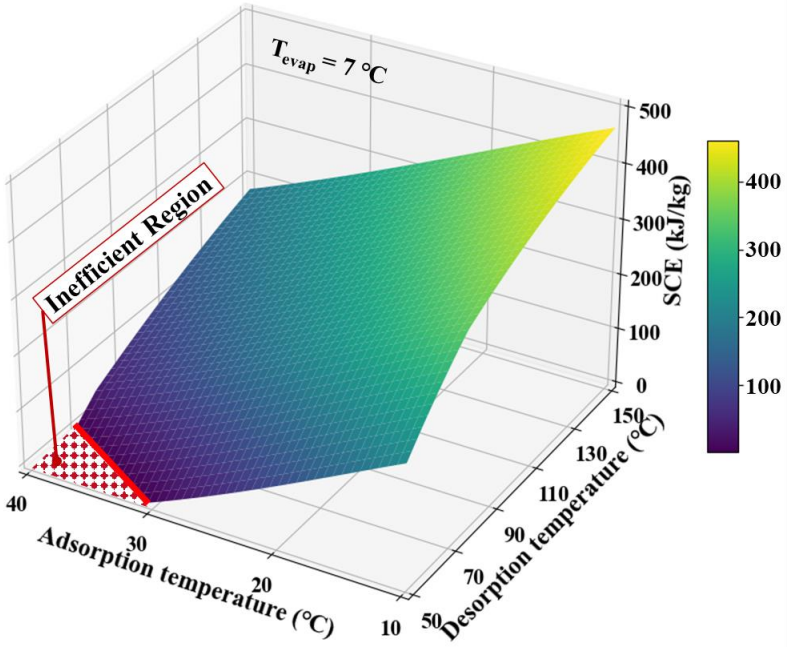

Figure 5.4 Effect of different evaporation temperatures and desorption temperatures on Specific cooling energy

Furthermore, Figure 5.5 illustrates the effect of desorption temperature on the SCE at evaporation temperatures of 7 °C and different adsorption temperatures ranging from 20 °C to 40 °C. Figure 5.6 illustrates the influence at adsorption temperatures of 30 °C and different evaporation temperatures ranging from 2 °C to 12 °C. It is noticed that the SCE linearly increases with the increase in desorption temperature due to the contribution of the adsorption uptake difference term ($w_{max} - w_{min}$). The increase in the desorption temperature causes more refrigerant molecules to detach from the adsorbent surface. This, in turn, leads to an increase in the effective adsorption amount within the cycle, resulting in an improvement in the cooling capacity of the cooling system.

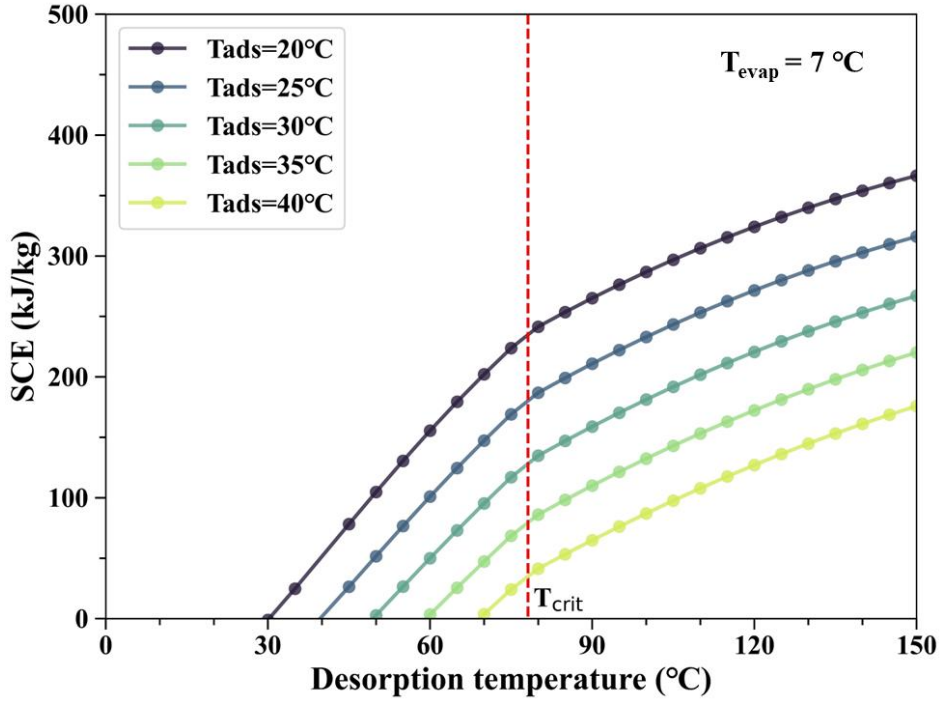

Figure 5.5 Effect of different desorption temperatures on SCE at different adsorption temperatures

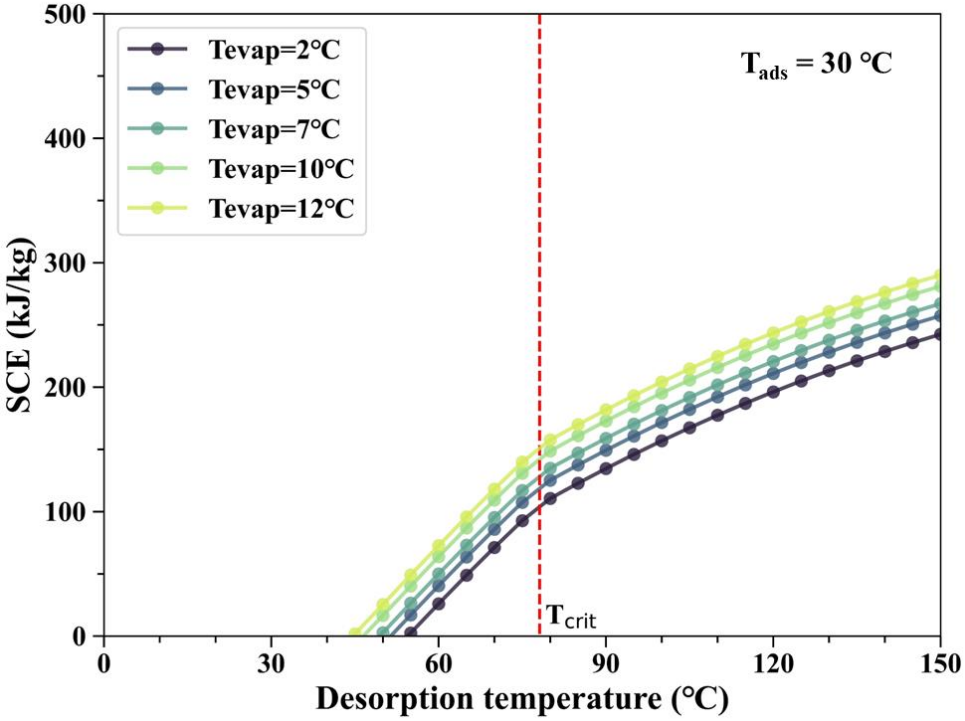

Figure 5.6 Effect of different desorption temperatures on SCE at different evaporation temperatures

The influence of desorption temperature on COP at evaporation temperatures of 7 °C and various adsorption temperatures ranging from 20 °C to 40 °C is depicted in Figure 5.8. It is noted here that as the desorption temperature increases, the COP initially rises rapidly. However, as the temperature continues to increase, the rate of COP increase slows down. Once the critical temperature is exceeded, the COP value only shows a very limited increase. When the adsorption temperature is 25°C, the COP reaches its highest value of 0.47 at a desorption temperature of 115 °C and gradually decreases as the temperature rises beyond that point even though SCE increases linearly. When the desorption temperature reaches the critical point of 78.11 °C for R32, the COP of the cooling cycle is 0.43, which is 90.5% of its highest value. As the desorption temperature increases, the minimum desorption uptake decreases, leading to increased consumption of thermal energy required to separate the refrigerant molecules from the surface of the adsorbent. Consequently, the increase in latent heat is more pronounced than that of the SCE, leading to a slow increase or even decrease of COP as desorption temperature continues to rise within the supercritical regime.

It is also found that for the fixed evaporation temperature of 7 °C, the minimum desorption temperatures needed are about 31, 39, 49,58 and 69 °C corresponding to the adsorption temperature of 20, 25, 30, 35 and 40 °C. If the desorption temperature is below these minimum values, theoretically the MSC 30 and R32 working pair will be unable to provide cooling.

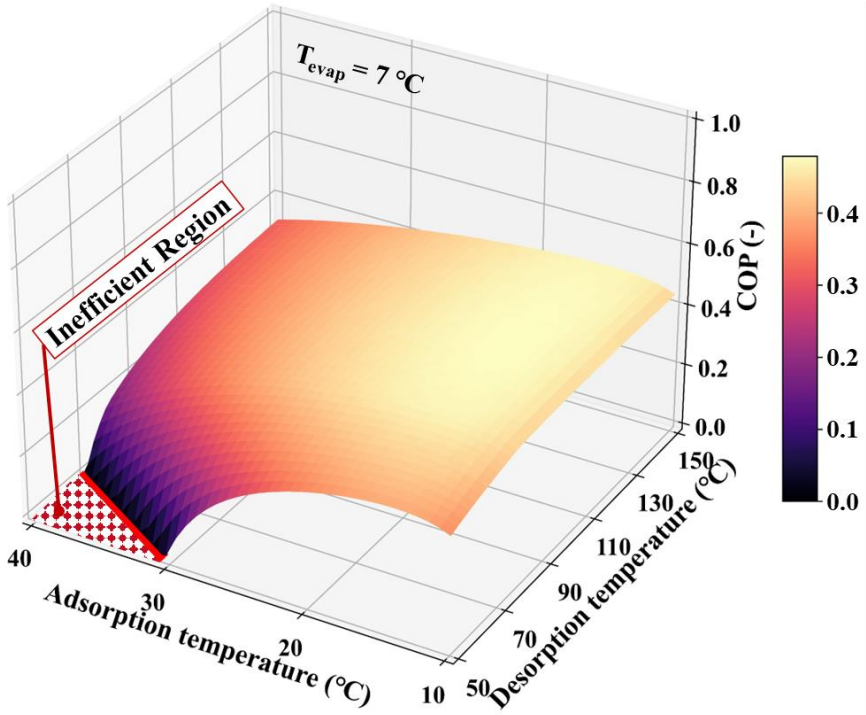

Figure 5.7 Effect of different evaporation temperatures and desorption temperatures on COP

For the fixed adsorption temperature of 30°C, the influence of desorption temperature on COP at different evaporation temperatures is illustrated in Figure 5.9. As can be seen from Figure 5.5-Figure 5.9, the SCE and COP of the system increase progressively with either a reduction in adsorption temperature or an increase in evaporation temperature. This is due to the fact that an increase in evaporation temperature and a decrease in adsorption temperature result in a rise in the maximum adsorption uptake of the adsorption bed, thereby leading to an enhancement in the effective adsorption capacity and subsequently the performance of the system.

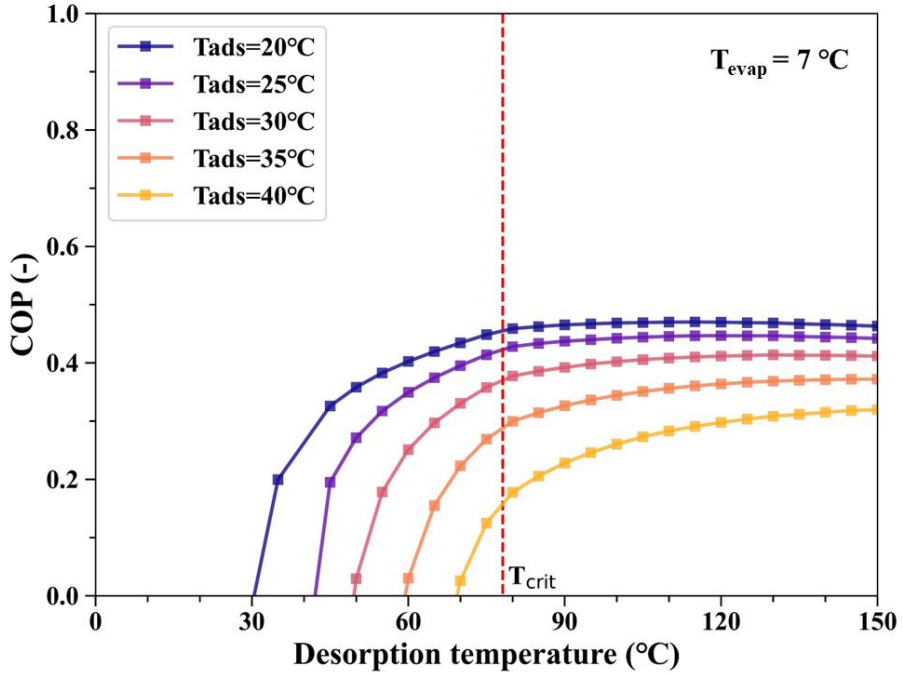

Figure 5.8 Effect of different desorption temperatures on COP at different adsorption temperatures

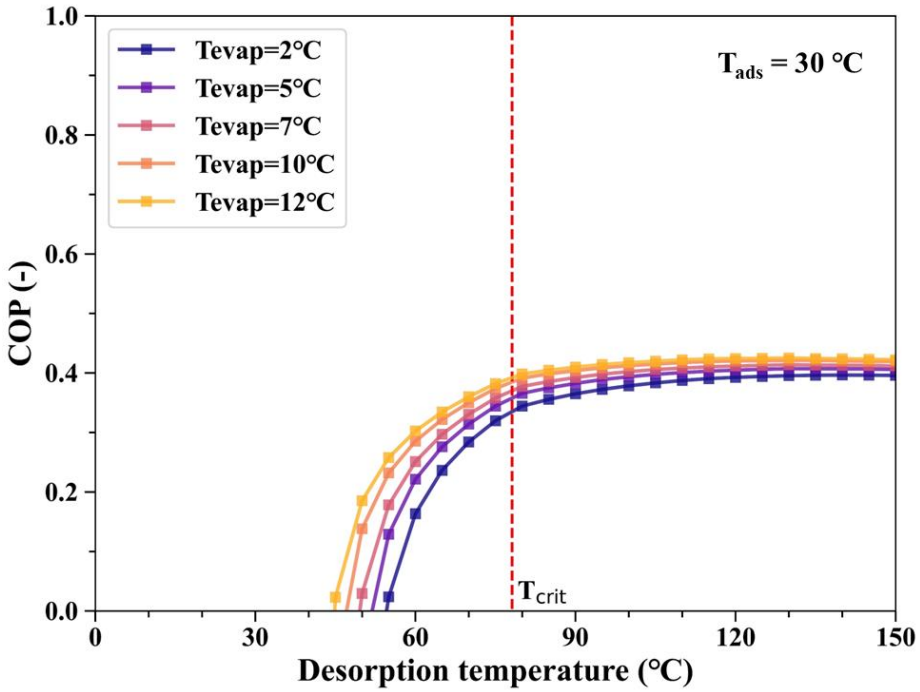

Figure 5.9 Effect of different desorption temperatures on COP at different evaporation temperatures

In the operation of adsorption heat pump cycles, the adsorption bed undergoes a continuous process of heating and cooling to facilitate the adsorption and desorption processes. During the temperature variation of the adsorption bed, a substantial amount of heat is utilized to either increase or remove the sensible heat from different components within the adsorption bed, including the heat exchanger's metal pipes and fins. Thus, apart from considering the temperature conditions governing the heat pump operation, the quality and sensible heat of the adsorption bed heat exchanger significantly influence the overall performance of the heat pump system. This study focuses on evaluating the heat exchanger's performance by analyzing the heat exchanger to effective-adsorbent mass ratio $\frac{m_{bed}}{m_{ads}}$. The specific heat capacity of the adsorption bed heat exchanger is determined using Eq (5.12), while the sensible heat is calculated using Eq (5.8). The heat pump system's COP under different mass ratios is presented and analyzed in Figure 5.10.

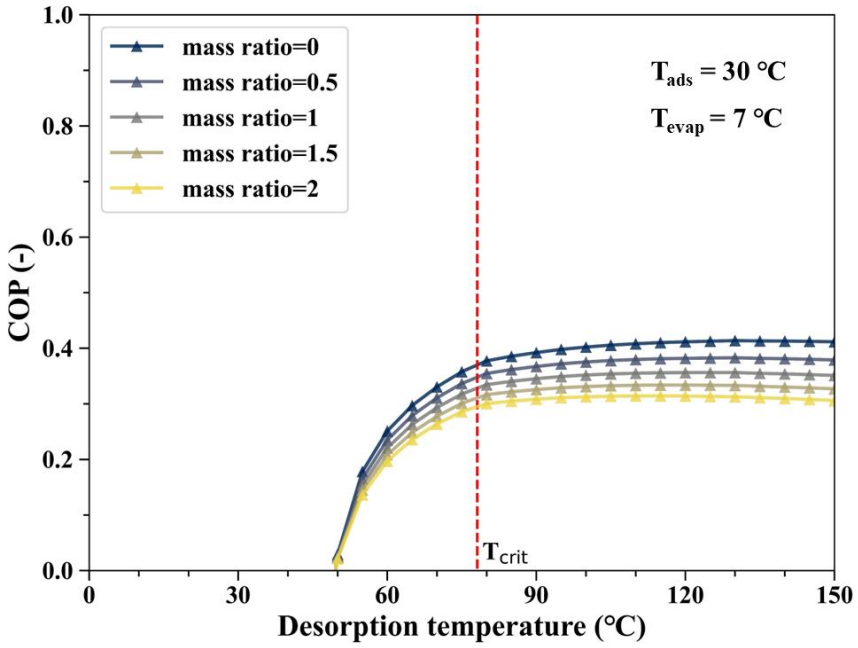

Figure 5.10 The effect of the thermal mass ratio of the heat exchanger and the adsorbent on the COP values

The sensible heat of the adsorption heat exchanger solely affects the sensible heat component of the heat pump system, while having no impact on the cooling capacity of the working fluid pairs. Therefore, the SCE of the heat pump remains constant across different mass ratios. Figure 5.10 illustrates that under identical temperature conditions, as the mass ratio varies from 0 to 2, the system's COP gradually decreases. This decline becomes more pronounced at higher desorption temperatures. For a desorption temperature of 120 °C, the COP of the adsorption-based heat pump with a mass ratio of 2 experiences a reduction of 0.098 compared to the COP of a pure adsorbent heat exchanger. At lower desorption temperatures, the influence of the mass ratio on the heat pump's COP is relatively minimal, attributed to the narrow temperature range of the adsorption bed, resulting in reduced heat losses associated with the metal pipes and fins. Hence, it is advisable to minimize the mass of heat exchange pipes and fins within the adsorption bed or consider utilizing materials with lower specific heat capacity. Examples of such materials include aluminum metal foams or carbon-based scaffold materials, which possess superior thermal conductivity while maintaining low density and specific heat capacity.

5.3.2 Cycle Analysis of Alternative Working Pairs

As discussed in Section 2.2.2, R32 possesses distinct advantages, including low global warming potential (GWP), cost-effectiveness, availability, and enhanced safety compared to other commonly utilized refrigerants. This section presents a comprehensive comparative analysis of the steady-state cycle performance of adsorption heat pumps employing diverse working fluid pairs, such as R245fa, R134a, CO_2, Methane, etc. The thermal properties and data employed in the steady-state

calculations for each working fluid pair are succinctly summarized in Table 5.2. Specifically, the MSC30-R32, MSC30-Methane, and Chemviron AC-Ethane working fluid pairs were derived through fitting isotherm data obtained from relevant literature sources[10-12], as expounded in Section 2.5.3. Conversely, the parameters for MSC30-R134a and MSC30-R245fa were sourced from existing literature studies [8, 9].

Table 5.2 Properties and fitted parameters of the alternative refrigerants

Adsorbent	MSC30	MSC30	MSC30	Ch-AC	MSC30	MSC30
Refrigerant	R32	CO2	Methane	Ethane	R245fa	R134a
T_{crit} (°C)	78.11	30.98	-82.59	32.17	153.86	101.06
mm ($g \cdot mol^{-1}$)	52.02	44.01	16.04	30.07	134.05	102.03
c_0 ($cm^3 \cdot g^{-1}$)	1.75	1.59	1.21	0.64	1.44	1.73
E ($J \cdot mol^{-1}$)	5133.35	5490.51	5158.23	7313.98	9862.60	7997.14
n (-)	1.37	1.32	1.30	1.21	1.66	1.37
κ (-)	19.03	21.12	11.07	18.14	-	-
μ (-)	-2.31	-0.57	-2.29	-69.87	-	-

Under typical operating conditions of an adsorption heat pump, where the adsorption temperature, desorption temperature, and evaporation temperature are set at 30°C, 90°C, and 7°C, respectively, the adsorption heat pump cycles of various adsorbent-adsorbate working pairs on the isotherms are presented in Figure 5.11 (a) and (b). The corresponding changes in working pressure and adsorption capacity are summarized in Table 5.3.

Table 5.3 Working pressure and adsorption capacity variations in different working pairs in adsorption heat pump cycles

Adsorbent	MSC30	MSC30	MSC30	MSC30	MSC30
Refrigerant	R32	CO_2	Methane	R134a	R245a
Adsorption pressure (kPa)	1011.50	4176.54	9922.56	374.63	72.59
Desorption pressure (kPa)	1927.51	7213.69	11614.55	770.20	178.08
Max uptake ($kg \cdot kg^{-1}$)	1.36	1.31	0.34	1.86	1.76
Min uptake ($kg \cdot kg^{-1}$)	0.75	0.90	0.28	1.22	1.23
Δw ($kg \cdot kg^{-1}$)	0.61	0.41	0.06	0.64	0.52

The adsorption heat pump operating with the MSC30-R32 working pair demonstrates considerably lower working pressures, ranging from 1011.05 to 1927.51 kPa, compared to heat pump cycles utilizing CO_2 and Methane as adsorbates. Higher working pressures impose stricter requirements on system sealing, safety, and operating environment. Hence, in contrast to these natural refrigerants, the MSC30-R32 adsorption heat pump exhibits lower demands in terms of sealing performance and cost. It is worth noting that, under similar temperature and pressure conditions, MSC30 exhibits significantly higher adsorption capacity than CO_2 and Methane. This discrepancy in adsorption capacity accounts for the lower working pressure and larger adsorption capacity variation observed in the MSC30-R32 working pair when compared to CO_2 and Methane. In contrast, the utilization of the MSC30-R32 working pair in the adsorption heat pump system results in higher operating pressures and lower adsorption capacities compared to the HFC refrigerants R134a and R245fa.

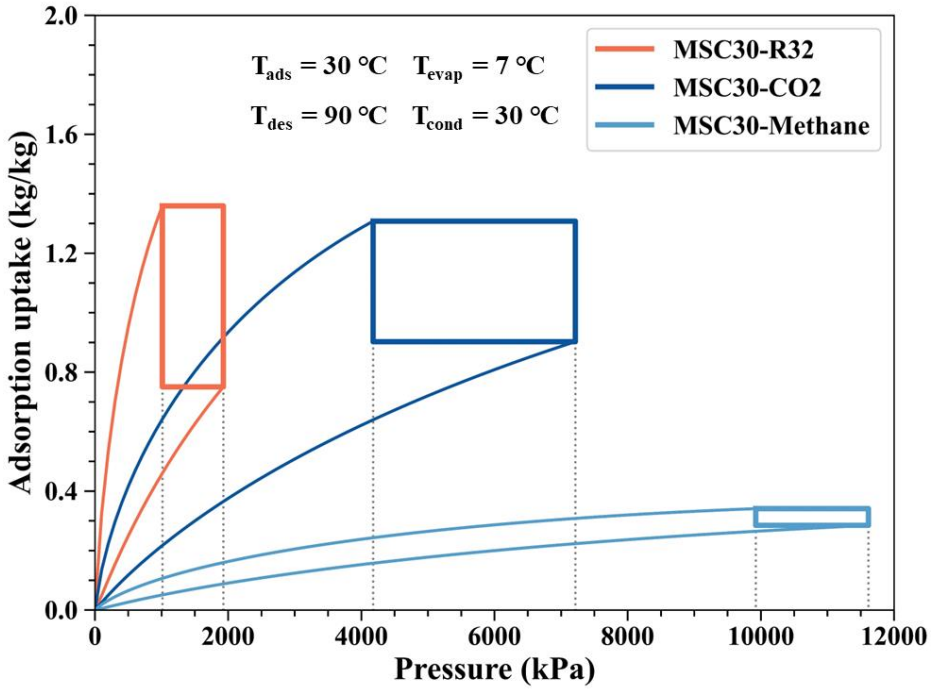

(a) Operating profiles for MSC30-R32, MSC30-CO_2, MSC30-Methane pairs

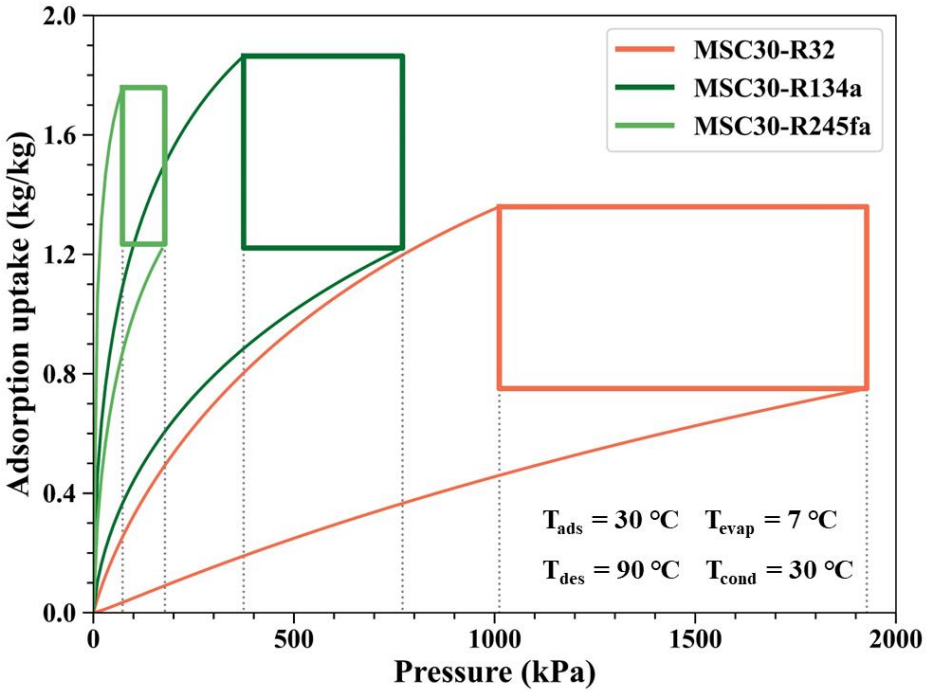

(b) Operating profiles for MSC30-R32, MSC30-R134a, MSC30-R245fa pairs

Figure 5.11 Representation of cooling cycle on w-p diagram of different working pairs at T_{ads} of 30 °C, T_{des} of 90°C and T_{evap} of 7°C

Furthermore, Figure 5.12 and Figure 5.13 showcase the influence of desorption temperature on the performance of adsorption heat pump cycles utilizing various working pairs, specifically MSC30-R32, MSC30-R245fa, MSC30-CO_2, and Chemviron AC-Ethane. The graphs demonstrate that as the desorption temperature increases, the SCE of the heat pump system improves almost linearly, along with a gradual increase in COP, although the rate of improvement slows down. Comparatively, the adsorption heat pump employing the MSC30-R32 working pair exhibits the highest SCE and COP values among the other four working pairs under equivalent temperature conditions. For adsorption temperature of 30°C and evaporation temperature of 7°C, with the desorption temperature varying from 0°C to 150°C, the maximum COP values obtained for the MSC30-R32, MSC30-R245fa, MSC30-CO2, and Chemviron AC-Ethane working pairs are 0.414, 0.340, 0.113, and 0.057, respectively. Notably, the MSC30-R32 heat pump achieves a COP that is 3.7 times higher than that of the MSC30-CO_2 heat pump. In comparison to other potential working pairs for single-stage ideal adsorption cooling systems, the MSC30/R32 pair exhibited superior performance. Additionally, at a desorption temperature of 90°C, the SCE of the MSC30-R32 heat pump surpasses the SCE of the other three working pairs by 77.08%, 223.48%, and 3908.16%, respectively. It is further noted that the advantages of the adsorption refrigeration system using MSC30-R32 as the working pair in terms of COP and SCE are significant compared to the other activated carbon-refrigerant pairs.

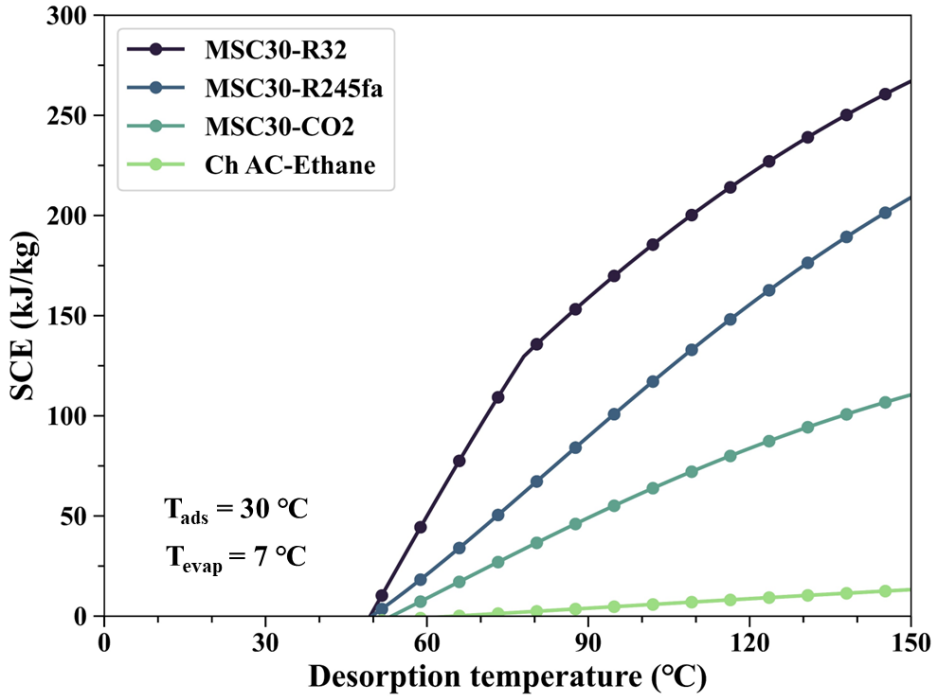

Figure 5.12 The effect of different desorption temperatures on SCE for different working pairs

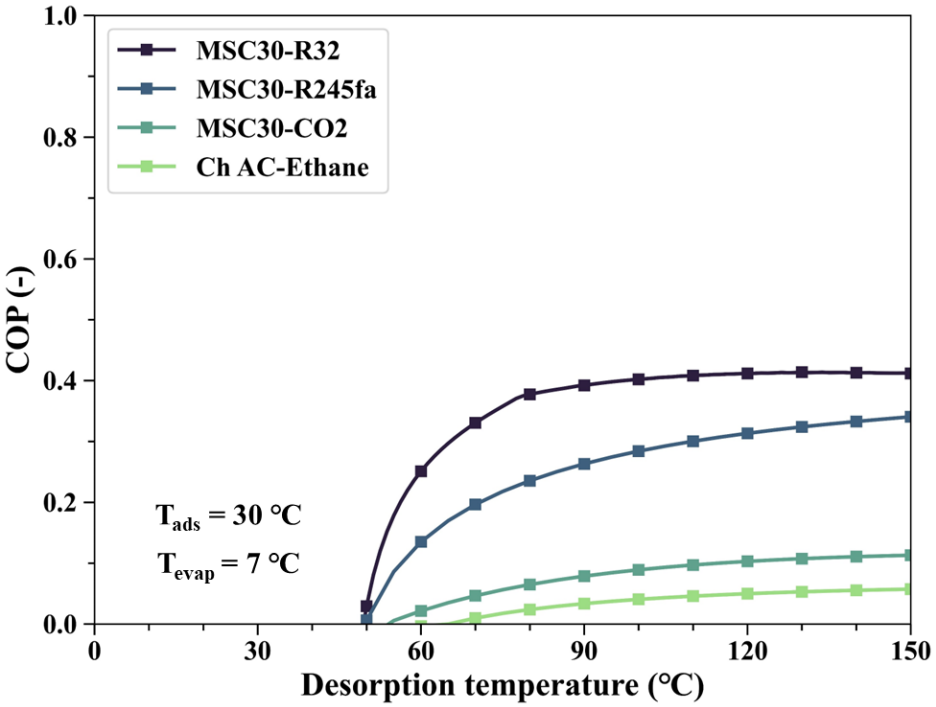

Figure 5.13 The effect of different desorption temperatures on COP for different working pairs

Furthermore, it is worth noting that at adsorption and evaporation temperatures of 30°C and 7°C, respectively, both MSC30-R32 and MSC30-R245fa exhibit comparable lowest desorption temperatures of 49.8°C and 50.3°C, respectively. However, the utilization of Chemviron AC-Ethane as the working pair in the heat pump system necessitates a significantly higher minimum heat source temperature of 65.8°C to yield positive values of SCE and COP. In contrast, employing MSC30-R32 in the heat pump cycle achieves an SCE of 77.56 $kJ \cdot kg^{-1}$ and a COP of 0.31 at this operating condition.

5.4 Conclusions

In this chapter, the thermodynamic model of equilibrium adsorption refrigeration cycles is employed to analyze the thermodynamic performance of low-temperature-driven adsorption refrigeration systems. The equilibrium cycle analysis of the adsorption heat pump utilizing R32 and MSC 30 as the working pair under supercritical conditions was conducted. The impact of varying adsorption temperature (10-40°C), evaporation temperature (2-12°C), desorption temperature (30-150°C), and mass ratio (0-2) on the performance indicators, such as SCE and COP, is investigated for the adsorption heat pump cycle using MSC30-R32 as the working pair. Furthermore, a comparative analysis is conducted to examine the performance characteristics of different activated carbon-refrigerant working pairs, including MSC30-CO2, MSC30-R245fa, MSC30-R134a, and Chemviron AC-Ethane etc., in adsorption heat pump systems.

The simulation results revealed that for the MSC30-R30 adsorption refrigeration

cycle with adsorption and desorption temperatures of 30°C and 90°C, respectively, and evaporation and condensation temperatures of 7°C and 30°C, the maximum relative adsorption capacity was found to be 0.82, while the relative adsorption capacity after desorption was 0.54. The adsorbent bed exhibited maximum and minimum pressures of 1927.51 kPa and 1011.50 kPa, respectively, during the adsorption-desorption cycle.

The COP and SCE of the system exhibited a positive correlation with the desorption temperature but a negative correlation with the evaporation temperature. This can be attributed to the increase in desorption temperature, which leads to an augmented effective adsorption capacity and subsequently enhances the refrigeration capacity of the system. The highest COP and SCE values obtained were 0.48 and 461.09 $kJ \cdot kg^{-1}$, respectively.

Regarding the comparison of different metal mass heat exchangers in the heat pump system, it was observed that as the metal-adsorbent mass ratio increased, more heat was utilized to modify the temperatures of the metal tubing and fins within the adsorbent bed. Consequently, this resulted in a decline in system efficiency. Thus, for practical implementation of heat pump cycles, it is advisable to employ materials with low density, low specific heat capacity, and high thermal conductivity, such as aluminum foam or carbon-based materials, as heat exchanger frameworks.

In comparison to heat pumps utilizing natural refrigerants like MSC30-CO2 or MSC30-Methane, the MSC30-R32 working pair demonstrated lower working pressure and absolute adsorption capacity. Furthermore, in comparison to other activated carbon-refrigerant working pairs, the utilization of MSC-R32 exhibited superior performance under similar operating conditions, leading to higher COP and SCE values. Notably, the MSC30-R32 heat pump exhibited a maximum COP that was 3.7 times higher than that of the MSC30-CO2 heat pump. For instance, at a desorption

temperature of 90°C, the MSC30-R32 heat pump exhibited SCE values that were 77.08%, 223.48%, and 3908.16% higher compared to MSC30-R245fa, MSC30-CO2, and Chemviron AC-Ethane working pairs, respectively. Through this comprehensive investigation, valuable insights into the thermodynamics and performance behavior of adsorption refrigeration cycles under various operating conditions are obtained. The results of this study offer valuable insights for enhancing the performance of adsorption heat pump systems utilizing R32 and MSC30.

5.5 Nomenclature

a_0-a_4	Coefficients for the specific heat capacity (-)
b_0-b_3	Coefficients for the specific heat capacity (-)
c_0	Volume-based maximum uptake ($cm^3 \cdot g^{-1}$)
c_p	Specific heat capacity ($J \cdot kg^{-1} \cdot K^{-1}$)
COP	Coefficient of performance (-)
E	Characteristic energy of adsorption ($J \cdot mol^{-1}$)
h_{fg}	Specific enthalpy of evaporation ($kJ \cdot kg^{-1}$)
k	Index of the pseudo-saturation equation (-)
mm	Molar mass ($g \cdot mol^{-1}$)
n	Heterogeneity factor (-)
p	Pressure (kPa)
q_{st}	Isosteric heat of adsorption ($kJ \cdot kg^{-1}$)
R	Molar gas constant (8.314 $J \cdot mol^{-1} \cdot K^{-1}$)
SCE	Specific cooling energy ($kJ \cdot kg^{-1}$)
T	Temperature (K)
w	Equilibrium uptake in mass ratio ($kg \cdot kg^{-1}$)
Greek symbols	
θ	Surface coverage (-)
κ	parameter of adsorption potential model (-)
φ	parameter of absolute uptake correction (-)
Subscript	

aded	Adsorbed phase
ads	Adsorbent/adsorption
atm	Atmospheric
bed	Adsorption bed
cond	Condenser
crit	Critical
des	Desorption
evap	Evaporator
gas	Gas phase
lat	Latent
max	Maximum
min	Minimum
pc	Pre-cooling
ph	Pre-heating
ref	refrigerant
sat	Saturation
satgas	Saturated liquid phase
satliq	Saturated gas phase
sen	Sensible
tot	Total

5.6 References

[1] S. Jribi, B.B. Saha, S. Koyama, H. Bentaher. Modeling and simulation of an activated carbon–CO2 four bed based adsorption cooling system, J. *Energy Conversion and Management*. 78(2014) 985-991, doi: 10.1016/j.enconman.2013.06.061.

[2] B. Sun, A. Chakraborty. Thermodynamic formalism of water uptakes on solid porous adsorbents for adsorption cooling applications, J. *Applied Physics Letters*. 104(2014), doi: 10.1063/1.4876922.

[3] R.H. Mohammed, O. Mesalhy, M.L. Elsayed, L.C. Chow. Novel compact bed design for adsorption cooling systems: Parametric numerical study, J. *International Journal of Refrigeration-Revue Internationale Du Froid*. 80(2017)

238-251, doi: 10.1016/j.ijrefrig.2017.04.028.

[4] W.S. Loh, I.I. El-Sharkawy, K.C. Ng, B.B. Saha. Adsorption cooling cycles for alternative adsorbent/adsorbate pairs working at partial vacuum and pressurized conditions, J. *Applied Thermal Engineering*. 29(2009) 793-798, doi: 10.1016/j.applthermaleng.2008.04.014.

[5] I. Jahan, T.H. Rupam, M.L. Palash, K.A. Rocky, B.B. Saha. Energy efficient green synthesized MOF-801 for adsorption cooling applications, J. *Journal of Molecular Liquids*. 345(2022), doi: 10.1016/j.molliq.2021.117760.

[6] M. Ghazy, A.A. Askalany, K. Harby, M.S. Ahmed. Adsorption isotherms and kinetics of HFC-404A onto bituminous based granular activated carbon for storage and cooling applications, J. *Applied Thermal Engineering*. 105(2016) 639-645, doi: 10.1016/j.applthermaleng.2016.03.057.

[7] A. Pal, K.A. Rocky, B.B. Saha. Thermodynamic analysis of promising biomass-derived activated carbons/CO2 based adsorption cooling systems, J. *Journal of Co2 Utilization*. 46(2021), doi: ARTN 101457 10.1016/j.jcou.2021.101457.

[8] S. Seo, H. Kawakami, F. Miksik, N. Takata, K. Thu, T. Miyazaki. Thermodynamic analysis and impact of thermal masses on adsorption cycles using MaxsorbIII/R245fa and SAC-2/R245fa pairs, J. *International Journal of Refrigeration*. 123(2021) 52-62, doi: 10.1016/j.ijrefrig.2020.12.005.

[9] F.H.M. Azahar, S. Mitra, A. Yabushita, A. Harata, B.B. Saha, K. Thu. Improved model for the isosteric heat of adsorption and impacts on the performance of heat pump cycles, J. *Applied Thermal Engineering*. 143(2018) 688-700, doi: 10.1016/j.applthermaleng.2018.07.131.

[10] K.A. RAHMAN. Experimental and Theoretical Studies on Adsorbed Natural Gas Storage System Using Activated Carbons, National University of Singapore, 2011.

[11] B.B. Saha, S. Jribi, S. Koyama, I.I. E-Sharkawy. Carbon Dioxide Adsorption Isotherms on Activated Carbons, J. *Journal of Chemical and Engineering Data*. 56(2011) 1974-1981, doi: 10.1021/je100973t.

[12] N. Tzabar, H.J.M. ter Brake. Adsorption isotherms and Sips models of nitrogen, methane, ethane, and propane on commercial activated carbons and

polyvinylidene chloride, J. *Adsorption-Journal of the International Adsorption Society*. 22(2016) 901-914, doi: 10.1007/s10450-016-9794-9.

Chapter 6
Conclusions

6.1 Major Finding of this Research

This research study critically assesses the feasibility and performance of an adsorption heat pump system utilizing the adsorbent-refrigerant pair in the context of low-grade heat sources, including solar energy, geothermal energy, and industrial waste heat. The investigation employs a comprehensive approach encompassing theoretical analysis, experimental testing, thermodynamic analysis, and steady-state simulations to gain in-depth insights into the adsorption characteristics of the activated carbon (Type MSC30)- difluoromethane (R32) pair and its potential application in low-grade heat-driven heat pump systems. The main research tasks and findings encompass the following aspects:

Firstly, experimental investigations were conducted using a thermal gravimetric approach to investigate the fundamental adsorption equilibrium characteristics of the refrigerant R32 on MSC30 activated carbon surfaces. The study encompassed a comprehensive range of operating conditions, including temperatures spanning from 25 °C to 150 °C and pressures ranging from 0 to 3000 kPa. This investigation represents a significant advancement as it is the first to examine the adsorption equilibrium characteristics of the R32-MSC30 pair under such extensive supercritical conditions. Furthermore, a comparative analysis of different methods for absolute

adsorption correction was performed to determine the most accurate approach in estimating the true adsorption uptake for this adsorbent-refrigerant system. Moreover, a novel and improved thermodynamic model for adsorption potential was developed specifically for adsorption processes operating under supercritical conditions. To assess the model's performance and reliability, isotherm data from diverse working pairs were employed for validation purposes. The results showcased exceptional fitting capabilities of the proposed model when applied to experimental adsorption isotherm data, with an average absolute deviation (AAD) error of merely 2.42 for the MSC30-R32 working pair. Importantly, the fitting errors observed for the proposed model were notably smaller compared to those of the conventional Tóth adsorption isotherm model and the traditional empirical equation relying on pseudo saturation pressure.

Secondly, based upon the experimental data obtained for the MSC30-R32 working pair, the adsorption thermodynamic properties, including adsorption enthalpy, specific heat capacity, entropy, and enthalpy, were calculated and analyzed within the temperature range of 0-160 °C. A novel adsorption isosteric heat model was proposed and validated using experimental data from four different working pairs: MSC30-R32, MSC30-Methane, MSC30-CO_2, and Chemviron AC-Ethane. The proposed model exhibited excellent consistency with classical models. Furthermore, a thorough investigation was conducted to assess the influence of temperature, pressure, and adsorption uptake on the thermophysical properties of the MSC30-R32 working pair under both subcritical and supercritical conditions. The results revealed that at temperatures below the critical temperature, substituting the specific heat capacity of the adsorbed liquid for the adsorbed phase was deemed acceptable when the relative adsorption quantity was below 0.6. However, at higher adsorption quantities, using the specific heat capacity of the saturated liquid as a substitute would lead to an

overestimation. Under supercritical conditions, the difference between the specific heat capacity of the gaseous refrigerant and the adsorbed phase should not be overlooked. Moreover, a comparative analysis was performed between the specific heat capacity of the MSC30-R32 working pair and other commonly used working pairs, including methane, ethane, and CO_2. The results demonstrated that the adsorbed specific heat capacity of the MSC30-R32 system was significantly lower than that of the other working pairs. This indicates that the MSC30-R32 system exhibits reduced energy wastage during heating or cooling processes, thus presenting potential advantages in terms of energy efficiency. Additionally, the impact of temperature and adsorption uptake on the entropy and enthalpy of the adsorbed phase was thoroughly evaluated. Regardless of whether the system operated under supercritical or subcritical conditions, an increasing trend in both entropy and enthalpy was observed with the growth of surface coverage. However, the influence of temperature on entropy and enthalpy was less pronounced under supercritical conditions compared to subcritical conditions. The entropy and enthalpy values varied between 1.88-5.28 $kJ \cdot kg^{-1} \cdot K^{-1}$ and 126.40-550.08 $kJ \cdot kg^{-1}$, respectively, when the temperature ranged from 10-70 °C and the surface coverage varied between 0.1 and 0.9. Similarly, when the temperature varied from 80-130 °C and the surface coverage ranged from 0.1 to 0.9, the entropy and enthalpy values ranged between 1.95-4.45 $kJ \cdot kg^{-1} \cdot K^{-1}$ and 328.47-538.99 $kJ \cdot kg^{-1}$, respectively.

Thirdly, the present study focused on investigating the adsorption kinetics of R32 vapor on MSC30 activated carbon powder adsorbent using a gravimetric approach facilitated by a MSB unit. A thorough assessment was conducted to evaluate the accuracy and suitability of various adsorption kinetics models, namely the FD model, LDF model, semi-infinite model, Sultan's modified LDF model, and Jribi's modified

LDF model, for predicting the kinetics uptake of the MSC30-R32 working pair. Notably, the fitting of the Arrhenius equation enabled the estimation of the activation energy E_a and pre-exponential coefficient $\frac{D_s}{R_p^2}$ for the MSC30-R32 pair, yielding values of 6262.37 kJ·kg^{-1}. and 0.00853 s^{-1}, respectively. In comparison to other common MSC30-refrigerant working pairs, the MSC30-R32 pair exhibited the highest diffusion time constant and adsorption rate, indicating its favorable kinetic performance. Furthermore, to enhance the accuracy and expand the applicability range of the Jribi model, a novel mass transfer coefficient model was proposed in this study. The proposed model was comprehensively validated using various adsorbent-adsorbate pairs across a wide temperature range. The combination of the Jribi modified LDF model and the proposed mass transfer coefficient model demonstrated remarkable precision and accuracy in predicting the adsorption kinetics of diverse working pairs.

Ultimately, this study examines the thermodynamic performance of an equilibrium adsorption refrigeration cycle, focusing on the utilization of low-temperature driving heat source. The investigation explores the impact of varying adsorption temperatures (10-40°C), evaporation temperatures (2-12°C), desorption temperatures (30-150°C), and mass ratios (0-2) on the performance indicators of the MSC30-R32 working pair adsorption heat pump cycle, such as specific cooling energy (SCE) and coefficient of performance (COP). A comparative analysis is conducted using different activated carbon-refrigerant working pairs, including MSC30-CO_2, MSC30-R245fa, MSC30-R134a, and Chemviron AC-Ethane, thereby assessing their respective performance within adsorption heat pump systems. The outcomes obtained from simulations indicate that for the MSC30-R32 adsorption refrigeration cycle,

wherein adsorption occurs at 30°C and desorption at 90°C, while evaporation and condensation take place at 7°C and 30°C respectively, the maximum relative adsorption capacity reaches 0.82, followed by a relative adsorption capacity of 0.54 after desorption process. Within the adsorption-desorption cycle, the highest and lowest pressures experienced by the adsorption bed are recorded at 1927.51 kPa and 1011.50 kPa respectively. A positive correlation between COP, SCE, and desorption temperature is observed, while a negative correlation is noted with respect to the evaporation temperature. This phenomenon can be attributed to the increase in effective adsorption capacity resulting from higher desorption temperatures, leading to enhanced refrigeration capability. The MSC30-R32 heat pump cycle achieves the highest COP of 0.48 and SCE of 461.09 $kJ \cdot kg^{-1}$. Moreover, a comparative analysis of different heat exchanger designs is conducted, revealing that with increasing metal-adsorbent mass ratio, a greater amount of heat is utilized to regulate the temperature of the metal pipes and fins within the adsorption bed. As a result, system efficiency is diminished. Consequently, it is recommended that heat exchanger frameworks with low-density, low specific heat capacity, and high thermal conductivity materials, such as aluminum foam or carbon-based materials, be utilized in practical heat pump cycles. In comparison to heat pumps employing MSC30-CO2 or MSC30-Methane as natural refrigerants, the MSC30-R32 working pair demonstrates lower operating pressures and absolute adsorption capacity. When compared to other activated carbon-refrigerant working pairs, the utilization of MSC-R32 shows superior performance under identical operating conditions, yielding higher COP and SCE values. Notably, the highest COP achieved by the MSC30-R32 heat pump is 3.7 times greater than that of the MSC30-CO_2 heat pump. For instance, at a desorption temperature of 90°C, the SCE of the MSC30-R32 adsorption heat pump surpasses that of the MSC30-R245fa, MSC30-CO_2,

and Chemviron AC-Ethane working pairs by 77.08%, 223.48%, and 3908.16% respectively.

In summary, the research outcomes presented in this study offer significant contributions to the understanding of the adsorption characteristics and thermodynamic performance of the MSC30-R32 working pair. The investigations shed light on the thermodynamic properties of this working pair across a wide range of operating conditions, with a particular focus on supercritical conditions. These insights provide a foundation for more accurate design and optimization of adsorption-based refrigeration and heat pump systems. Additionally, the findings have practical implications for the development and optimization of adsorption-based cooling and heating systems, promoting energy efficiency improvements and environmental sustainability.

6.2 Recommendations for future work

Based on the present study, a summary of further research directions in the domain of adsorption heat pumps covered in this thesis, is presented below.

1. The performance and cost of adsorption working pairs are critical considerations that impede the widespread adoption of adsorption systems on a large scale. Consequently, it is pertinent to explore meaningful avenues aimed at enhancing adsorption capacity and thermal conductivity. One promising approach involves surface modification of adsorbents through the addition of additives, such as functional groups and composite materials.
2. In the realm of steady-state adsorption heat pump cycles, the adoption of

idealized assumptions introduces certain discrepancies when comparing the actual performance of heat pump cycles. Therefore, it becomes imperative to explore the dynamic adsorption heat pump cycle, considering factors such as cycle time and heat transfer efficiency. Both simulation and experimental endeavors should be pursued in order to comprehensively investigate and validate the dynamic behavior of adsorption heat pump cycles.

3. In comparison to conventional HFC refrigerants, R32 exhibits a lower environmental impact; however, its GWP value remains higher when compared to natural refrigerants like water, ammonia, and methanol. Consequently, it becomes imperative to conduct thorough testing and analysis of the performance of adsorption heat pumps utilizing refrigerants that are more environmentally friendly.

Appendix A
Experimental uptake of MSC30-R32 pair

The equilibrium adsorption uptake for the MSC30-R32 working pair, as measured in the experimental study, are displayed in Table A.1.

Table A.1 Equilibrium adsorption uptake for the MSC30-R32 pair

T(°C)	P(kPa)	Uptake (g/g)	T(°C)	P(kPa)	Uptake (g/g)	T(°C)	P(kPa)	Uptake (g/g)
25	47.1	0.14	30	47.5	0.11	50	52.2	0.08
25	90.5	0.27	30	92.4	0.22	50	99.9	0.14
25	134.1	0.38	30	137.3	0.32	50	274.7	0.37
25	224.4	0.59	30	230.1	0.50	50	459.2	0.56
25	314.9	0.75	30	322.8	0.65	50	632.2	0.71
25	405.0	0.89	30	415.5	0.78	50	790.4	0.82
25	489.8	1.00	30	507.9	0.89	50	939.3	0.91
25	565.7	1.09	30	599.9	0.99	50	1076.0	0.99
25	634.1	1.17	30	691.5	1.08	50	1198.8	1.05
25	696.1	1.24	30	781.7	1.16	50	1315.7	1.11
25	752.0	1.29	30	862.5	1.23	50	1416.8	1.16
25	802.3	1.34	30	934.9	1.29	50	1517.8	1.20
25	848.2	1.38	30	1000.2	1.34	50	1633.5	1.25
25	890.0	1.42	30	1059.1	1.37	50	1733.4	1.28

25	928.1	1.45	30	1112.3	1.40	50	1831.2	1.31
25	962.7	1.47	30	1160.3	1.43	50	1925.2	1.33
25	994.2	1.49	30	1204.0	1.44	50	2009.3	1.35
25	1023.0	1.50	30	1243.5	1.46	50	2088.6	1.37
25	1049.3	1.51	30	1279.8	1.47	50	2153.5	1.38
25	1073.4	1.52	30	1312.3	1.48	50	2228.9	1.39
25	1095.3	1.53	30	1342.1	1.48	50	2305.3	1.39
25	1115.6	1.54	30	1369.3	1.49	50	2375.3	1.40
25	1134.0	1.54	30	1394.0	1.49	50	2441.9	1.40
25	1151.0	1.55	30	1416.9	1.50	50	2500.3	1.41
25	1166.5	1.55	30	1437.9	1.50	50	2546.3	1.41
25	1180.9	1.55	30	1456.7	1.50	50	2561.7	1.41
25	1194.4	1.56	30	1474.2	1.50	50	2582.8	1.41
25	1206.6	1.56	30	1490.3	1.51	50	2596.1	1.41
25	1217.6	1.56	30	1505.0	1.51	50	2609.3	1.41
25	1227.8	1.56	30	1518.7	1.51	50	2622.6	1.41
25	1237.2	1.57	30	1530.9	1.51	50	2636.2	1.41
25	1245.7	1.57	30	1542.5	1.51	50	2648.7	1.41
25	1253.9	1.57	30	1553.2	1.51	50	2659.6	1.41
25	1261.3	1.57	30	1562.8	1.52	50	2671.7	1.41
…	…	…	…	…	…	…	…	…
25	1324.1	1.58	30	1666.6	1.53	50	2780.3	1.42

T(°C)	P(kPa)	Uptake (g/g)	T(°C)	P(kPa)	Uptake (g/g)	T(°C)	P(kPa)	Uptake (g/g)
70	52.0	0.05	90	52.9	0.03	110	55.4	0.02
70	104.4	0.09	90	106.6	0.06	110	110.8	0.04
70	211.6	0.18	90	217.1	0.12	110	226.0	0.09
70	318.5	0.26	90	327.4	0.18	110	341.7	0.13
70	423.9	0.34	90	438.6	0.24	110	459.0	0.17
70	531.2	0.41	90	551.1	0.29	110	576.2	0.21
70	637.5	0.48	90	664.4	0.34	110	694.3	0.25
70	743.4	0.54	90	777.6	0.39	110	813.7	0.29
70	852.0	0.60	90	891.5	0.43	110	934.1	0.33
70	959.1	0.65	90	1006.8	0.48	110	1056.7	0.36
70	1066.4	0.70	90	1121.9	0.52	110	1180.3	0.40
70	1174.7	0.74	90	1238.9	0.56	110	1304.3	0.43
70	1282.7	0.78	90	1356.5	0.59	110	1430.5	0.46
70	1391.9	0.83	90	1474.8	0.63	110	1558.3	0.49
70	1501.0	0.86	90	1594.7	0.66	110	1687.4	0.52
70	1610.9	0.90	90	1715.8	0.69	110	1818.0	0.54
70	1721.3	0.93	90	1837.9	0.72	110	1951.0	0.57
70	1831.8	0.97	90	1962.6	0.75	110	2087.0	0.60
70	1943.5	1.00	90	2088.2	0.78	110	2226.6	0.62
…	…	…	…	…	…	…	…	…
70	2972.2	1.20	90	2990.8	0.93	110	2977.2	0.74

T(°C)	P(kPa)	Uptake (g/g)	T(°C)	P(kPa)	Uptake (g/g)
130	59.0	0.02	150	60.4	0.01
130	117.5	0.03	150	120.5	0.02
130	237.8	0.07	150	244.9	0.05
130	359.6	0.10	150	371.2	0.08
130	481.8	0.13	150	499.1	0.10
130	605.5	0.16	150	627.7	0.12
130	729.9	0.19	150	757.7	0.15
130	856.4	0.22	150	889.8	0.17
130	983.7	0.25	150	1022.9	0.19
130	1112.5	0.28	150	1157.7	0.22
130	1242.5	0.30	150	1294.5	0.24
130	1374.8	0.33	150	1433.3	0.26
130	1509.0	0.36	150	1574.6	0.28
130	1645.1	0.38	150	1718.4	0.30
130	1783.4	0.40	150	1865.6	0.33
130	1924.1	0.43	150	2015.9	0.35
130	2068.3	0.45	150	2170.5	0.37
130	2215.7	0.47	150	2327.9	0.39
130	2358.9	0.49	150	2461.5	0.40
…	…	…	…	…	…
130	2995.5	0.58	150	2975.6	0.46

Appendix B
Effect of operating conditions on the performance of adsorption cycle

The operational parameters, including the desorption temperature T_{des}, adsorption temperature T_{ads}, and evaporation temperature T_{evap}, play a crucial role in influencing the performance of adsorption heat pumps. The desorption temperature, commonly referred to as the regeneration temperature, primarily relies on the available heat source temperature within the system. Conversely, the adsorption temperature aligns closely with the condensation temperature T_{cond} and is contingent upon the cooling water temperature or ambient temperature. The evaporation temperature, on the other hand, is predominantly affected by the properties of refrigerant and the desired temperature of the chilled water. A detailed analysis of the impact of these operational parameters on the performance of adsorption heat pumps has been thoroughly discussed in Section 5.3 of this study. Additionally, this appendix presents a comprehensive examination of the variations observed in the adsorption heat pump cycle utilizing the MSC30-R32 working pair as these operational parameters are modified, thus providing supplementary insights into the subject matter.

Figure B.1 and Figure B.2 present the variations of the adsorption heat pump cycle on the Pressure-Temperature-uptake (p-T-w) diagram with an evaporation temperature of 7°C and an adsorption temperature of 30°C, while altering the desorption temperature. Notably, the adsorption bed pressure remains unaffected by changes in the desorption temperature, maintaining the evaporator and condenser pressures at constant values of

1101.50 kPa and 1927.51 kPa, respectively. However, as the desorption temperature increases, a gradual reduction in the minimum adsorption capacity of the bed is observed, while the maximum adsorption capacity remains unchanged. Consequently, the effective adsorption capacity progressively increases. For example, when the desorption temperature rises from 60°C to 150°C, the minimum adsorption capacity decreases from 1.17 $kg \cdot kg^{-1}$ to 0.34 $kg \cdot kg^{-1}$, whereas the effective adsorption uptake elevates from 0.19 $kg \cdot kg^{-1}$ to 1.02 $kg \cdot kg^{-1}$, indicating a substantial 4.3-fold enhancement. Additionally, Figure B.1 (a) demonstrates that when the desorption temperature approaches 50°C, the minimum adsorption capacity of the bed becomes nearly equal to the maximum adsorption capacity, resulting in an effective adsorption capacity of 0. Consequently, the adsorption bed fails to provide effective cooling capability in such instances.

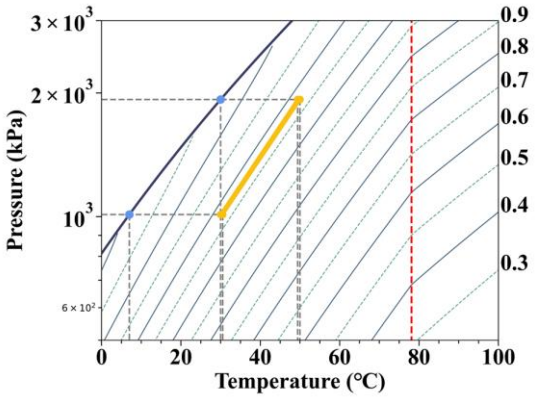

(a) Desorption temperature of 50 °C

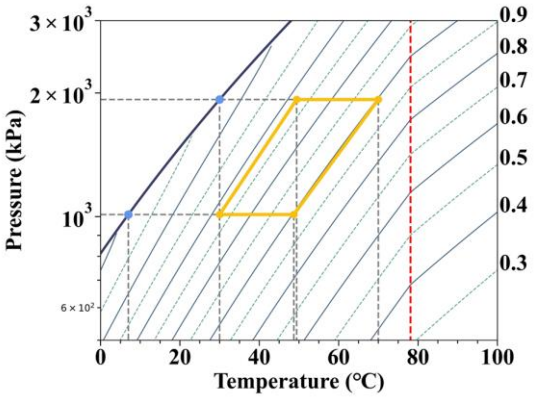

(b) Desorption temperature of 70 °C

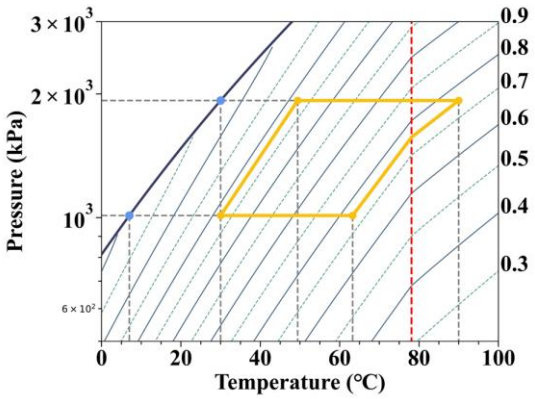

(c) Desorption temperature of 90 °C

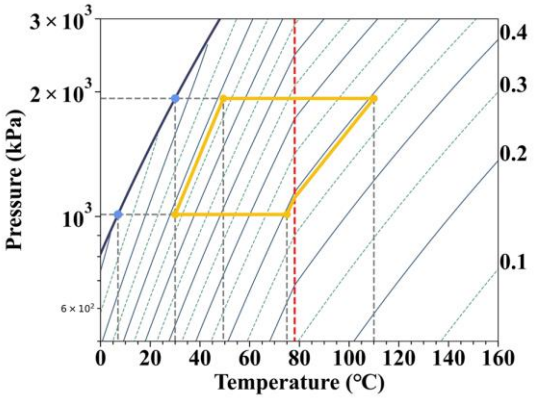

(d) Desorption temperature of 110 °C

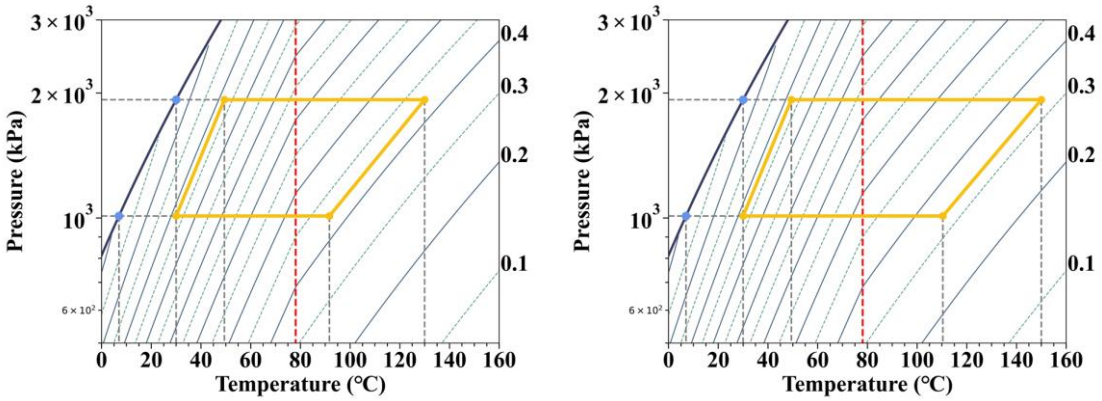

(e) Desorption temperature of 130 °C (f) Desorption temperature of 150 °C

Figure B.1 Representation of cooling cycle on p-T-w diagram of MSC30-R32 pair with different desorption temperatures at T_{ads} of 30 °C and T_{evap} of 7 °C

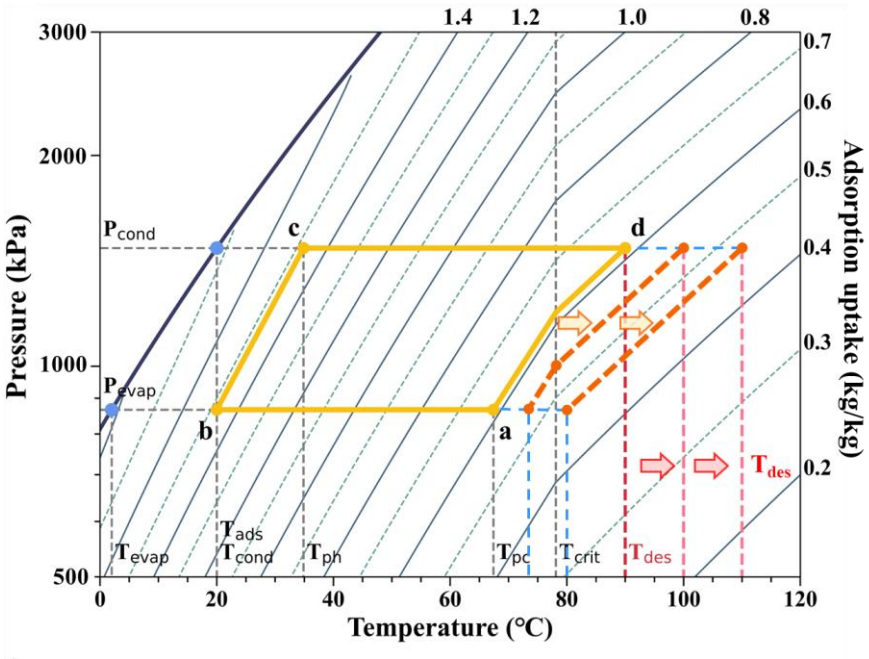

Figure B.2 Effect of the increasing desorption temperature on cooling cycle on p-T-w diagram with T_{ads} of 30 °C and T_{evap} of 7 °C

Figure B.3 and Figure B.4 depict the variations in the adsorption heat pump cycle under different adsorption temperatures, while maintaining an evaporation temperature of 7°C and a desorption temperature of 90°C. Notably, the condensation temperature

closely aligns with the adsorption temperature. As the adsorption and condensation temperatures increase, it is observed that the condenser pressure progressively rises. Consequently, this leads to a reduction in the maximum adsorption capacity of the bed while the minimum adsorption capacity increases, resulting in a decrease in the effective adsorption capacity. This dynamic is evident in Figure B.4, where point **c** gradually shifts towards the upper right quadrant, while point D moves upwards. Specifically, with an increase in the adsorption temperature from 20°C to 40°C, the effective adsorption capacity declines from 0.95 $kg \cdot kg^{-1}$ to 0.27 $kg \cdot kg^{-1}$ Therefore, optimizing the cooling water temperature to minimize its value holds significant potential for enhancing the overall performance of the adsorption heat pump system.

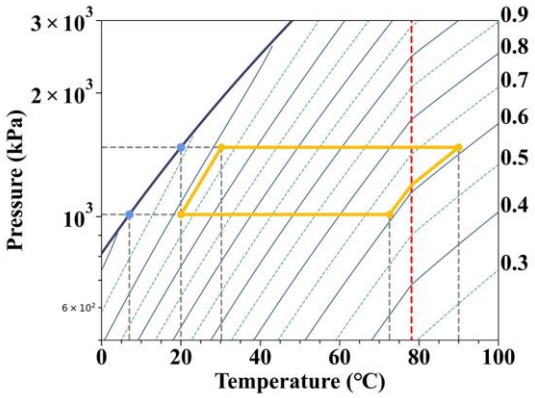

(a) Adsorption temperature of 20 °C

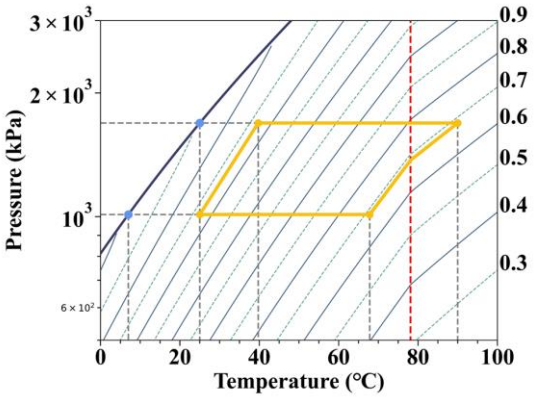

(b) Adsorption temperature of 25 °C

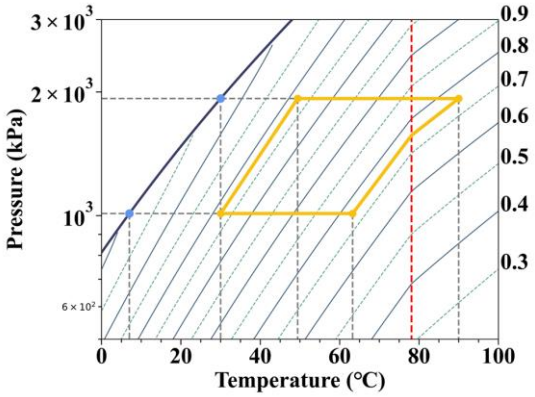

(c) Adsorption temperature of 30 °C

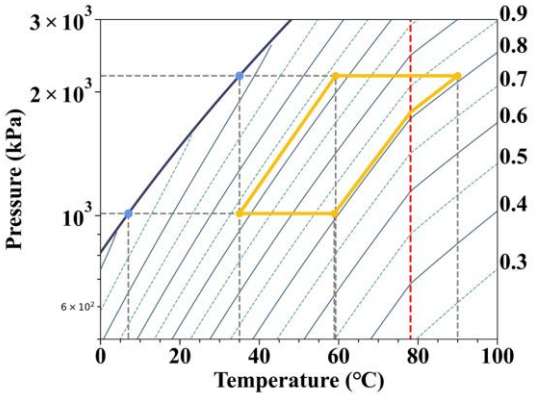

(d) Adsorption temperature of 35 °C

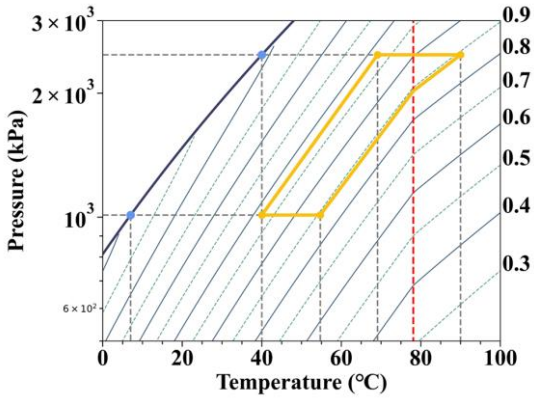

(e) Adsorption temperature of 40 °C

Figure B.3 Representation of cooling cycle on p-T-w diagram of MSC30-R32 pair with different adsorption temperatures at T_{ads} of 90 °C and T_{evap} of 7 °C

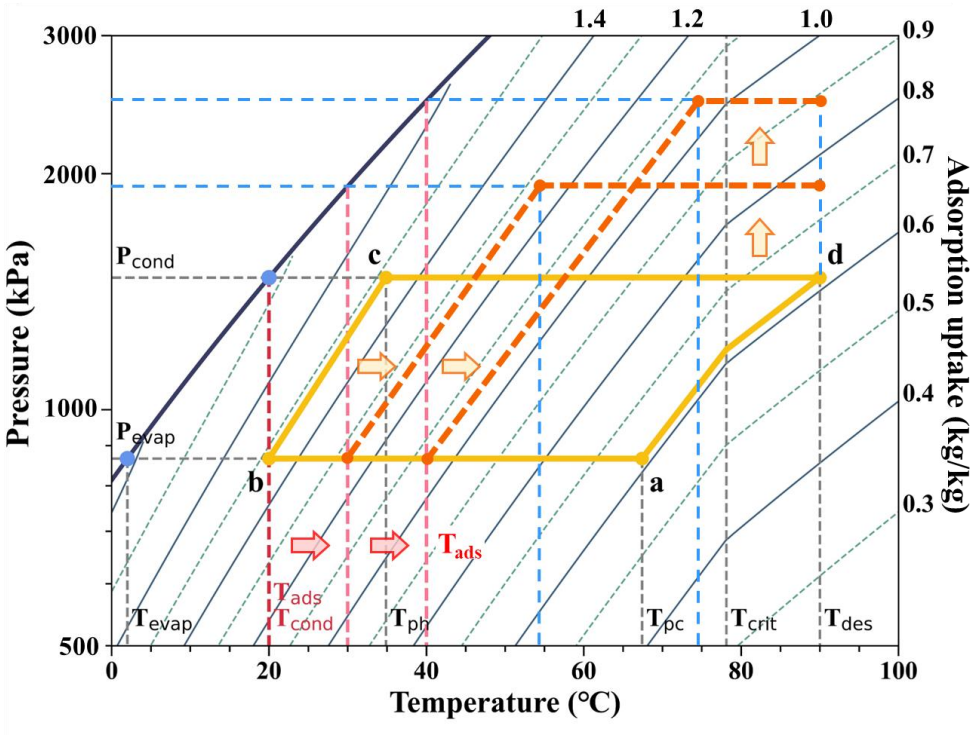

Figure B.4 Effect of the increasing adsorption temperature on cooling cycle on p-T-w diagram with T_{ads} of 90 °C and T_{evap} of 7 °C

Figure B.5 and Figure B.6 present the variations in the adsorption heat pump cycle

as the evaporator temperature (ranging from 2 to 12°C) is investigated, while maintaining a fixed desorption temperature of 90°C and an adsorption temperature of 30°C. It is observed that the condensation pressure and the minimum adsorption capacity of the bed remain unaffected by the changes in the evaporation temperature. However, an increase in the evaporation temperature leads to a gradual rise in the evaporation pressure, resulting in an augmentation of the maximum adsorption capacity and consequently, an elevation in the effective adsorption capacity. This augmentation in the adsorption capacity directly correlates with an enhancement in the system's cooling performance. Specifically, as the evaporation temperature rises from 2 to 12°C, the effective adsorption capacity increases from 0.52 $kg \cdot kg^{-1}$ to 0.70$kg \cdot kg^{-1}$, representing a noteworthy improvement of 34%.

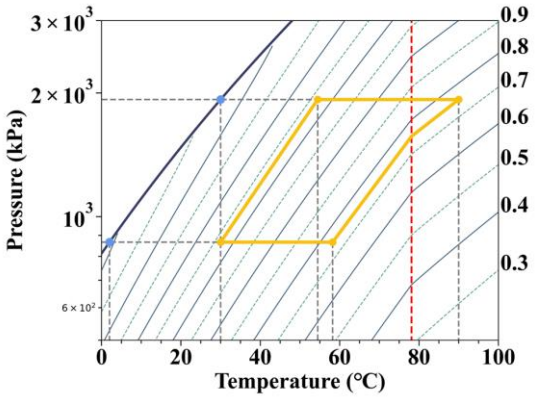

(a) Evaporator temperature of 2 °C

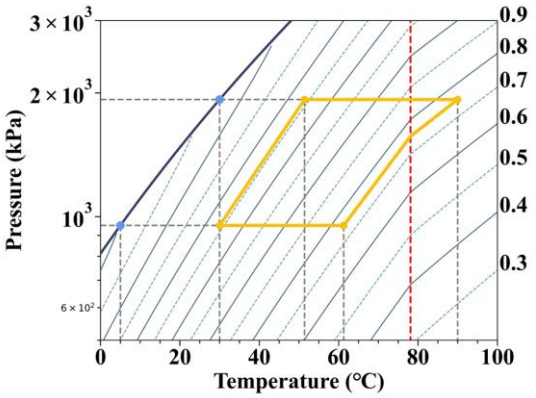

(b) Evaporator temperature of 5 °C

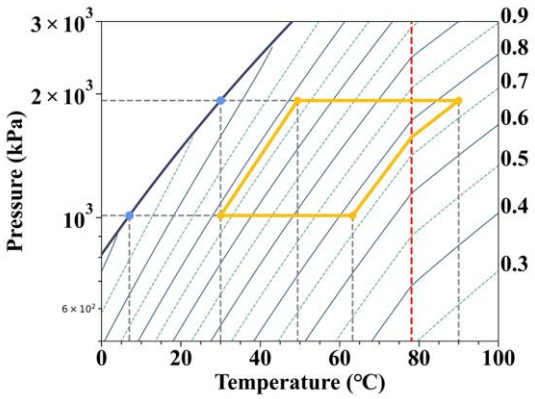

(c) Evaporator temperature of 7 °C

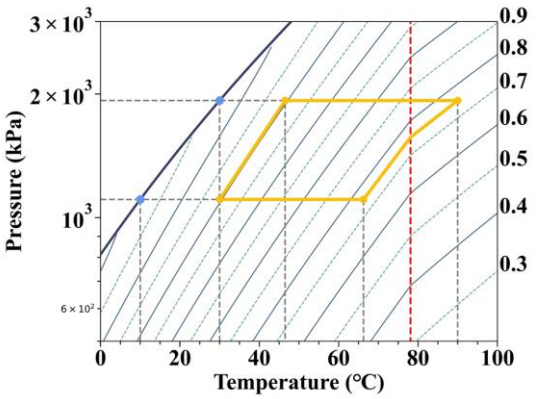

(d) Evaporator temperature of 10 °C

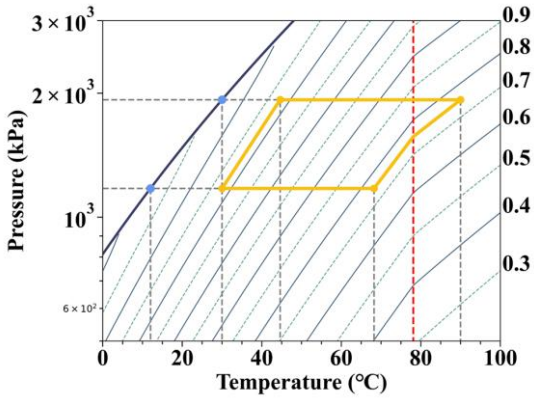

(e) Evaporator temperature of 12 °C

Figure B.5 Representation of cooling cycle on p-T-w diagram of MSC30-R32 pair with different evaporator temperatures at T_{des} of 90 °C and T_{ads} of 30 °C

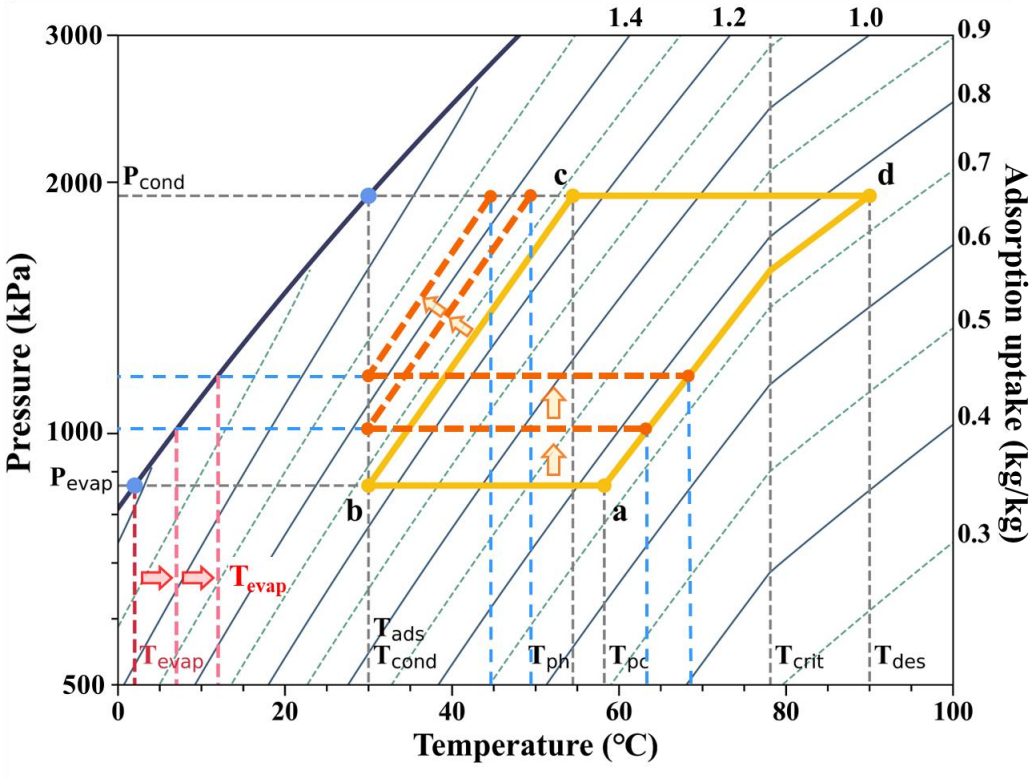

Figure B.6 Effect of the increasing evaporation temperature on cooling cycle on p-T-w diagram with T_{des} of 90 °C and T_{ads} of 30 °C